sciendo **Slovak Journal of Civil Engineering**

Vol. 30, 2022, No. 3, 1 – 8
DOI: 10.2478/sjce-2022-0015

ANALYSIS OF STATIC AND CYCLIC TRAFFIC LOADING OF AN EMBANKMENT SUPPORTED BY A GEOGRID RETAINING STRUCTURE

Jakub, STACHO[1*], Monika, SULOVSKA[1]

Abstract

The article deals with a deformation analysis of a road embankment under different types of static and cyclic loading. A typical cross-section of a road embankment supported by geogrid retaining structures is considered. In the case of a design, the load is usually applied as a distributed static load. The analysis presented in the paper includes all the most loading methods used. Because there are only a few measurements for these types of construction in a given region, the analysis also includes a cyclic loading that aims to simulate real traffic loading. The cyclic loading considered the weights of cars and trucks and the distances between them, based on traffic intensity measurements. The study results showed how significant the differences in vertical and horizontal deformations of an embankment are when the different types and methods of static loading are used in a design. The results of the cyclic loading showed the deformations that can be expected from current real traffic.

Address

[1] Dept. of Geotechnics, Faculty of Civil Engineering, Slovak University of Technology in Bratislava, Bratislava, Slovakia

* ***Corresponding author:*** jakub.stacho@stuba.sk

Key words

- Traffic loading,
- Static loading,
- Cyclic loading,
- Road embankment,
- Geogrid retaining structure.

1 INTRODUCTION

The design of a road embankment supported by a geogrid retaining structure (GRS) is a type of construction increasingly used for expanding road infrastructures in Slovakia. In suitable conditions, the design of a road embankment supported by a GRS can lead to more effective, economical, and less time-consuming alternative to conventional methods. The typical applications of these types of constructions in Slovakia are discussed in, e.g., Dolinajova and Snahnican (2015); Adamec and Snahnican (2016); Silber-Hasslacher and Snahnican (2019); and Sulovska and Stacho (2019). The study presented in this article focuses on road embankments supported by a wrapped GRS with a passive facing system. In the case of a wrapped GRS, the geogrid is on the side of the face returned back into the soil/embankment, see, e.g., Scotland et al. (2014). In the case of a passive facing system, the wrapped GRS is built to a total height in the first step; then, an independent facing system is constructed and given the final form of the structure, see, e.g., Silber-Hasslacher and Snahnican (2019). The analysis presented is focused on vertical and horizontal deformations of an embankment supported by a GRS. The simple analytical and semi-empirical methods for determining the deformations of these structures have been presented by, e.g., Wu (1994) and Holtz and Lee (2002). The numerical modelling, which is based on the finite element method (FEM) or the distinct element method (DEM), was presented by, e.g., Scotland et al. (2016); Drusa and Vlcek (2016); and Wang et al. (2014). The modeling of any traffic loading on an embankment is a separate problem. A traffic load is mostly applied according to Eurocode 1: Actions on structures, Part 2: Traffic loads on bridges (EN 1991-2). Loading Model 1 (LM1) is used. The LM1 defines the magnitude of the loads for the individual loading lanes in a tandem system (TS) and a uniformly distributed load (UDL). According to this standard, the load from a TS and ULD can be distributed to an equivalent distributed load. This method is usually used in the case of the design of a construction supported by GRS. The load is applied as a design static load and represents the most critical situation during the life of a construction. It is used in different verifications of the ultimate limit state (ULS); however, the traffic load is not applied in verifications of the serviceability limit state (SLS). When the static load according to LM1 is used, the deformation of the embankment seems to be too great. The real traffic loading is variable, acts dynamically, and has a smaller magnitude, which means that real deformations of the embankment are significantly smaller. There is not enough permanent monitoring of the deformations of an embankment supported by GRS in Slovakia. For this reason, cyclic loading, the aim of which is to simulate a typical real traffic loading, was modelled. The magnitude of the loads and loading frequency were determined according to the traffic intensity measurements in the given road section.

2 CREATING THE NUMERICAL MODEL FOR THE CASE STUDY

The numerical model of the embankment supported by GRS was done using the Plaxis geotechnical software. The calculations are based on FEM. This software permits modeling a construction process and executes a detailed deformation analysis of an embankment and subsoil under different types of loads. The scheme of the model focused on an embankment supported by GRS is shown in Fig. 1. The embankment has a height of 5.2 to 5.96 m above the terrain level. The width of the embankment at the top was 13.5 m. The whole dimensions of the model were 70 x 30 m, which was appropriate for the type of task. The model was created as a plane strain model using triangular 6-node elements, which were required to reduce the calculation time for the analysis of the cyclic loading. The mesh of the finite elements was refined especially close to the facing of the wrapped GRS to obtain its adequate horizontal deformation of the embankment. A view of the connectivity plot, the finite element mesh, is shown in Fig. 2. The soils were modelled using the Hardening small-strain (HSs) model, see Benz (2007). This constitutive model extends the "classic" Hardening soil (HS) model and permitts taking into account the very small-strain soil stiffness and its non-linear dependency on the strain amplitude. The parameters describing the deformation behavior of the soil are as follows: E_{50}^{ref} - secant stiffness in a standard drained triaxial test; E_{oed}^{ref} - tangent stiffness for the primary oedometer loading; E_{ur}^{ref} - unloading/reloading stiffness; m - power for the stress-level dependency of the stiffness; G_0^{ref} - the initial small-strain shear modulus; and $g_{0.7}$ - the shear strain level of the secant shear modulus. G_s is reduced to about 70% of G_0. The subsoil was modelled as A-type undrained, and the material of the embankment was modelled as drained, see, e.g., the Plaxis manual (2021). The basic properties used in the model are stated in Tab. 1, where γ is the unit weight, g_{sat} is the saturated unit weight; j' is the drained angle of the shear strength; y' is the angle of the dilation, and c' is the drained cohesion. Based on the engineering-geological survey, the subsoil consists of clayey sand. The body of the embankment was designed from silty gravel. The properties, such as γ, g_{sat}, j', c', and E_{oed} were determined according to, e.g., Sulovska and Stacho (2019). In this study, it was assumed that $E_{50}^{ref} = E_{oed}^{ref}$, and $E_{ur}^{ref} = 4 \cdot E_{oed}^{ref}$ in the case of the clayey sand and $E_{ur}^{ref} = 3 \cdot E_{oed}^{ref}$ in the case of the gravels. The angle of the dilatancy of the gravel was determined as $y' = j' - 30°$, see e.g., PLAXIS 2D CE V21.01:1 (2021). Other parameters required for the HSs material model, such as $g_{0.7}$ and G_0^{ref}, were determined according to recommendations made by Ladicsova (2017).

The compacted gravel between the facing blocks and wrapped main body of the embankment, gravel bed, and base course, are usually created of compacted poorly graded gravel. Although the grain size of the material may vary in the backfill, gravel bed, and base course, the same relatively conservative properties are usually used in a practical design, see, e.g., Sulovska and Stacho (2019). Gravel properties, i.e., silty gravel as well as poorly graded gravel, were determined according to STN 72 1001: Classification of soil and rock.

The foundation strips, facing blocks, and asphalt pavement were modelled using only the standard Linear elastic (LE) material model, which adequately simulates the behaviour of these elements. The concrete had the following properties: Young's modulus, E = 35 GPa, and Poisson's ratio, v = 0.2. The wearing course of the pavement had the following properties: an axial stiffness $E.A$ = 97.8 MN.m^{-1}; a bending stiffness $E.I$ = 326 MN.m^{-2}.m^{-1}; and v = 0.35. The geogrid was modelled using an elastoplastic, isotropic geogrid type of material. The elastic stiffness $E_{geogrid}.A_{geogrid}$ was defined at a value of 1100 kN.m^{-1}, and the plastic threshold N_p was applied at a value of 80 kN.m^{-1}. The property of the interface between the geogrid and soil is given by the R_{inter} parameter. The R_{inter} was assumed

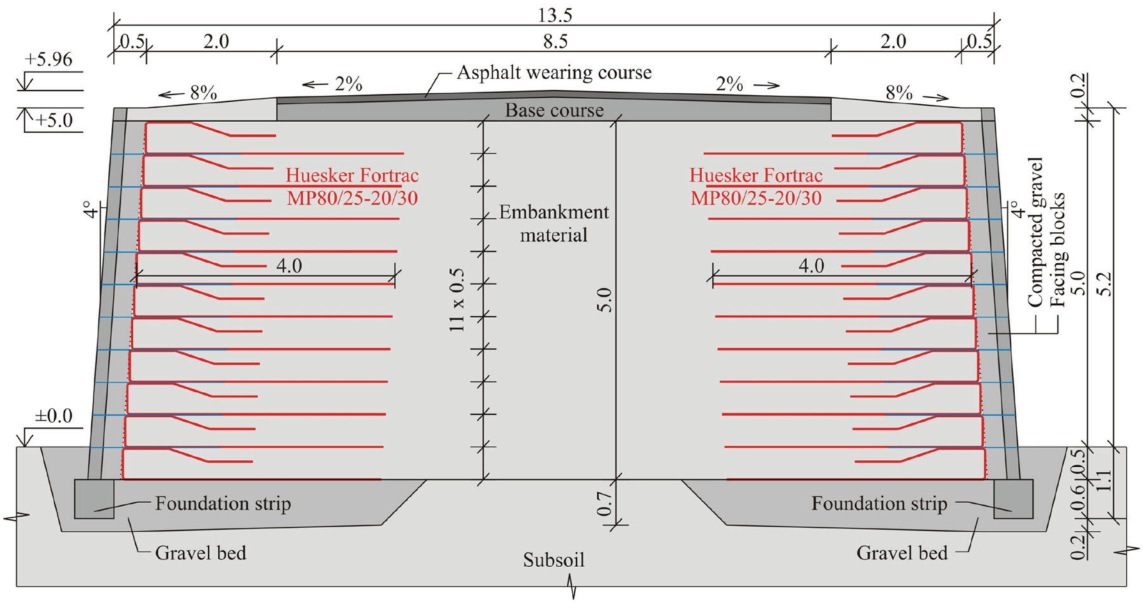

Fig. 1 *Scheme of the road embankment supported by GRS*

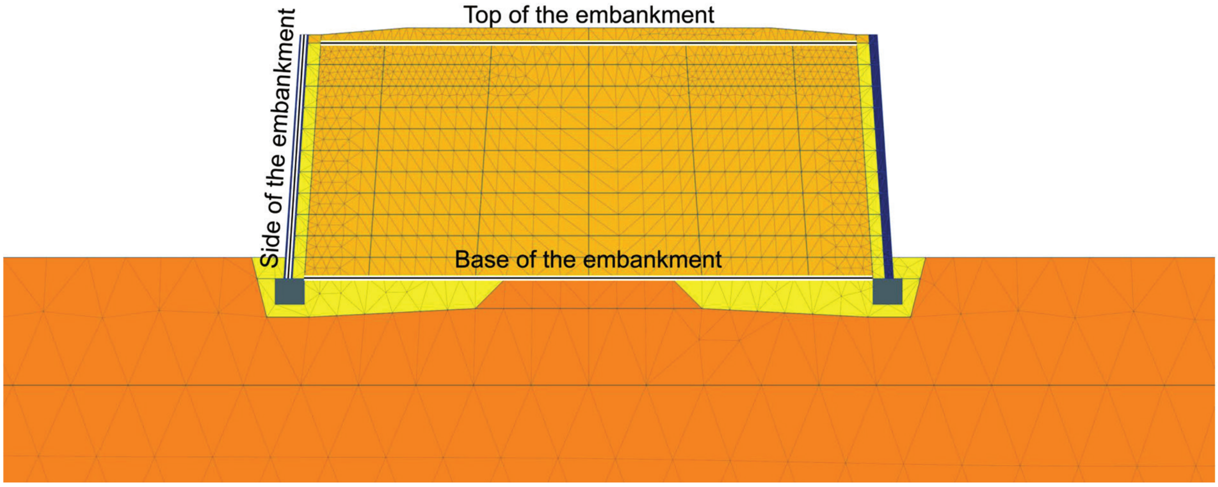

Fig. 2 *Detail of the finite element mesh of the embankment*

at a value of 1.0, which was determined from the study results presented by Stacho et al. (2020). The same consideration was given by Mirmoradi and Ehrlich (2015). The connection between the two geogrids was modeled as rigid. The active length of the geogrid was 4.0 m. The placing of the geogrids is also shown in Fig. 1.

Tab. 1 *Properties of the soils used in the calculations*

Parameter	Unit	Material / Soil		
		Embankment (Silty gravel)	Poorly graded gravel	Subsoil (Clayey sand)
γ	(kN.m^{-3})	19	19	20.3
g_{sat}	(kN.m^{-3})	19	19	20.3
E_{50}	(MN.m^{-2})	84	95	11.7
E_{oed}	(MN.m^{-2})	84	95	11.7
E_{ur}	(MN.m^{-2})	252	285	46.8
m	(-)	0.5	0.5	0.7
G_0	(MN.m^{-2})	157.5	178.0	60.84
$g_{0,7}$	(-)	0.0002	0.0002	0.0003
j'	(°)	28	35	24
y'	(-)	0	5	0
c'	(kN.m^{-2})	5	0	12
Drainage Type	(-)	Drained	Drained	Undrained A

The process of the construction of the embankment supported by GRS was modelled in 19 phases. The phases were modelled as consolidation phases, and the time of each stage was given according to the real construction time of a similar embankment on the same motorway. The initial phases were focused on the landscaping and the construction of the concrete foundation strips. Subsequently, the wrapped body of the embankment was constructed step by step to its full height. The construction of the wrapped GRS was simulated according to a layer-by-layer formwork method. In this part of the calculations, the pure wrapped embankment had relatively significant deformations. After the complete consolidation phase, the deformations were set to zero, and the construction of the facing system and road construction was modelled. The facing blocks were placed 0.3 m from the wrapped GRS body. The space between them was filled by compacted gravel. The facing blocks were connected with the wrapped GRS using the activation of the connecting geogrids. Subsequently, the construction of the road was modelled. The complete consolidation phase ended the modelling of the construction of the embankment. This numerical model was later used in the analysis, where different static and cyclic load types were applied.

2.1 Determining the load from the traffic

In the first part of the analysis, the static load was applied in the numerical modelling. The traffic load was used according to Eurocode 1: Actions on structures, Part 2: Traffic loads on bridges (EN 1991-2). The loads for the individual lanes in the form of TS (acting as the point load) and UDL (acting as the distributed load) were applied according to LM1; see Tab. 2. According to this standard, the load from TS and ULD could be distributed to an equivalent distributed load.

Tab. 2 *Application of the load according to LM1 of the EN 1991-2 standard*

Loading type		Width of the lane	TS	UDL	Coefficients for the road category	
Marking (Unit)		(m)	$Q_{i,k}$ (kN)	$q_{i,k}$ (kN.m^{-2})	$a_{Q,i}$ (-)	$a_{q,i}$ (-)
Location	Lane No.1	3	300	9	0.9	0.9
	Lane No.2	3	200	2.5	0.9	1
	Lane No.3	3	100	2.5	0.9	1
	Remaining area	-	-	2.5	-	1

 Vol. 30, 2022, No. 3, 1 – 8

According to the standard, the loading lanes must be placed to achieve the most critical situation for the design; however, it is not exactly clear how the load must be applied in the given type of construction when the different conditions require placing the load in various positions. For this reason, two options are used in the practical design. The first option considers placing Lane No.1 on both sides of the road and the remaining area between them, see *Loading model A* (Fig. 3). The second option considers the loading on one side, i.e., Lanes Nos. 1 and 2, and the remaining area on the other side of the road, see *Loading model B* (Fig. 3). In the case of *Loading model A* (Fig. 3), two schemes were used, i.e., *Scheme 1*, where all the loads were distributed to a single load f_k, and *Scheme 2*, where the loads in the loading lanes were distributed to load $f_{k,1}$, while the load in the remaining area $q_{2,k}$ corresponds to $f_{2,k}$. In *Loading model B*, the loads in the loading lanes and the remaining lanes are directly distributed to loads $f_{1,k}$; $f_{2,k}$; and $f_{3,k}$ (Fig. 3). The EN 1991-2 standard recommends a load distribution from TS to an area of 6.6 m^2. This option can lead to determining relatively significant deformations, which are often assumed to be unreal. For this reason, the load from TS is distributed to an area of 15 m^2 in the practical design. Both options were used in the study presented in this paper. The characteristic distributed loads for each scheme are summarized in Tab. 3.

In the second part of the analysis, the load was modelled as cyclic and simulated the real traffic load. The numerical modelling of cyclic loading can be done in different ways. An analysis of an embankment or platform under dynamic/cyclic and cyclic loading has been presented by, e.g., Abdelkrim et al. (2003); Zheng et al. (2012); Xuecheng et al. (2010); and Zhuang and Li (2015). In the case of a dynamic analysis, the common problem in numerical modelling is the time required for the calculations and the heavy demands on a computer's hardware. Adam et al. (2000) presented a 3D modelling approach performed with a coupled boundary element-boundary element method and a 2D modelling approach performed by a coupled boundary element-finite element method. They demonstrated effective algorithms for reducing the time and system requirements for the calculations. Another important aspect of the modeling is the way in which the dynamic/cyclic load is defined. In most analyses, the load is specified using a traditional sinusoidal course, see, e.g., Zhuang and Li 2015; Han et al. 2015; Pham and Dias (2019). Other ways of modelling the cyclic load have been presented by, e.g., Zheng et al. (2012), who used a semisine course, or Abdelkrim et al. (2003) and Liu et al. (2017), who demonstrated a simulation of a moving strip or point load, respectively.

Tab. 3 *Loads applied in the numerical modeling in the different models*

Loading type	Loading scheme	Model	Characteristic distributed load		
			$f_{1,k}$	$f_{2,k}$	$f_{3,k}$
Static	Scheme 1	Model S1	31.9	-	-
		Model S2	64.21	-	-
	Scheme 2	Model S1	44.1	2.5	-
		Model S2	89.92	2.5	-
	Scheme 3	Model S1	44.1	26.5	2.5
		Model S2	89.92	57.04	2.5
Cyclic	Scheme 4	Model D1	*changing (Fig. 4)	-	-

In the case of the analyzed embankment supported by GRS, the real traffic intensity was considered. The traffic intensity measurements in the given road section showed that five small passenger cars and one truck passed through the section of the road in one minute. The average weight of the passenger cars at a value of 2.5 t was taken into account. In the case of the truck, the weight of the whole truck of 44.0 t was assumed (Fig. 4). The load was modelled as a distributed load acting as a step (jump) load for loading the road only for the time required to pass a car or truck, respectively, when the nominal speed of 90 km.h^{-1} is taken into account. These times and the times between the cars or between the cars and the truck are stated in Fig. 4. In this way, one loading cycle, which was repeated in numerical simulations, was defined. In this case, the real situation was modelled; as a result, the distributed load of the average width of 2.5 m was modelled in the middle of each lane, see *Loading Model C* and corresponding *Scheme 4* in Fig. 3.

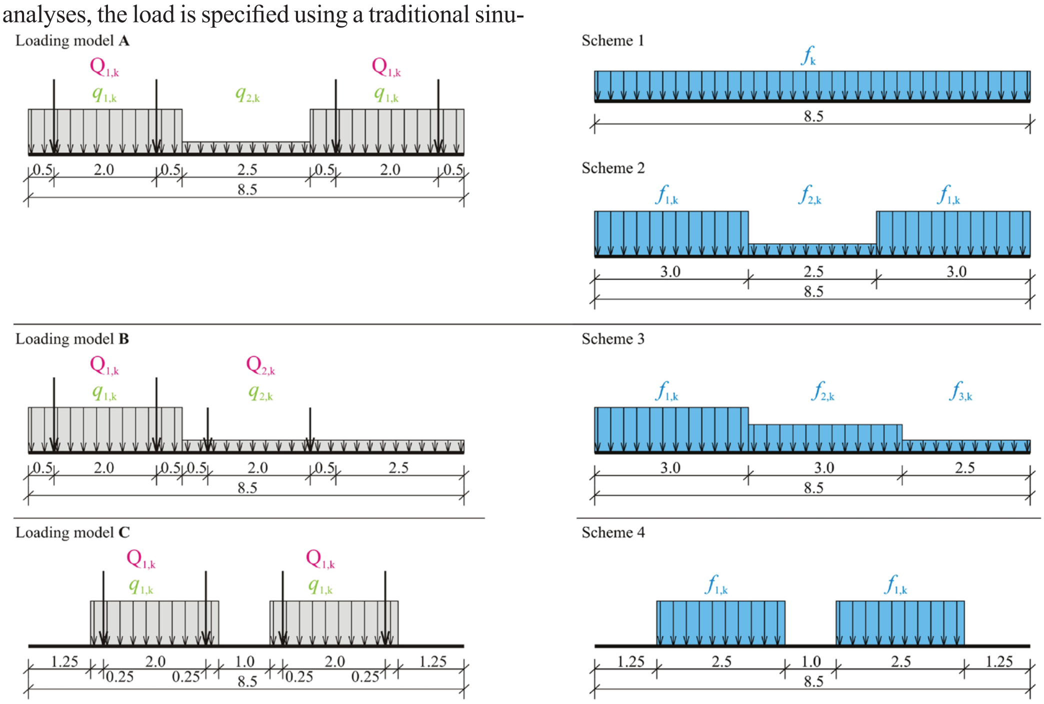

Fig. 3 *Schemes of the loading models and load distributions applied in the numerical modeling*

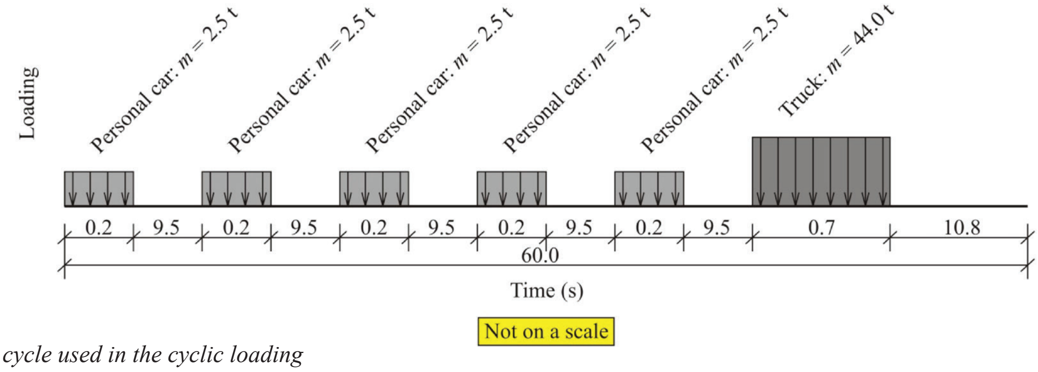

Fig. 4 *One-load cycle used in the cyclic loading*

3 THE RESULTS OBTAINED IN THE STUDY

The results of the study focus on a comparison of the vertical deformations on the top and bottom of the embankment, the horizontal deformations of the side of the embankment, and the passive facing system of the embankment, respectively, see Fig. 2. The total deformations are presented in Fig. 5 for the bottom of the embankment, Fig. 6 for the top of the embankment, and Fig. 7 for the side of the embankment. The first model marked *Initial stage - No traffic load*, represents a situation when no traffic load is applied on the embankment. The deformations are caused only by the construction of the top of the embankment and the construction of the road, respectively, and the construction of the passive facing system. Subsequently, combinations of the different static loads applied were assembled. The application of the loading in *Schemes 1*, *2*, and *3*, is shown in Fig. 3. *Model S1* takes the distribution of the load from TS to an area of 15 m^2 into account, and *Model S2* takes the distribution of the load from TS to an area of 6.6 m^2 into account. The following combinations of models and loading were assembled:

- *Model S1 - Scheme 1*,
- *Model S1 - Scheme 2*,
- *Model S1 - Scheme 3*,
- *Model S2 - Scheme 1*,
- *Model S2 - Scheme 2*,
- *Model S2 - Scheme 3*,

The results are presented for a situation when the static load acted on the embankment for the time required for complete consolidation. This permitted determining the final permanent deformation of the embankment, which was loaded by a different type of static loading. The results obtained for the cyclic loading are marked *Model D1 - Scheme 4*. In this case, the cyclic load was applied according to *Scheme 4* of *Loading model C*. The greatest permanent deformation of the embankment was achieved after 324 loading cycles. The results of the deformation of the embankment under cyclic loading are stated in section 3.1 in more detail.

The results showed that the vertical deformations determined in *Model D1 - Scheme 4* are slightly greater than those reached in the *Initial stage*. The difference is about 3 mm at the bottom of the embankment and about 11.5 mm at the top of the embankment. In *Model D1 - Scheme 4*, the horizontal deformation increased from 6.1 mm (Initial stage) to about 11.0 mm. These results showed that small deformations of the embankment only occur when simulating the actual traffic loading. Applying the static loading typically used in the design led to determining significantly greater embankment deformations. In *Model S1*, the vertical deformations of the top and bottom of the embankment are similar for all the loading schemes applied, except for the lesser loading side of the embankment in

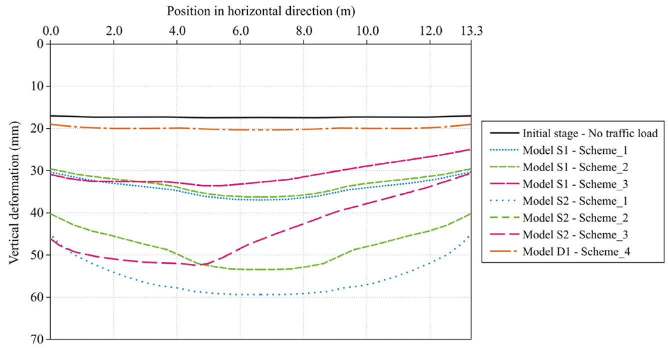

Fig. 5 *Vertical deformation of the base of the embankment*

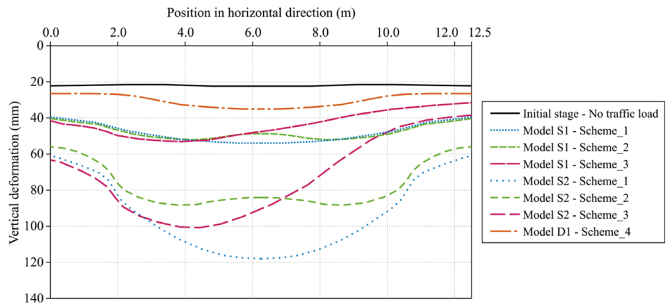

Fig. 6 *Vertical deformation of the top of the embankment*

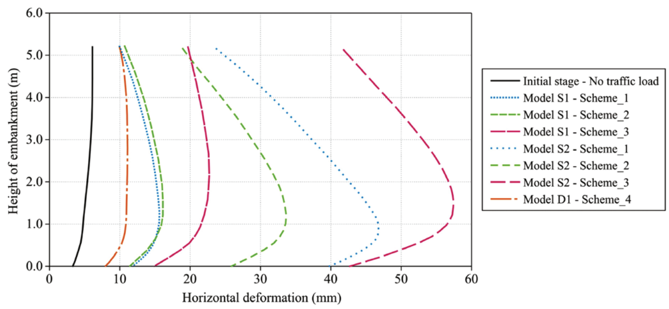

Fig. 7 *Horizontal deformation of the embankment*

Scheme 3. The vertical deformation of the bottom of the embankment was about 33 - 37 mm, and the vertical deformation of the top of the embankment was about 53 - 54 mm. The horizontal deformation of the embankment was about 15 mm in the case of *Model S1 - Scheme 1* and about 16 mm in the case of *Model S1 - Scheme 2*. In the case of *Model S1 - Scheme 3*, the horizontal deformation achieved was about 22.7 mm. In all three cases, the distribution area of 15 m^2 was applied to the TS. When the distribution area of 6.6 m^2 was used on the TS (*Model S2*), significantly greater vertical and horizontal deformations were achieved. The greatest vertical deformations of the top and the bottom of the embankment were achieved when the load was applied according to *Scheme 1*; however, in the case of the horizontal deformations, the greatest value was achieved when the load is applied according to *Scheme 3*.

3.1 Deformation of the embankment under cyclic loading

The cyclic loading was applied according to the scheme in Fig. 4, which tries to simulate real traffic loading according to actual traffic intensity measurements. The loads were defined according to *Scheme 4* of *Loading model C* (Fig. 3). The vertical deformations of the top and bottom of the embankment over time are presented for the initial 180 cycles in Figs. 8 and 9, respectively. A significant increase in the deformations was achieved in the initial cycles; then, the incremental displacement was reduced over time. After 324 cycles, the stable value of the deformations was achieved. It was assumed that the stable value of the deformations was achieved when the excess pore pressure decreased below 1 kPa. The change in the maximum pore pressure over time for the initial 180 cycles is shown in Fig. 10.

The vertical deformations of the top and bottom of the embankment and the horizontal deformation of the side of the embankment, which is reached after 10, 100, and 324 cycles, are shown in Figs. 11, 12, and 13. The results presented also include the deformations determined in the initial stage. In the case of cyclic loading, the deformations increase significantly in the initial cycles, but this increase decreases over time or on the number of cycles, respectively.

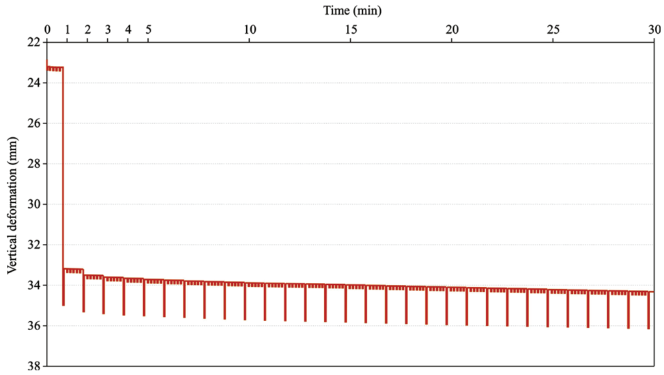

Fig. 8 *Vertical deformation of the top of the embankment over time - initial 180 cycles*

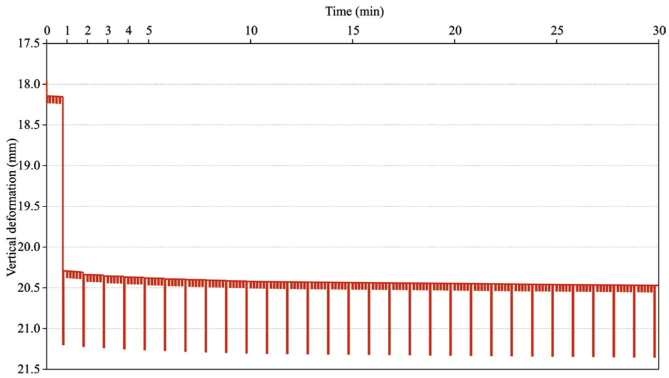

Fig. 9 *Vertical deformation of the base of the embankment over time - initial 180 cycles*

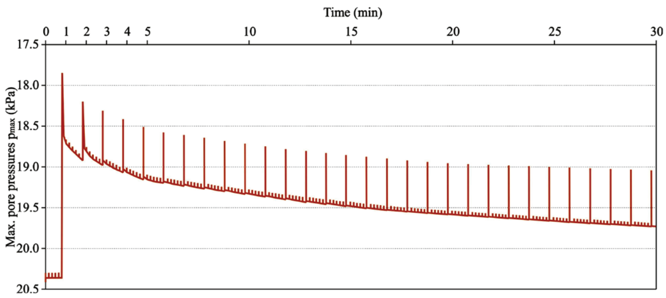

Fig. 10 *Course of the maximum pore pressure over time - initial 180 cycles*

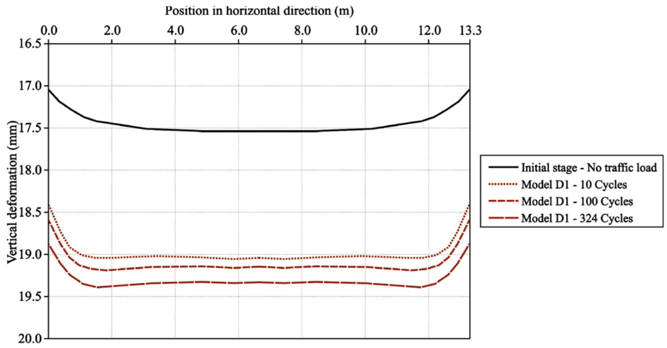

Fig. 11 *Vertical deformation of the base of the embankment in the case of cyclic loading*

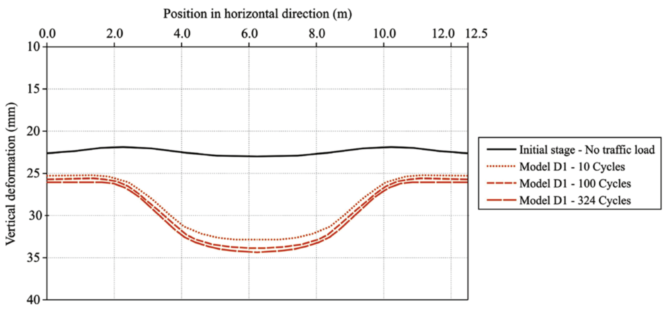

Fig. 12 *Vertical deformation of the top of the embankment in the case of cyclic loading*

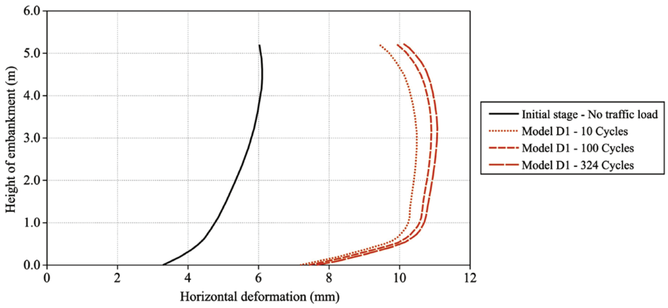

Fig. 13 *Horizontal deformation of the embankment in the case of cyclic loading*

The results more or less confirm that the deformations of the embankment are mainly caused by truck traffic. In the analysis presented, the subsoil of the embankment is relatively stiff and permeable. Based on the average traffic intensity, only one truck passes through the road section per minute. All these parameters lead to a relatively small number of cycles required to achieve a stable deformation. In the clayey subsoil, which requires a longer consolidation time and a greater intensity of truck traffic, the time and number of cycles needed to achieve a stable deformation can be significantly longer. The results also showed that in the case of the embankment design supported by GRS, the simulation of the cyclic loading permitted obtaining a magnitude of the estimated deformations that could occur under expected or design traffic loading.

4 CONCLUSIONS

The design of a road embankment supported by a geogrid retaining structure (GRS) with a passive facing system is based on verifications of the ultimate and serviceability limit states. The verification of the deformations of the embankment, as part of the serviceability limit state verifications, usually does not consider the acting variable traffic load. The visual monitoring of such constructions shows that some deformations from a traffic load occurs; however, the permanent monitoring for a given type of construction in the given region is missing. The results of the deformation analysis of the embankment supported by GRS under different types of loading showed that the type of loading and scheme have a significant impact on the deformations achieved. Different schemes based on the Load Model 1 of the EN 1991-2 standard were applied in the case of the static loading. If the load distribution from a tandem system (TS) to an area of 15 m^2 (which is often used in the practical design of given types of constructions) is applied, the vertical deformations of the top and bottom of the embankment are similar for all the loading schemes applied. In the horizontal deformations, the loading according to Scheme 3 led to determining the greatest horizontal deformations. If the load distribution from TS to an area of 6.6 m^2 is applied, according to the recommendations of the standard, the vertical and horizontal deformations of the embankment are significantly greater. The greatest vertical deformations of the embankment were achieved when the load was applied according to Scheme 1, and the greatest horizontal deformations were achieved when the load was used according to Scheme 3. The cyclic loading simulated the real traffic loading determined according to the traffic intensity measurements of the given road section. A one-minute segment included five personal vehicles and one truck. The results showed that in the given boundary conditions and properties of soil, the stable deformation of the embankment is reached after 324 cycles. The results showed that the deformation of the embankment is only a little higher than the deformation determined in the initial stage and visibly less than the deformation determined when different permanent static loading schemes were applied. The method presented can be suitably used in determining the estimated deformations from a traffic load that can occur under expected or design traffic loading.

REFERENCES

Abdelkrim, M. – Bonnet, G. – de Buhan, P. (2003) *A computational procedure for predicting the long term residual settlement of a platform induced by repeated traffic loading*. Computers and Geotechnics, Vol. 30, No. 6, pp. 463-476. https://doi.org/10.1016/S0266-352X(03)00010-7

Adam, M. - Pflanz, G. – Schmid, G. (2000) *Two- and three-dimensional modelling of half-space and train-track embankment under dynamic loading*. Soil Dynamics and Earthquake Engineering, Vol. 19, pp. 559-573. https://doi.org/10.1016/S0267-7261(00)00068-3

Adamec, J. – Snahnican, J. (2016) *Geotechnické konštrukcie na D1 Hričovské podhradie – Lietavská lúčka (Geotechnical structures on Hričovské podhradie – Lietavská lúčka D1 motorway)*. Engineering geology 2016, 16-17. June, 2016, Vysoke Tatry, Slovakia, pp. 24-31 [in Slovak].

Benz, M. (2007) *Small-strain Stiffness of Soils and Its Numerical Consequences*. Dissertation Thesis. Institute of Geotechnics, University of Stuttgart, 209 pp. Available at: https://www.igs.uni-stuttgart.de/dokumente/Mitteilungen/55_Benz.pdf, (accessed at 03/08/2021).

Dolinajova, K. – Snahnican, J. (2015) *Oporné múry vystužené geomrežami a dvojzákrutovou oceľovou sieťou vystavené vysokému zaťaženiu v seizmickej oblasti (Geogrid and Double Twist Steel Mesh Reinforced Soil Walls Subjected to High Loads in a Seismic Area)*. Proceedings of the 12th Slovak Geotechnical Conference: 55 Years of Geotechnical Engineering in Slovakia, 1-2 June, 2015, Bratislava, Slovakia, pp. 79-87 [in Slovak].

Drusa, M. – Vlcek, J. (2016) *Importance of Results Obtained from Geotechnical Monitoring for Evaluation of Reinforced Soil Structure - Case Study*. Journal of Applied Engineering Sciences, Vol. 6, No. 1, pp. 23-27. https://doi.org/10.1515/jaes-2016-0002

Han, G. – Gong, Q. – Zhou, S. (2015) *Soil Arching in a Piled Embankment under Dynamic Load*. International Journal of Geomechanics, Vol. 15, No. 6, 7 pp. https://doi.org/10.1061/(ASCE)GM.1943-5622.0000443

Holtz, R.D. – Lee, W.F. (2002) *Internal stability analyses of geosynthetic reinforced retaining walls*. Research Report, Agreement No. T9903, Task 95, Geosynthetic Reinforcement III, Washington State Transportation Center, USA, 466 pp. Available at: https://www.wsdot.wa.gov/research/reports/fullreports/532.1.pdf (accessed at 03/08/2021).

Ladicsova, E. (2017) *Deformations of Retaining Structures.* PhD Thesis, Faculty of Civil Engineering, STU in Bratislava, 196 pp [in Slovak].

Liu, P. – Wang, D. – Oeser, M. (2017) *Application of semi-analytical finite element method to analyze asphalt pavement response under heavy traffic loads*. Journal of Traffic and Transportation Engineering (English edition), Vol. 4, No. 2, pp. 206-214. https://doi.org/10.1016/j.jtte.2017.03.003

Mirmoradi, S.H. – Ehrlich, M. (2015) *Modeling of the Compaction-induced Stress on Reinforced Soil Walls*. Geotextiles and Geomembranes, Vol. 43, No. 1, pp. 82-88. https://doi.org/10.1016/j.geotexmem.2014.11.001

Pham, H.V. – Dias, D. (2019) *3D Numerical Modeling of a Piled Embankment under Cyclic Loading*. International Journal of Geomechanics, Vol. 19, No. 4, 15 pp. https://doi.org/10.1061/(ASCE)GM.1943-5622.0001354

PLAXIS 2D CE V21.01:1 (2021) Tutorial Manual. Available at https://communities.bentley.com/products/geotech-analysis/w/plaxis-soilvision-wiki/46137/manuals---plaxis (accessed at 03/08/2021).

Scotland, I. – Dixon, N. – Frost, M. – Wackrow, R. – Fowmes, G. – Horgan, G. (2014) *Measuring Deformation Performance of Geogrid Reinforced Structures Using a Terrestrial Laser Scanner*. Proceedings of 10th International Conference of Geosynthetics, September 2014, Berlin, Germany, 8 pp. Available at: https://www.researchgate.net/publication/286860094_Measuring_deformation_performance_of_geogrid_reinforced_structures_using_a_terrestrial_laser_scanner, (accessed at 03/08/2021).

Scotland, I. – Dixon, N. – Frost, M. – Fowmes, G. – Horgan, G. (2016) *Modelling Deformation During the Construction of Wrapped Geogrid Reinforced Structures*. Geosynthetics International, Vol. 23, No. 3, pp. 219-232. https://doi.org/10.1680/jgein.15.00049

Silber-Hasslacher, T. – Snahnican, J. (2019) *Active and Passive Facing Systems for Reinforced Soil Structures*. 13th Geosynthetics Annual Conference 2019, 7-8 Feb., Zilina, Slovakia, 9 pp. Available at: http://www.geosoul.sk/wp-content/uploads/2019/02/GEOSYNTETIKA2019_ACTIVE-AND-PASSIVE-FACING-SYSTEMS-FOR-REINFORCED-SOIL-STRUCTURES.pdf (accessed at 03/08/2021).

Stacho, J. – Sulovska, M. – Slavik, I. (2020) *Determining the Shear Strength Properties of a Soil-geogrid Interface Using a Large-scale Direct Shear Test Apparatus*. Periodica Polytechnica Civil Engineering, Vol. 64, No. 4, pp. 989-998. https://doi.org/10.3311/PPci.15766

Sulovska, M. – Stacho, J. (2019) *Design of Road Embankment Reinforced Using a Geogrid*. SGEM 2019. 19th International Multidisciplinary Scientific GeoConference. Vol. 19. Science and Technologies in Geology, Exploration and Mining, Sofia, Bulgaria, pp. 145-152. https://doi.org/10.5593/sgem2019/5.4/S22.047

Wang, Z. – Jacobs, F. – Ziegler, M. (2014) *Visualization of Load Transfer Behaviour between Geogrid and Sand Using PFC2D*. Geotextiles and Geomembranes, Vol. 42, No. 1, pp. 83-90. https://doi.org/10.1016/j.geotexmem.2014.01.001

Wu, J.T.H. (1994) *CTI-UCD-1-94: Design and Construction of Low Cost Retaining Walls: The Next Generation in Technology*. Colorado Transport Institute, Denver, Colorado, USA, 1994, p. 152. Available at: https://www.codot.gov/programs/research/pdfs/1994-research-reports/retainingwalls.pdf (accessed at 03/08/2021).

Xuecheng, B. – Hongguang, J. – Yunmin, Ch. (2010) *Accumulative deformation in railway track induced by high-speed traffic loading of the trains*. Earthquake Engineering and Engineering Vibration, Vol. 9, No. 3, pp. 319-326. https://doi.org/10.1007/s11803-010-0016-2

Zheng, L. – Hai-lin, Y. – Wan-ping, W. – Ping, Ch. (2012) *Dynamic stress and deformation of a layered road structure under vehicle traffic loads: Experimental measurements and numerical calculations*. Soil Dynamics and Earthquake Engineering, Vol. 39, pp. 100-112. https://doi.org/10.1016/j.soildyn.2012.03.002

Zhuang, Y. – Li, S. (2015) *Three-dimensional finite element analysis of arching in a piled embankment under traffic loading*. Arabian Journal of Geosciences, Vol. 8, No. 10, pp. 7751–7762. https://doi.org/10.1007/s12517-014-1748-5

sciendo Slovak Journal of Civil Engineering
Vol. 30, 2022, No. 3, 9 – 16
DOI: 10.2478/sjce-2022-0016

SIZING OF AN AUTONOMOUS INDIVIDUAL SOLAR WATER HEATER BASED IN ORAN, ALGERIA

Touhami BAKI[1*], Abdelfatah MARNI SANDID[2], Driss NEHARI[2]

Abstract

The study concerns an autonomous individual solar water heater installed in the Oran region in Algeria. Supplied by two sources of solar thermal and photovoltaic energy, this solar water heater provides domestic hot water for the needs of an average family of 6 people. A comparative approach was made to find the most adequate solution between increasing the surface area of the thermal solar panel or those of the photovoltaic panels, by analyzing the solar fraction and the efficiency of the thermal panels. The choice was make for a thermal panel with a surface area of 4 m² and complete with 16 photovoltaic panels, thus resulting in a total surface area of 14 m² to obtain an autonomous solar water heater powered only by solar energy. Another option was considered by incorporating a photovoltaic thermal panel, and substantial savings were found.

Address

[1] Mechanical Faculty, Gaseous Fuels and Environment Laboratory, USTO-MB, BP 1505, El-M'Naouer, Oran 31000, Algeria
[2] Dept. of Mechanical Engineering, University of Ain-Temouchent Belhadj Bouchaib, 46000, Ain-Temouchent, Algeria

* ***Corresponding author:*** touhami.baki@univ-usto.dz

Key words

- Solar energy,
- PT,
- PV,
- Solar water heater,
- Autonomous.

1 INTRODUCTION

The transition to renewable energy has been accentuated by the harmful effects of the consumption of fossil fuels; researchers and policymakers are looking for solutions from renewable energy systems. Solar energy is the most promising source due to its availability and abundance around the world; it can be easily converted into electricity and heat. Algeria, due to its geographical location, has significant potential in solar energy, it has a duration of sunshine varying from 2650 to 3500 hours per year and an average of received energy varying from 1700 to 2650 kWh / m² per year (Zidane et al., 2020).

Two distinct applications arise from solar energy, i.e., photovoltaic panels (PV) producing electricity and thermal panels (PT) producing heat. These two modules can be grouped together in the same box to produce electricity and heat in photovoltaic and thermal panels (PV/T) (Sultan and Ezfan, 2018). The energy consumption of buildings consumes one-third of the world's energy consumption (Good et al., 2015); this energy is supplied for the needs of electricity for air conditioning and the production of domestic hot water, which can be provided by thermal or photovoltaic panels or a combination of both.

Baki (2021) compared the performance of a domestic solar water heater with thermal panels in three regions in Algeria. Using the TRNSYS code (Rawat and Kesari, 2018) simulated the performance of a solar water heating system operating with solar energies of the PV, PT, and PV / T types. (Matuska and Sourek, 2017) studied the performance of solar water heaters coupled to resistance and photovoltaic panels and compared them with a solar water heater coupled to a thermal panel. (Chen et al., 2019) evaluated the performance of a solar water heater system and developed a model to simulate the power and heat output. (Huide et al., 2017) developed solar thermal, photovoltaic and hybrid simulation models, and experiments were carried out to validate the simulation. The performances of the three solar systems for residential applications were analyzed. (Khordehgah et al., 2020) simulated a PV / T to produce electricity and hot water for a house and studied the performance of the system. (Lazreg et al., 2020) simulated the performance of a solar water heater powered by a solar thermal panel and investigated the stratification of the temperature at the tank level. (Baki et al., 2021) have analytically studied a solar water heater installation for the domestic hot water needs of a family; the approach used compares the incoming and outgoing energies at the level of the tank. Formulations have been established, and the temperatures and energies were evaluated.

we have studied the performance of a solar water heater by making a dynamic simulation with the TRNSYS software; the parameters have been varied to find a compromise between a solar energy supply with PT thermal collectors and PV photovoltaic modules. The PT thermal collector was then replaced by a PV / T thermal and photovoltaic panel.

2 DESCRIPTION OF THE INSTALLATION

Domestic hot water is used for the needs of an individual dwelling housing an average family of 6 people. The total consumption is on average 40 liters per person per day, which is equivalent to 240 liters per day at a temperature of 60°C.

2.1 Details of the water heater

The water heater is powered by two energy sources, i.e., one thermal and the other photovoltaic. The thermal panel transfers energy to the heat exchanger located inside the tank by the circulation of the heat transfer fluid, while the pump only operates when the temperature at the outlet of the thermal panel is higher than the temperature of the water in the lower part of the balloon. The PV panel produces electricity, and the regulator dispatches it. If the hot water outlet temperature is sufficient, the energy captured is transmitted to the batteries for storage, but if the temperature is lower than the set temperature, the regulator provides electricity to the inverter to power the resistance. The electricity comes to the inverter from the panel during the day and as needed from the battery when the PV panel does not provide enough electricity or during the absence of sunlight. The operation of the installation is detailed in Figure 1.

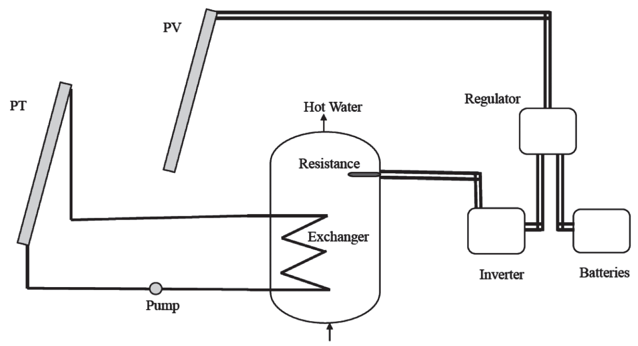

Fig. 1 *Installation diagram*

2.2 Weather data

The city of Oran is located on the southern coast of the Mediterranean Sea. Its climate is classified as Csa (Koppen-Geiger), which is of the warm temperate type with hot and dry summers and rainy and mild winters. The rainfall is low and varies between 330 and 400 mm per year. Figure 2 shows the variations in the average monthly temperature. It is around 12°C in the winter and 26° during the months of July and August. The average annual temperature is 18.1°C. The maximum solar radiation on a horizontal surface during the months of the year are shown in Figure 3; they vary from 560 W/m² in December to over 900 W/m² from April to September.

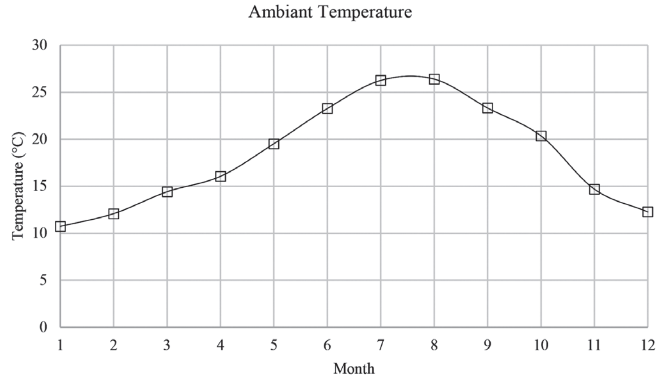

Fig. 2 *Average monthly temperature in Oran*

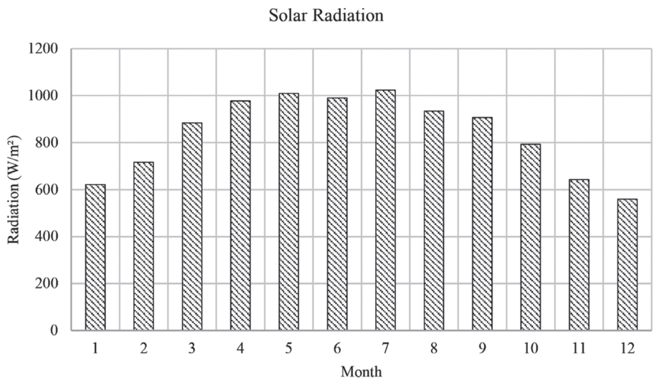

Fig. 3 *Monthly solar radiation in Oran*

2.3 Hot water demand load

Hot water needs are estimated at 240 liters of hot water per day at a temperature of 60°. The tank is supplied by city water at an average annual temperature of 18°; the heating is provided by the exchanger supplied by the thermal panel and the resistance supplied by the photovoltaic panel. The hourly distribution follows the profile in Figure 4. There are two consumption peaks on the order of 10% of the load between 8 and 11 a.m. in the morning and between 8 and 10 p.m. in the evening. The consumption is zero between 2 and 5 a.m. and fluctuates during the rest of the day between 2 and 4%.

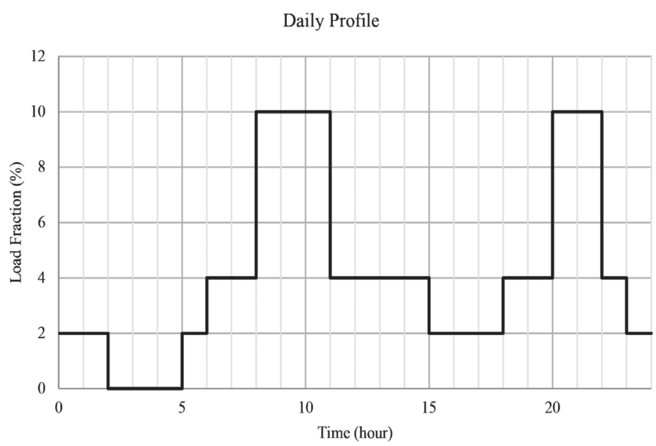

Fig. 4 *Load profile per day*

2.4 PV Module

For the simulation of the photovoltaic panels, a module composed of 36 monocrystalline cells in a series with an area of 0.89 m² were used. Their specifications are shown in Table 1. The peak power can reach 100 Wp; the energy supplied is either consumed by the resistance or stored in the batteries. The characteristics of the module indicated in Table 1 are taken from the default parameters of the TRNSYS code; the panel faces south and has an inclination angle of 35°.

Tab. 1 *PV module specification*

Module short-circuit current at reference conditions	6.5	amperes
Module open-circuit voltage at reference conditions	21.6	V
Reference temperature	298	K
Reference insulation	1000	W/m²
Module voltage at max power point and reference conditions	17	V
Module current at max power point and reference conditions	5.9	amperes
Temperature coefficient of Isc at (ref. cond)	0.02	-
Temperature coefficient of Voc (ref. cond.)	-0.079	-
Number of cells wired in series	36	-
Module temperature at NOCT	313	K
Ambient temperature at NOCT	293	K
Insulation at NOCT	800	W/m²
Module area	0.89	m²

2.5 PT Module

The thermal solar flat panels used in the simulation with characteristics taken from the TRNSYS code are presented in Table 2. The thermal panels transfer the heat captured from the solar rays to the hot fluid conveyed to the exchanger; the thermal panel is also oriented towards the south and inclined at 35°.

Tab. 2 *PT module specifications*

Fluid specific heat	4.190	kJ/kg.K
Efficiency mode	1	-
Tested flow rate	40.0	kg/hr.m²
Intercept efficiency	0.80	-
Efficiency slope	13.0	kJ/hr.m².K
Efficiency curvature	0.05	kJ/hr.m².K²
Optical mode 2	2	-
1st-order IAM	0.2	-
2nd-order IAM	0.0	-
Module area	1	m²

2.6 Hot water storage tank

The characteristics of the storage tank are listed in Table 3; this tank is a buffer stock for water to heat it. It is cylindrical in shape with a shell and two domed ends and contains a volume of 300 liters. The balloon is installed vertically and is equipped with several nozzles for the entry and exit of fluids and the mounting of regulation and control accessories. Inside the tank a helical-shaped copper exchanger with an internal diameter of 10 mm, an external diameter of 12 mm, and a length of 26 meters is mounted.

Tab. 3 *Characteristics of the storage tank*

Tank volume	0.3	m³
Tank height	1.25	m
Height of flow inlet	1.25	m
Height of flow outlet	0.0	m
Fluid specific heat	4.190	kJ/kg.K
Fluid density	1000.0	kg/ m³
Tank loss coefficient	3.0	kJ/hr.m².K
Fluid thermal conductivity	1.40	kJ/hr.m.K
Height of 1st aux. heater	1.0	m
Height of 1st thermostat	1.25	m
Set point temperature for element 1	60	C
Deadband for heating element 1	5.0	deltaC
Maximum heating rate of element 1	1800	kJ/hr
Number of internal heat exchangers	1	-
Heat exchanger inside diameter	0.01	m
Heat exchanger outside diameter	0.012	m
Total surface area of heat exchanger	1	m²
Heat exchanger length	26.0	m
Heat exchanger conductivity	1.40	kJ/hr.m.K

2.7 TRNSYS Diagram

The simulation is performed with TRNSYS software. The parameters are taken by default except for those indicated; the calculations are done by a time step of one hour over the entire length of the year. The assembly of the installation is shown schematically in Figure 5. The 60d type tank is connected to the 1b type thermal panel and to the 94a type electrical panel. The water is heated by the heat exchanger located inside the tank. If the temperature does not reach 60°C, the resistance is triggered.

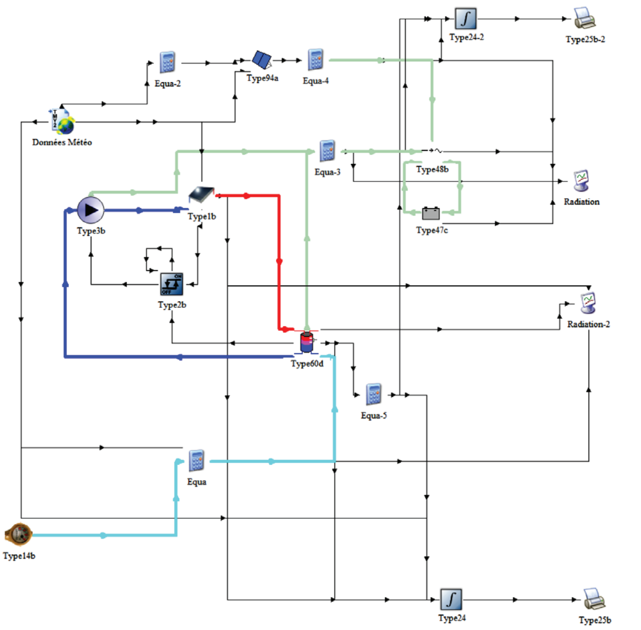

Fig. 5 *TRNSYS diagram*

2.8 Mathematical formulation

In order to compare the variables with each other, the following formulations of the energy and ratios were selected and are presented below.

The energy consumed, Q_c, is the quantity of energy that takes into account the water temperature at the inlet to the tank and which leaves it with the flowing of the hot water consumed; this quantity varies every hour. The total quantity will be the integration over a period of one day or one month.

$$Q_c = \int f\dot{m}c_p\left(T_{o\_b} - T_{i\_b}\right).dt \tag{1}$$

The instantaneous efficiency of a photovoltaic panel is calculated by the relationship:

$$\eta_{el} = \frac{UI}{A_{PV}G} \tag{2}$$

The efficiency of a thermal collector at any time is determined by the following relationship:

$$\eta_t = \eta_0 - a_1\frac{\Delta T}{G} - a_2\left(\frac{\Delta T}{G}\right)^2 \tag{3}$$

6

Likewise, we can determine the electrical energy collected over a period of a day or a month.

$$E_{el} = \int \eta_{el}A_{PV}G.dt \tag{4}$$

The useful thermal energy supplied by the thermal collector over a given period:

$$Q_u = \int \eta_t\, A_{PT}G.dt \tag{5}$$

represents the energy lost by the walls of the balloon, this value is determined by:

$$Q_p = \int U_t.S_t(T_i - T_L).dt \tag{6}$$

The necessary auxiliary energy supplied by the electrical resistance to bring the hot water to the temperature of 60 ° C is deduced from the following relation:

$$Q_{aux} = Q_p + Q_c - Q_u \tag{7}$$

We also define the total solar energy irradiated on a given surface by:

$$Q_s = \int A\,G.dt \tag{8}$$

The solar fraction is thus equal to:

$$SF = \frac{Q_c - Q_{aux}}{Q_c} \tag{9}$$

The efficiency of the overall thermal collector is:

$$\eta_{t\_g} = \frac{Q_u}{Q_s} \tag{10}$$

The efficiency of the overall photovoltaic panel is:

$$\eta_{el\_g} = \frac{E_{el}}{Q_s} \tag{11}$$

3 RESULTS AND DISCUSSION

3.1 Energy consumed

Figure 6 shows the monthly energy required for the supply of domestic hot water leaving the tank at 60°C over a period of one year. This energy remains relatively constant with slight variations from one month to another. The differences are due to variations in the temperature during the seasons. In the cold months the demand is high, i.e., around 340 kWh, unlike the hot months, where it decreases to 294 kWh. In February the demand is 310 kWh since there are fewer days than the other cool months. The annual demand is 38.8 GWh.

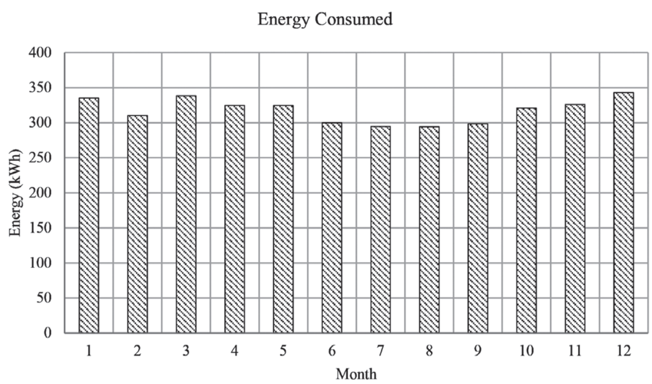

Fig. 6 *Energy consumed*

3.2 Solar thermal panel surface

Figure 7 shows the effect of the surface of the thermal solar panel on the solar fraction. By varying the surface of the solar panel from 1 to 10 m², we can notice an increase in the solar fraction, which starts from 0.11 and goes to 0.91. At the beginning the increase is significant; then it decreases and tends towards a given value. Table 4 shows a strong increase in the solar fraction going from 230 % to 24 %; then it decreases until it reaches 1% for an area going from 9 to 10 m².

Tab. 4 *Progression of the solar fraction*

PT	SF	Progression (%)
1	0.11	-
2	0.35	230
3	0.55	55
4	0.68	24
5	0.77	13
6	0.82	7
7	0.86	4
8	0.88	3
9	0.90	2
10	0.91	1

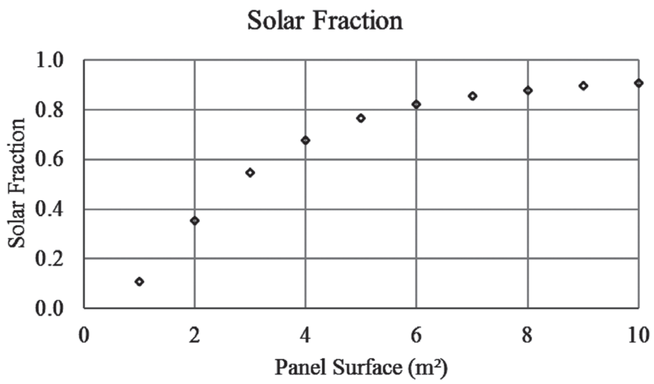

Fig. 7 *Effect of the area on the solar fraction*

3.3 Auxiliary energy requirements

Figure 8 shows the auxiliary energy requirements necessary to make up the difference in energy supplied by the thermal solar panels for a month. January is considered to be the most unfavorable month for solar radiation; with 1 m² of the surface area of the solar panel, the needs are on the order of 350 kWh. The more the surface increases, the solar energy needs to decrease to reach 115 kWh. The auxiliary energy must compensate for the need to bring the water to 60°C to compensate for thermal losses through the walls of the tank and provide the energy necessary for the operation of the solar loop circulation pump.

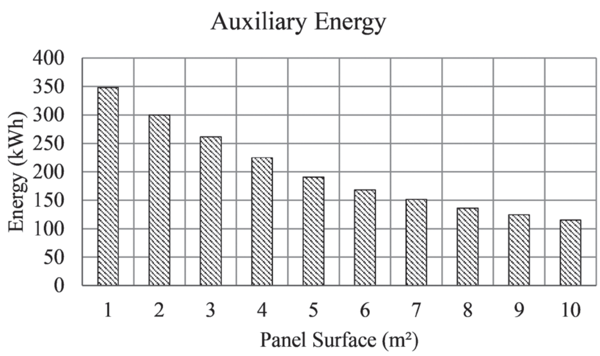

Fig. 8 *Auxiliary energy requirements*

3.4 Photovoltaic panel requirements

Table 5 shows the results of the simulation of the energy needs provided by the photovoltaic panels to meet the needs of the installation; 25 photovoltaic panels with an area of 0.89 m² will be needed to provide the necessary energy of 367 kWh for the month of January with 105% coverage. The more the surface of the thermal solar panels increases, the more the needs for the number of photovoltaic panels sharply decreases, i.e., between 4 m² and 7 m² of the surface of the thermal panels. The surface decreases by 2 photovoltaic panels.

Tab. 5 *Effect of the PT number*

PT Number	PT Efficiency	PV Number	PV Efficiency	kWh	kWh	Cover %
1	0.46	25	0.11	367	348	105
2	0.43	20	0.11	293	300	98
3	0.41	18	0.11	264	261	101
4	0.38	16	0.11	235	225	104
5	0.35	14	0.11	205	191	108
6	0.33	12	0.11	176	168	104
7	0.30	10	0.11	147	151	97
8	0.29	9	0.11	132	136	97
9	0.27	9	0.11	132	124	106
10	0.26	8	0.11	117	115	102

3.5 Panel performance

Figure 9 shows the efficiency of the thermal and photovoltaic panels. When the surface of the collector is increased, the efficiency of the thermal panels decreases. It goes from 0.46 for a surface of 1 m² to 0.26 for 10 m²; on the other hand, the yield of the photovoltaic panels remains constant and carries a value of 0.11.

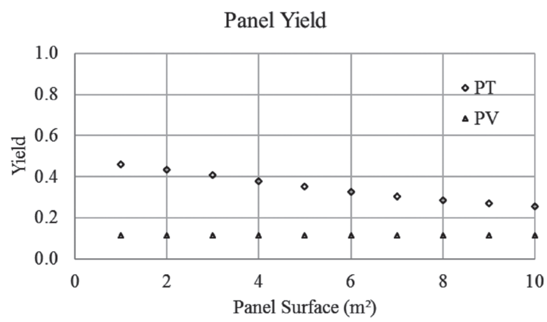

Fig. 9 *PT and PV performances*

3.6 Battery and regulator requirements

In order to allow for continuous operation, the electrical installation was connected to batteries. The connection of the inverter regulator manages the flows for the various components. The number of batteries required for total coverage is shown in Table 11; this number varies from 13 for a thermal collector area of 1 m² to 4 batteries for a thermal collector area of 10 m².

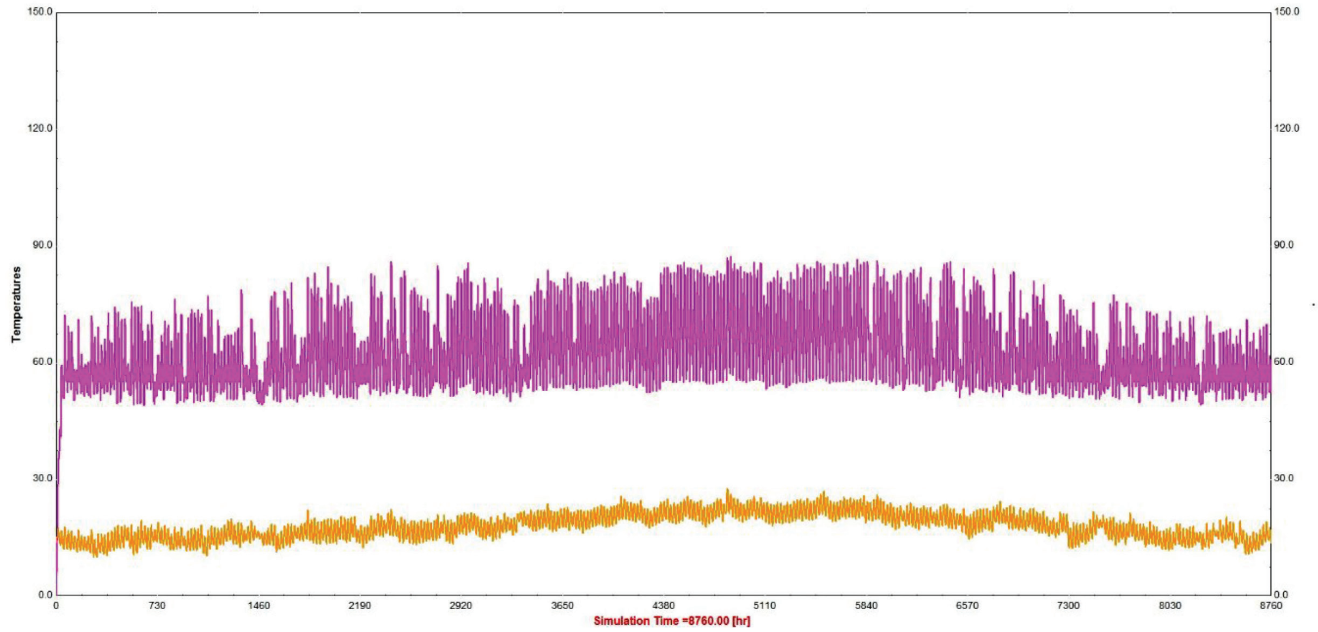

Fig. 10 *Inlet and outlet temperatures of the tank (inlet: yellow, outlet: purple)*

Tab. 6 *Number of batteries*

PT	PV		Battery
Number	Number	kWh	Number
1	25	367	13
2	20	293	10
3	18	264	9
4	16	235	8
5	14	205	7
6	12	176	6
7	10	147	5
8	9	132	5
9	9	132	5
10	8	117	4

3.7 Choice of the most adequate option

The most suitable option is to install a solar water heater equipped with thermal panels with a surface area of 4 m² and 16 photovoltaic panels; this choice is motivated by the fraction reached, which is 0.68, and the fact that the efficiency of the thermal panels is 0.38. It is in fact a compromise between these two criteria since when the surface of the thermal panel is increased, the fraction increases, and the thermal efficiency decreases. This choice of the appropriate option was also determined by the outlet temperature of the hot water tank, which must be under boiling. In the summer the temperature reaches values approaching 90°C, as shown in Figure 10, where we can observe the variations of the inlet and outlet temperatures inside the balloon.

4 STUDY OF THE SELECTED OPTION

4.1 Consumed and auxiliary energies

Figure 11 shows the energy necessary for the supply of hot water at 60°C; it remains relatively constant with slight variations from one month to another. This study was made for a the surface of a collector of 4 m² inclined at 35°. The energy is supplied by the solar panel to the tank, which if necessary, is filled by the electric resistance installed in the tank. In the same Figure we note that the auxiliary energy is at a maximum in January and December and a minimum during the summer period.

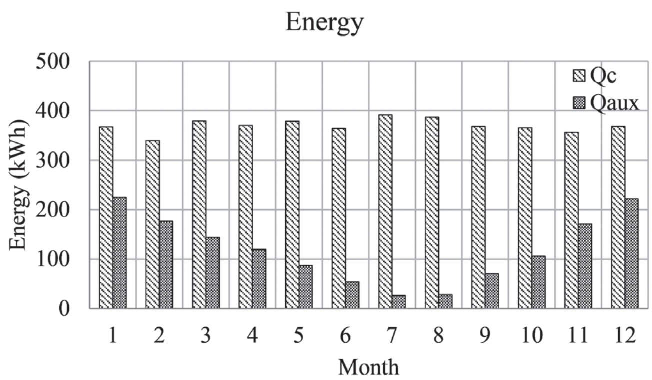

Fig. 11 *Consumed and auxiliary energies*

4.2 Energy supplied by the panels

Figure 12 shows histograms of the energy supplied by the thermal collector and the photovoltaic panels as well as the radiation of solar energy over an area of 1 m². The surface area allocated to the thermal collector is 4 m² and that of the photovoltaic panels is 16 panels of 0.89 m², resulting in a total surface area of 14.24 m². The sum of the captured energies is injected into the tank to heat the domestic hot water and meet consumption needs.

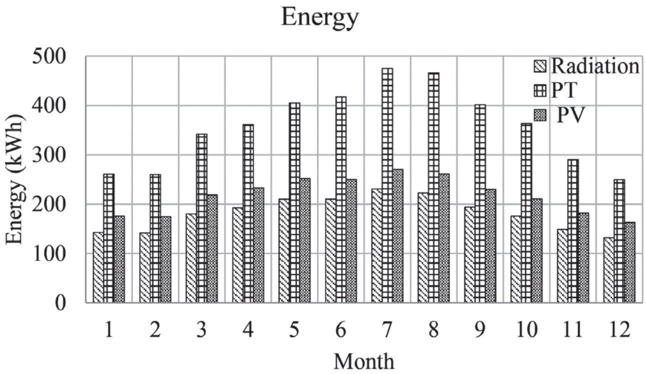

Fig. 12 *Energy supplied*

Over the months the energy captured is irregular and depends strongly on radiation; it is at a maximum in the summer and a minimum in the winter. The sizing of the photovoltaic panels is done on the basis of the least favorable month, which is the month of January. The auxiliary energy needs must be met during this month.

4.3 Efficiency

Figure 13 shows us the monthly variations in the efficiency of the thermal and photovoltaic panels. The efficiency of the thermal panel varies during the year between 0.35 and 0.42 with a maximum in August and minimum values during the rest of the year. For the months of January and December, the yield of the photovoltaic panel is, on the other hand, stable during the year and varies between 0.11 and 0.12. The minimum values are obtained during the summer; the average value of the annual yield is 0.38 for the thermal panel and 0.11 for the photovoltaic panel.

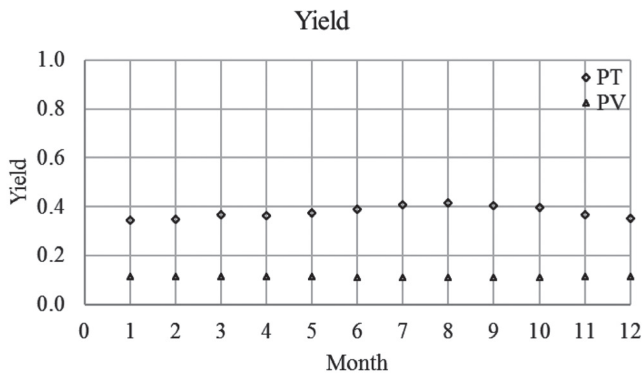

Fig. 13 *Performance of the panel*

4.4 Case study of a PV/T panel

In the diagram of the simulation in 5, the 1b type thermal solar panel is replaced by a 50b type thermal photovoltaic panel with all the connections, the characteristics of which are indicated in Table 7. The panel supplies heat through the solar loop and electricity to the regulator; additional electrical energy is provided by the photovoltaic panels.

The simulation results are presented in Table 8; they show the energy supplied by the PV/T panel and that supplied by the 12 PV panel modules during all the months of the year. The sum of these energies covers the months from January. The need for auxiliary energy or the saving of 4 photovoltaic panels was achieved by installing a PV/T instead of a PT.

Tab. 7 *PV/T characteristics*

Mode	2	-
Collector Area	4	m²
Collector Efficiency Factor	0.96	-
Fluid Thermal Capacitance	4.19	kJ/kg.K
Collector plate absorbance	0.92	-
Number of glass covers	1	-
Collector plate emittance	0.09	-
Loss coefficient for bottom and edge losses	1.1	kJ/hr.m².K
Collector slope	35	degrees
Transmittance absorbance product	0.9	-
Temperature coefficient of PV cell efficiency	0.0032	any
Temperature for cell reference efficiency	25	C
Packing factor	0.8	-
Cell efficiency at reference conditions	0.2	-

Tab. 8 *Simulation results of the installation with PV/T*

Month	(PV)	(PV/T)		Cover
	kWh	KWh	kWh	%
1	176	70	225	110
2	174	70	176	138
3	218	87	144	212
4	233	93	119	273
5	252	101	87	406
6	250	100	54	650
7	270	109	27	1420
8	261	105	28	1314
9	229	92	71	455
10	211	85	106	279
11	182	73	171	149
12	163	65	222	103

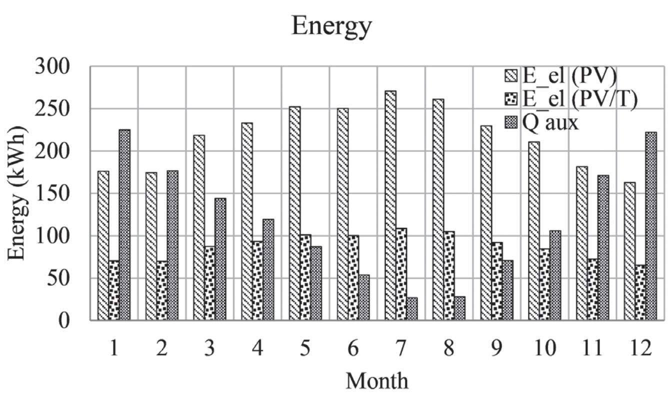

Fig. 14 *Electrical and auxiliary energies of PV/T*

Figure 14 shows the auxiliary energy needs during the months and the electrical energies supplied by the PV and PV/T panels; the auxiliary energy needs are at a maximum in the month of January and can be covered by the sum of the electric energies of the PV panels and PV/T.

5 CONCLUSION

The sizing of an autonomous solar water heater supplying a house housing 6 people under its roof has been studied. The energy coverage is based on the two types of solar energy, i.e., thermal and photovoltaic. A comparative study was made between a thermal panel surface area varying from 1 to 10 m² and the additional surface area of photovoltaic panels, resulting in an adequate option consisting of having a thermal panel surface area of 4 m² and additional auxiliary energy supplied by 16 photovoltaic panels. The heat collector was subsequently replaced by a PV/T panel; positive results have been achieved from the savings energy.

REFERENCES

Baki, T. (2021) *Comparison of the performance of a domestic solar water heater in different climates in Algeria*. Present Environment & Sustainable Development, Vol. 15. N° 1. pp. 143-151. DOI:10.15551/pesd2021151011

Baki, T. – Tebbal, M. – Berrebah, H. (2021) *Following the balloon temperature of a solar heater installed in Oran, Algeria.* Turkish Journal of Electromechanics & Energy, Vol. 6. N°2, pp. 74-80.

Chen, X. – Wang, W. – Luo, D. – Zhu, C. (2019) *Performance evaluation and optimization of a building-integrated photovoltaic/thermal solar water heating system for exterior shading: A case study in South China*. Applied Sciences, Vol. 9. N° 24, pp. 1-13. DOI:10.3390/app9245395

Good, C. – Andresen, I. – Hestnes, A. G. (2015) *Solar energy for net zero energy buildings–A comparison between solar thermal, PV and photovoltaic–thermal (PV/T) systems*. Solar Energy, Vol. 122, pp. 986-996. DOI: 10.1016/j.solener.2015. 10.013.

Huide, F. – Xuxin, Z. – Lei, M. – Tao, Z. – Qixing, W. – Hongyuan, S. (2017) *A comparative study on three types of solar utilization technologies for buildings: Photovoltaic, solar thermal and hybrid photovoltaic/thermal systems*. Energy Conversion and Management, Vol. 140. pp. 1-13. DOI: 10.1016/j.enconman.2017.02. 059

Khordehgah, N. – Żabnieńska-Góra, A. – Jouhara, H. (2020) *Energy performance analysis of a PV/T system coupled with domestic hot water system*. *Chem Engineering*, Vol. *4. N°* 2. Pp. 1-14. DOI: 10.3390/chemengineering 4020022.

Lazreg M. – Baki T. – Nehari D. (2020) *Effect of Parameters on the Stratification of a Solar Water Heater*. In: Belasri A., Beldjilali S. (eds) ICREEC 2019. Springer Proceedings in Energy. Springer, Singapore. DOI: 10.1007/978-981-15-5444-5_15

Matuska, T. – Sourek, B. (2017) *Performance analysis of photovoltaic water heating system*. International Journal of Photoenergy, Vol. 2017. pp. 1-10. DOI:10.1155/2017/7540250

Rawat, P. – Kesari, J. P. (2018) *Analysis of Three Types of Solar Systems: PV, Flat Plate Thermal, and Hybrid PV-T Using TRNSYS Model*. International Journal of Advanced Research in Science, Engineering and Technology, Vol. 5 N° 6. pp. 6257-6265.

Sultan, S.M. – Efzan, (2018) *M.N.E. Review on recent Photovoltaic/Thermal (PV/T) technology advances and applications*. Solar Energy, Vol. 173, pp. 939–954. DOI:10.1016/j.solener.2018.08.032

Zidane, T. E. K. – Adzman, M. R. – Tajuddin, M. F. N. – Zali, S. M. – Durusu, A. – Mekhilef, S. (2020) *Optimal design of photovoltaic power plant using hybrid optimisation: a case of south Algeria*. Energies, Vol. 13, N° 11, pp. 1-28. DOI: 10.3390/en13112776.

Slovak Journal of Civil Engineering

Vol. 30, 2022, No. 3, 17 – 26
DOI: 10.2478/sjce-2022-0017

ESTIMATION OF THE UPLIFT RESISTANCE FOR AN UNDER-REAMED PILE IN DRY SAND USING MACHINE LEARNING

Sharad DADHICH[1*], Jitendra Kumar SHARMA[2], Madhav MADHIRA[3]

Abstract

Under-reamed piles are extensively used to resist uplift forces and settlements. The objective of the present study is to develop various machine learning models (linear and non-linear) and determine the best model to estimate the ultimate uplift resistance of under-reamed piles embedded in cohesionless soil. The machine learning models were developed considering the following input parameters: the density index, dry density, base diameter, angle of an enlarged base with a vertical axis, shaft diameter, and embedment ratio. A linear equation is proposed to estimate the ultimate uplift resistance based on Multivariate Linear Regression analysis with a mean absolute error equaling 0.25kN and 0.50kN for loose and dense sands respectively. The Decision Tree Regression model provides an excellent degree of accuracy with a mean absolute error of 0.02kN and 0.02kN in cases of loose and dense sands respectively.

Address

[1] MTech student, Department of Civil Engineering, Rajasthan Technical University, Kota,

[2] Professor, Department of Civil Engineering, Rajasthan Technical University, Kota

[3] AICTE-INAE Distinguished Visiting Professor, Professor Emeritus, JNT University; Visiting Professor IIT, Hyderabad

* ***Corresponding author:*** sdadhich.mtech18@rtu.ac.in

Key words

- Under-reamed pile,
- Uplift resistance,
- Machine learning,
- Multivariate linear regression and decision tree regression.

ABBREVIATIONS

A	Exponent
ANN	Artificial neural network
C	Regression constant
D_b	Base diameter (in mm)
DE	Dimensional distinct element
D_r	Density Index (in %)
D_s	Shaft diameter (in mm)
DTR	Decision Tree Regression
MAE	Mean absolute error (in kN)
m_i	Regression coefficient
ML	Machine learning
MLP	Multi-layer perceptron
MLR	Multivariate Linear Regression
MPR	Multivariate Polynomial Regression
P_{ult}	Ultimate uplift resistance (in kN)
r^2-score	Coefficient of determination
RBM	Restricted Boltzmann Machine
ReLu	Rectified linear unit (activation function)
RFR	Random Forest Regression
RMSE	Root mean square error (in kN)
SVR	Support Vector Regression
Tanh	Hyperbolic tangent (Activation function)
UBL	Upper Bound Limit
Xi	Input variable
Y	Output variable
B	Angle of enlarged base with horizontal axis (in ^{o})
γ_d	Dry density (in %)
Λ	Embedment ratio

1 INTRODUCTION

Generally, high-rise structures such as transmission towers or elevated buildings are exposed to lateral loads (shear) and overturning moments due to wind, waves, or a combination of both, in addition to any axial load. Therefore, the conventional piles (bored and driven piles) supporting these buildings have to resist these lateral forces, moments, and uplift loads. In general, these loads and moments act on the piles simultaneously (Nazir et al., 2015; Mosquera et al., 2015; Milad et al., 2015). Therefore, many theoretical methods have been developed for the assessment of pile behavior under different load combinations (Arulmoli et al., 2004; Borel, 2001; Tolinson and Wood, 2008). Under-reamed piles are a special type of pile with enlarged bell-shaped bases generally constructed with concrete. Typically, the pile base is in the form of a reversed cone, which provides an enlarged plain area to resist uplift forces (Harris and Madabhushi, 2015).

Many research laboratory and field tests have been executed to analyze the performance of piles subjected to uplift forces. However, there are comparatively few papers in the literature that deal with under-reamed piles subjected to uplift forces (Zhao et al., 2011; Sego et al., 2003; Grigoryan and Chinenkov, 1990; Bartholomew, 1977). The uplift resistance of under-reamed piles implanted in the sand can be obtained based on hypothetical and semi-empirical approaches (Nazir et al., 2014; Nazir et al., 2015). Field and small-scale laboratory tests have been performed to obtain appropriate results (Sakr, 2015; Tshua and Aoki, 2010). A full-scale test was conducted to validate the results based on a laboratory (small scale) test (Briancon and Simon, 2011). Sego et al. (2003) inspected an under-reamed pile located on ice permafrost. The outcomes verified that uplift resistance can be substantially increased through a bell-shaped base. Honda et al. (2011) applied a 2D distinct element (DE) analysis to assess the uplift resistance of single and multi-belled under-reamed piles and developed a theoretical solution using Upper Bound Limit (UBL) analysis. Chae et al. (2012) investigated the uplift resistance of under-reamed piles by conducting pullout tests on tension piles. When comparing the results from field tests, hypothetical methods, and three-dimensional finite element analysis, it was found that theoretical methods over-estimate the uplift capacity. Yao and Yao and Chen (2014) developed an elastoplastic analytical model, which was better than the previous theoretical solutions. Lin et al. (2015) analyzed the failure pattern and demonstrated that the slip surface was established at a small space away from the apparent surface of the pile. In some cases, researchers have used geosynthetics to enhance the uplift resistance (Ahmadi and Bonab, 2012; Horpibulsuk and Niramitkornburee, 2010; EI and Nazir, 2006). Tafreshi et al. (2014) concluded that pile length can be condensed considerably using geosynthetics as a reinforcement.

Many studies based on artificial neural networks (ANN) are available to forecast capacities of single piles and groups of piles (Suman et al., 2016; Momeni et al., 2015; Shahin, 2014; Shahin, 2016; Kordjazi et al., 2014; Bazair et al., 2012), dynamic pile capacity (Alkroosh and Nikraz, 2014; Zhang et al., 2010), and settlement of piles (Liang et al., 2005; Nejad et al., 2009). Rahman et al. (2001) developed an ANN model to predict the uplift resistance of a suction pile. To ensure the strength and steadiness of the structures, uplift resistance and capacity against horizontal forces along with vertical forces are required for a design of the foundation system. Unlike compression and lateral resistance, the uplift resistance of piles has not been extensively investigated.

In the present study, an effort has been made to develop an improved approach using machine learning (ML) algorithms for predicting the uplift resistance of under-reamed piles embedded in dry cohesionless sand. Linear (multivariate linear and polynomial regression) and non-linear (support vector, decision tree and random forest regression) machine learning algorithms have been developed, and the performance of each ML model is evaluated in its training and testing phase using three statistical parameters i.e., mean absolute error (MAE), root mean absolute error (RMSE), and coefficient of determination (r^2-score). The results of the study are also compared with an existing multilayer perceptron (MLP) neural network model.

2 DATA COLLECTION

The data used in this study was acquired from small-scale laboratory tests executed by Nazir et al. (2014). The aim of the research is to determine the uplift capacity of under-reamed piles against uplift forces. The dataset consists of 432 results, which were undertaken in both loose and dense dry cohesionless sand. The various combinations of the following parameters were considered for the experimental study: an enlarged base pile with a base angle (β) of 30°, 45°, and 60°; an enlarged base diameter (D_b) of 75 mm, 100 mm, 125 mm, and 150 mm; a shaft diameter (D_s) of 30 mm, 40 mm, and 50 mm; and an embedment ratio (λ) of 0 to 5. The soil parameters considered for the testing purpose were the dry unit weight (γ_d) and density index (D_r). In this study the input parameters used for developing the machine learning models are shown in Table 1.

Tab. 1 Physical parameters used for determination of the uplift resistance

Material parameters	Symbol	Magnitude		Unit
Soil		Loose	Dense	
Dry unit weight	γ_d	14.70	18.00	kN/m³
Density index	D_r	35	85	%
Pile				
Shaft diameter	D_s	30, 40 and 50		Mm
Base diameter	D_b	75, 100, 125 and 150		Mm
Base angle	$Β$	30, 45 and 60		Degree (°)
Embedment ratio	$Λ$	0, 1, 2, 3, 4 and 5		--
Uplift resistance	P_{ult}	Output Parameter		kN

3 METHODOLOGY

Machine learning (ML) is a subsection of artificial intelligence (AI), which assists computers to learn based on a training dataset. The process of learning starts with an analysis of the data and successively obtaining a mathematical relationship between the input and output variables in linear and non-linear forms. ML is broadly divided into three groups as shown in Fig. 1.

In this study supervised learning techniques were used to ascertain and model the relationship between the input and output variables by fitting linear and non-linear models to the experimental data.

3.1 Linear Model

In this type of supervised machine learning, a linear relationship is obtained between the input and output variables, while minimizing the mean absolute error (MAE). If the input variables

ARTIFICIAL INTELLIGENCE				
MACHINE LEARNING				DEEP LEARNING
Supervised Learning		Unsupervised Learning	Reinforcement Learning	• Artificial Neural Network • Recurrent Neural Network • Convolution Neural Network • Generative Adversarial Network • Restricted Boltzman Machine
• Classification KNN, SVM, DTC, RFC, Naïve based and Logistic regression	• Regression Linear regression MLR & MPR Non-linear regression SVR, DTR & RFR	• Clustering SVD, PCA & K-means • Association • Hidden Markov	• Dynamic Programming • Monte Carlo Analysis	

Fig. 1 *Types of Machine Learning*

are in a linear relationship with the output variables, the equation obtained can be written as:

(a). Multivariate Linear Regression Model
$$Y = C + \sum_{i=1}^{n} m_i \times X_i \quad (1)$$

(b). Multivariate Polynomial Regression Model
$$Y = C + \sum_{i=1,a=0}^{i=n,a=m} m_i * X_i^a \quad (2)$$

where 'Y' is the output variable; 'Xi' is the input variable; 'm_i' is the regression coefficient; 'a' is the exponent; and 'C' is the bias or regression constant.

3.2 Non-linear Models

In this type of machine learning algorithm, a non-linear relationship is obtained between the input and output variables using curves. In this paper Support Vector Regression (SVR), Decision Tree Regression (DTR), and Random Forest Regression (RFR) models were trained and tested for predicting the uplift resistance of the under-reamed piles.

3.2.1 Support Vector Regression (SVR) model

Despite reducing the error as in linear regression, SVR permits the flexibility to define an acceptable error and will define an appropriate line (multi-dimensional plane or hyperplane) to fit the data. The objective of SVR is to minimize the coefficient of weights associated with each input, while constraining the error within the permissible limit (Eq. 3). SVR is briefly explained in Smola and Scholkopf (2004).

$$Minimize = \frac{1}{2} \times ||w_i||^2, while\ |Y_i - w_i \times X_i| \leq \boldsymbol{\varepsilon} \quad (3)$$

3.2.2 Decision Tree Regression (DTR) model

A decision tree is a model, which predicts an output value based on the variables input. The basic terminology of the Decision Tree Regression model is presented in Fig. 2. The parent node or root node is the very first node of the DT, which contains the whole dataset. The splitting starts from the root node. The decision node is a sub-node, which divides into further sub-nodes. It is also referred to as a child

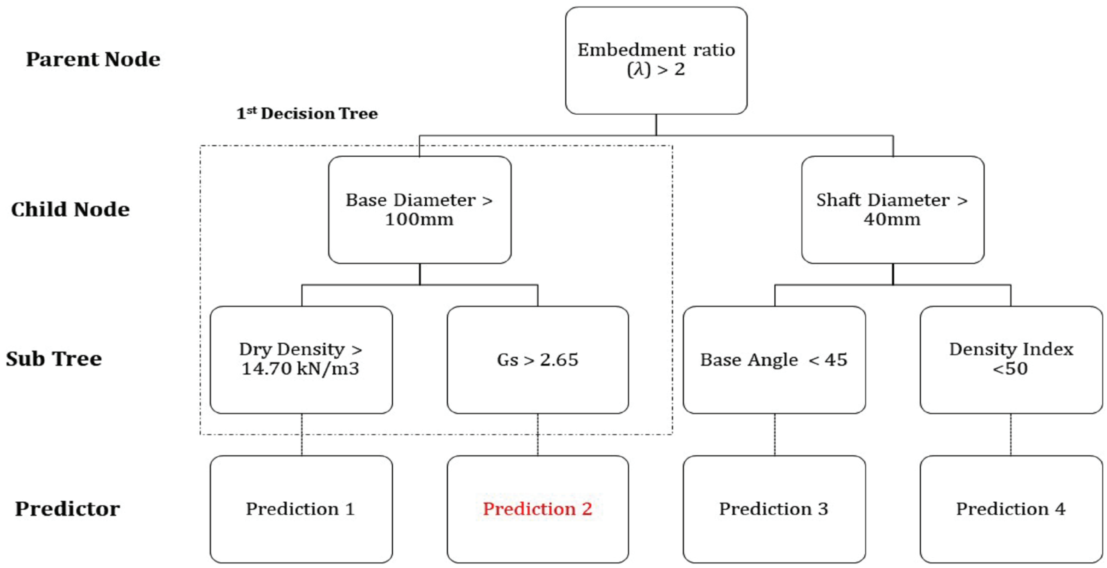

Fig. 2 *Basic Terminology of the Decision Tree Regression model*

node. The leaf node or the predictor is the node which contains the decision; there is no more splitting after that node. Splitting is the process of dividing the node into sub-nodes. Pruning is the process of deactivating any sub-node. A sub-tree is a portion of an entire tree, which consists of a parent node and a child node. In the DTR model, the recursive partitioning of the dataset starts from the root node. Each node is divided into a child node in order to reduce standard deviation (entropy). The splitting of the node is based on the information gain (IG), which is the difference between the impurity of the parent node and sum of impurities of the child node. Therefore, the objective function in the DTR model is an information gain. Finally, the data is pure or free from any impurity at each leaf node. The decision tree is briefly explained in Tso and Yau (2007).

3.2.3 Random Forest Regression (RFR) model

Random Forest Regression (RFR) includes numerous decision trees (Fig. 3), and the prediction is completely based on the average of the outputs received from every decision tree. It belongs to the circle of relatives of ensemble machine learning algorithms that expect a reaction (in this case, the respective soil parameters) from a set of predictors (matrix of training records) by creating multiple decision trees (DTs) and aggregating their results. Every Decision Tree inside the Random Forest is independently constructed while using the unique bootstrap sample of the training data, whereas other machine learning algorithms (e.g., bagging and bootstrapping) use the nice split among all the predictors for node splitting. RFR chooses the best split in a random manner. The creation of this additional randomness decreases the correlation among the trees inside the forest and therefore will increase the level of accuracy and predictability. Additionally, RFR calls for no assumption of the probability distribution of the target predictors as with linear regression and is powerful towards non-linearity, although over-fitting can also arise in instances where noisy data is being modeled.

4 ARCHITECTURE OF THE MODELS

In this study various machine learning models (linear and non-linear) have been developed. The performance of a model not only depends on the dataset but also on its architecture. To obtain the optimal performance of the model, several iterations were performed to select the best model architecture. Data pre-processing techniques were used to clean the data, and hyper parameter tuning was used to obtain the best model architecture. The architecture of the different models is shown in Table 2 as follows:

Tab. 2 *Architecture of the different models*

Sr. No.	Model	Architecture (Parameters)
1.	Multivariate Linear Regression model	Default
2.	Multivariate Polynomial Regression model	Degree (a) = 2
3.	Support Vector Regression model	Kernel = rbf and linear
4.	Decision Tree Regression model	random_state = 1
5.	Random Forest Regression model	random_state = 1 n_estimators =40

5 PERFORMANCE EVALUATION

Various machine learning algorithms (linear and non-linear) have been developed to predict the ultimate uplift resistance of under-reamed piles. A performance evaluation was carried out on each phase (training and testing phases), and the overall performance of the model was evaluated. For this purpose, different statistical parameters (Hassanvand et al., 2018; Saadat et al., 2018; Dadhich et al., 2021), i.e., Mean Absolute Error (MAE), Root Mean Square Error (RMSE), and the Coefficient of Determination (r^2-score) were used and estimated as follows:

$$Mean\ Absolute\ Error\ (MAE) = \frac{1}{n} * \sum_{i=0}^{n} (y_{actual} - y_{predict} \quad (4)$$

$$Root\ Mean\ Square\ Error = \sqrt{\frac{1}{n} * \sum_{i=0}^{n} (y_{actual} - y_{predictec}} \quad (5)$$

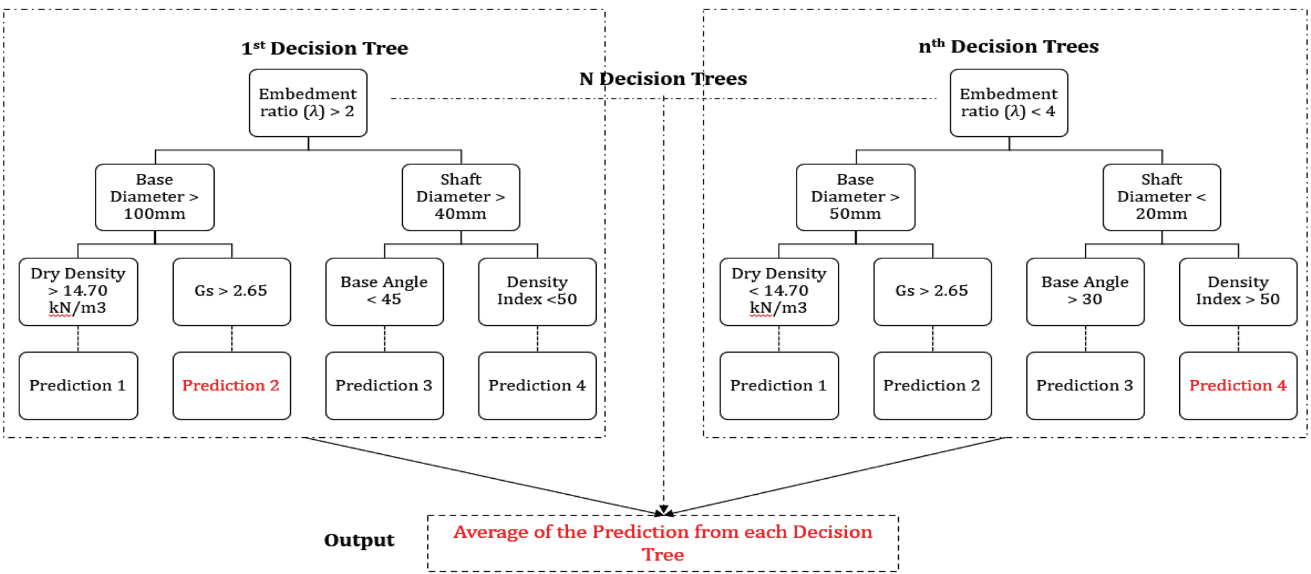

Fig. 3 *Basic Architecture of the Random Forest Regression model*

$$r^2 - score = 1 - \frac{\left(\sum_{i=1}^{n}(y_{predicted} - y_{mean})^2\right)}{\left(\sum_{i=1}^{n}(y_{actual} - y_{mean})^2\right)} \quad (6)$$

$$Overall_{pf} = Train_{Fraction} * Train_{pf} + Test_{Fraction} * Test_{pf} \quad (7)$$

where '$y_{predict}$ is the predicted output; y_{actual} is the actual value; y_{mean} is the mean of the actual value, and n is the total number of the dataset.

6 RESULTS AND DISCUSSION

The dataset consisting of 432 test results (Nazir et al., 2015), 216 each of the loose and dense sands, was used for generating different machine learning algorithms. A correlation matrix was generated and used to determine the dependency of the output variable on the input variables. The results of the correlation matrix are shown below in Table 3.

The ultimate uplift resistance (P_{ult}) of the under-reamed pile (Table 3) positively depends on the base diameter (D_b) and embedment ratio (λ).

Tab. 3 *Correlation coefficient matrix*

	γ_d	D_r	D_s	β	λ	D_b	P_{ult}
γ_d	1						
D_r	1	1					
D_s	0	0	1				
β	0	0	0	1			
λ	0	0	0	0	1		
D_b	0	0	0	0	0		
P_{ult}	.23	.23	-0.02	-0.03	0.66	0.42	1

6.1 Results of the Machine Learning Algorithms

LOOSE SAND

6.1.1 Linear model

Linear and polynomial regression analyses were performed to estimate the ultimate uplift resistance (P_{ult}) of the under-reamed pile embedded in the sand. Based on the multivariate linear regression analysis, the equation proposed to estimate P_{ult}, is

$$P_{ult}(kN) = .138 \times D_S - 2.43 \times \beta + 254.13 \times \lambda + 10.5 \times D_b \quad (8)$$

In Table 4, it can be seen that the training phase is much more accurate than the testing phase. In the multivariate polynomial regression model, the MAE and r²-scores were 0.09kN and 0.97 in the training and 0.10kN and 0.95 in the testing phases, respectively. In the case of the multivariate linear regression model, the corresponding values for these two parameters were 0.27kN and 0.69 and 0.25kN and 0.71. The MPR model performs better than the MLR model and can be used to estimate the ultimate uplift resistance (P_{ult}). The training and testing phase results were plotted against the actual values as shown in Figs. 4 and 5 for the MLR and MPR models respectively. The training phase results of the MLR deviate largely from the regression line (Fig. 4).

Tab. 4 *Results of the Linear Regression model*

Linear Model	Statistical Parameter	Phase		Overall Performance
		Training	Testing	
Multivariate Linear Regression	MAE	0.27	0.25	0.26
	RMSE	0.35	0.31	0.34
	r²-score	0.69	0.71	0.70
Multivariate Polynomial Regression	MAE	0.09	0.10	0.09
	RMSE	0.11	0.13	0.11
	r²-score	0.97	0.95	0.96

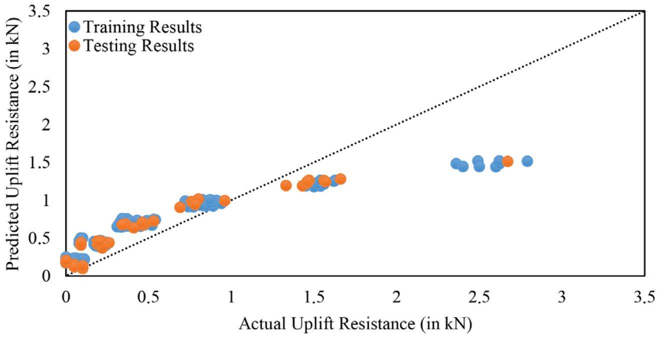

Fig. 4 *Results of the Multivariate Linear Regression model (MLR)*

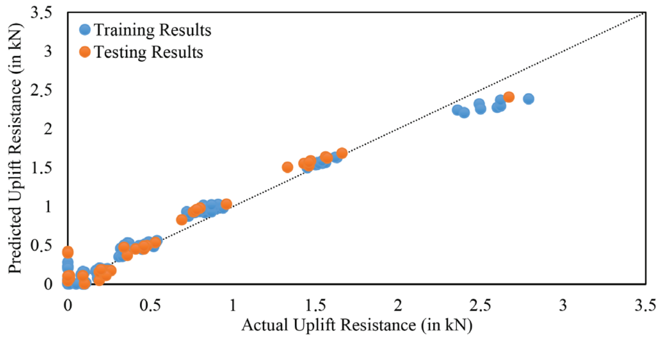

Fig. 5 *Results of the Multivariate Polynomial Regression model (MPR)*

The actual and predicted outputs for the multivariate polynomial regression model (Fig. 5) in the training and testing phases are nearly equal and deviate less from the regression line. The same results are also evident in Table 4. Thus, it can be concluded that the MPR model performs better than the MLR model.

6.1.2 Non-linear model

Non-linear regression modeling was carried out using Support Vector Regression (SVR), Decision Tree Regression (DTR), and Random Forest Regression (RFR). The performances of the different models evaluated are given in Table 5.

It can be seen in Table 5 that the training phase is much more accurate than the testing phase. In the training phase of the support vector regression model, MAE is 0.07kN with an r²-score of 0.97, while in the testing phase, MAE is 0.08kN with an r²-score of 0.96, which shows the better performance of the support vector regression model over the linear regression models.

Fig. 6 shows the performance of the support vector regression model in the training and the testing phases. It can be seen in Fig. 6 that the SVR model performs well in the training and testing phases.

Tab. 5 *Results of the non-linear regression model*

Non-linear Model	Statistical Parameter	Phase		Overall Performance
		Training	Testing	
Support Vector Regression model	MAE	0.07	0.08	0.07
	RMSE	0.12	0.12	0.12
	r^2-score	0.97	0.96	0.97
Decision Tree Regression model	MAE	0.00	0.02	0.005
	RMSE	0.00	0.038	0.01
	r^2-score	1.00	0.9957	0.9989
Random Forest Regression model	MAE	0.006	0.02	0.009
	RMSE	0.012	0.039	0.02
	r^2-score	0.99	0.9955	0.991

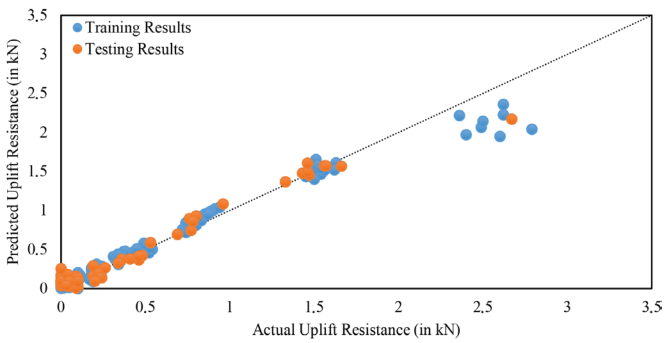

Fig. 6 *Results of the Support Vector Regression (SVR) model*

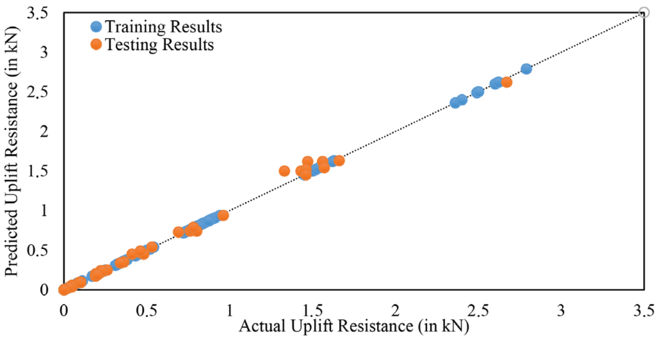

Fig. 7 *Results of the Decision Tree Regression model (DTR)*

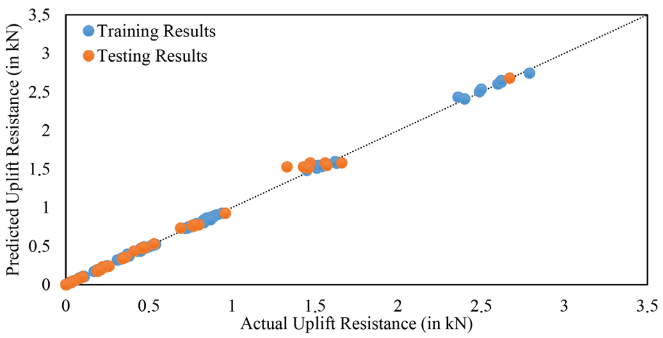

Fig. 8 *Results of the Random Forest Regression model (RFR)*

In the case of the decision tree regression model, MAE in the training phase is 0.00 with an r^2-score of 1.00, while it is 0.02 with an r^2-score of 0.9957 in the testing phase. This shows that the decision tree regression model best fits the data as a polynomial regression model. The performance of the Random Forest Regression model is satisfactory in the training phase as well as in the testing phase with a MAE of 0.006kN and 0.02kN respectively.

Fig. 7 shows that the training and testing phases of the decision tree regression model overlap the regression line, which shows that the actual and predicted values are highly compatible with each other.

Fig. 8 shows the performance of the Random Forest Regression model (RFR). It can be seen that the performance of the non-linear regression model is consistent in the training and testing phases. Out of the 5 models, the decision tree regression mode performs the best in the training and testing phases with a minimum MAE and a RMSE with a maximum r^2-score.

DENSE SAND

6.1.3 Linear model

A linear and polynomial regression analysis was performed to estimate the ultimate uplift resistance (P_{ult}) of the under-reamed pile embedded in the sand. Based on the Multivariate Linear Regression analysis, the following equation is proposed to estimate P_{ult}, which is shown in Eq. 9.

$$Pult\ (in\ kN) = .166 \times Ds - 6.9 \times \beta + 513.71 \times \lambda + 19.75 \times Db \quad (9)$$

Tab. 6 *Results of the Linear regression model*

Linear Model	Statistical Parameter	Phase		Overall Performance
		Training	Testing	
Multivariate Linear Regression	MAE	0.50	0.50	0.50
	RMSE	0.64	0.61	0.63
	r^2-score	0.72	0.75	0.73
Multivariate Polynomial Regression	MAE	0.15	0.16	0.15
	RMSE	0.20	0.23	0.21
	r^2-score	0.97	0.96	0.97

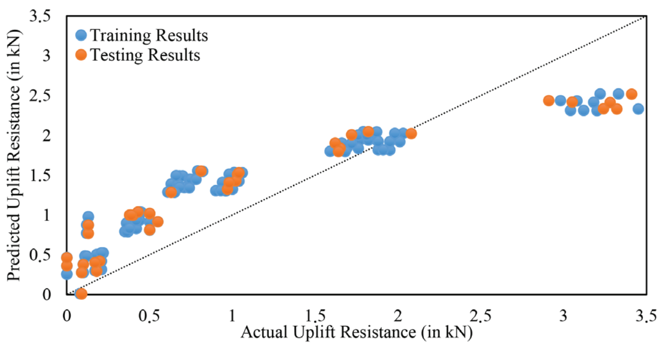

Fig. 9 *Results of the Multivariate Linear regression model (MLR)*

It can be seen in Table 6 that the training phase is much more accurate than the testing phase. In the training phase of the polynomial regression model, the MAE is 0.15kN with an r^2-score of 0.97, but in the testing phase, the MAE is 0.16kN with an r^2-score of 0.96. In the case of the linear regression model, the MAE in the training phase is 0.50kN with an r^2-score of 0.72, while in the testing phase, it is 0.50kN with an r^2-score of 0.75. This shows that the Multivariate Polynomial Regression model (MPR) performs

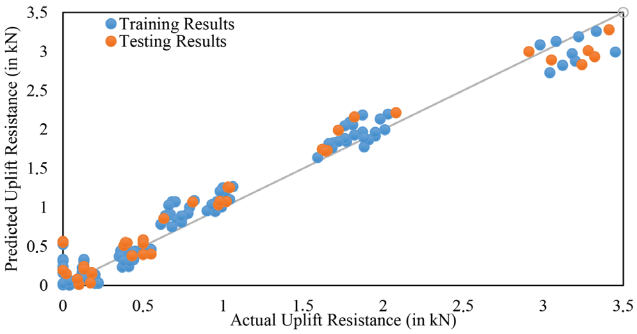

Fig. 10 *Results of the Multivariate Polynomial Regression model (MPR)*

better than the Multivariate Linear Regression model (MLR) and can be used to estimate the ultimate uplift resistance. The training and the testing results are plotted against the actual results as shown in Figs. 9 and 10 for the MLR and MPR models. It can be seen that in Fig. 9 for MLR, the training results highly deviate from the 1:1 line (regression line).

It can be seen in Fig. 10 that in the training and the testing phases, the actual and predicted values are nearly equal and deviate less from the regression line, which is also evident from Table 6.

6.1.4 Non-linear model

Non-linear regression modeling was carried out using Support Vector Regression (SVR), Decision Tree Regression (DTR), and Random Forest Regression (RFR). The performance of the different models is evaluated in Table 7 as follows:

Tab. 7 *Results of the Non-linear regression model*

Non-linear Model	Statistical Parameter	Phase		Overall Performance
		Training	Testing	
Support Vector Regression model	MAE	0.46	0.47	0.46
	RMSE	0.71	0.69	0.70
	r^2-score	0.66	0.68	0.66
Decision Tree Regression model	MAE	0.00	0.02	0.005
	RMSE	0.00	0.04	0.01
	r^2-score	1.00	0.99	0.9989
Random Forest Regression model	MAE	0.02	0.04	0.025
	RMSE	0.04	0.07	0.04
	r^2-score	0.99	0.99	0.99

It can be seen in Table 7 that the training phase is much more accurate than the testing phase. In the training phase of the support vector regression model, MAE is 0.46kN with an r^2-score of 0.66, while in the testing phase, MAE is 0.47kN with an r^2-score of 0.68, which shows the poor performance of the Support Vector Regression model over the linear regression models.

In the case of the Decision Tree Regression model, MAE in the training phase is 0.00kN with an r^2-score of 1.00, while in the testing phase it is 0.02kN with an r^2-score of 0.99. This shows that the Decision Tree Regression model best fits the data as a polynomial regression model. The performance of the Random Forest Regression model is satisfactory in the training phase as well as in

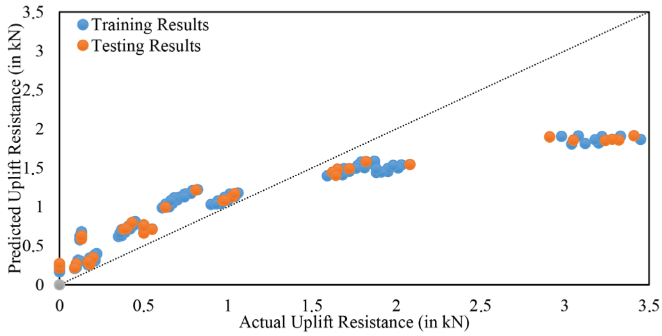

Fig. 11 *Results of the Support Vector Regression model (SVR)*

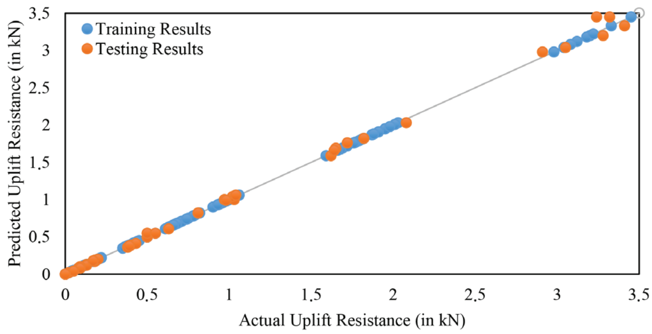

Fig. 12 *Results of the Decision Tree Regression model (DTR)*

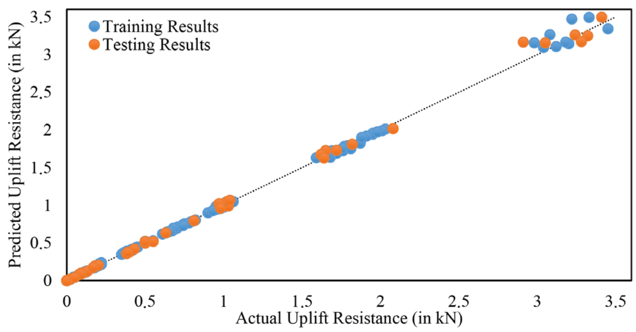

Fig. 13 *Results of the Random Forest Regression model (RFR)*

the testing phase with an MAE of 0.02kN and 0.04kN, respectively. Fig. 11 shows the performance of the Support Vector Regression model in the training and testing phase. It can be seen in Fig. 11 that the SVR model performs poorly in the training and testing phases.

Fig. 12 shows the training and testing phases of the Decision Tree Regression model. The results of the DTR model overlap the regression line. This shows that the actual and predicted values are compatible with each other and that the DTR model can be used to predict the uplift resistance of the under-reamed pile.

Fig. 13 shows the performance of the Random Forest Regression model (RFR). It can be seen that the performance of the non-linear regression model is consistent in the training and testing phases. Out of all 5 models, the Decision Tree Regression model performs the best in the training and testing phases with a minimum MAE and RMSE and with a maximum r^2-score.

6.2 Comparison with existing MLP Neural Network Model

Moayedi and Rezaei (2019) developed a formula using a multilayer perceptron (MLP) artificial neural network (ANN) to pre-

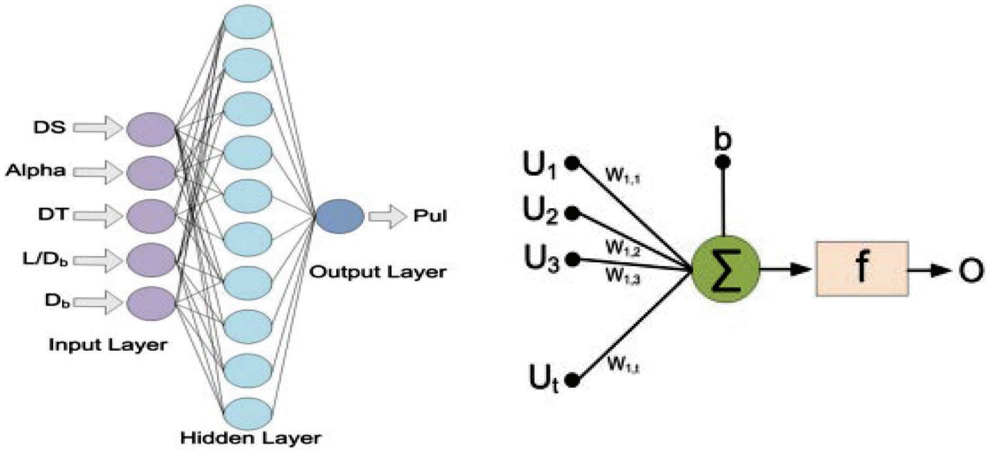

Fig. 14 *Architecture of the MLP neural network and mathematical structure of a neuron, Courtesy Moayedi and Rezaei, 2019*

$$Pul = abs(-1.3419 * tansig(0.012753 * Ds - 1.4692 * Alpha - 0.12898 * DT + 1.2804 * ER + 0.65553 * Db + 10.8701) - 0.010131 * tansig(0.27276 * Ds - 0.0022046 * Alpha + 0.4184 * DT + 1.1763 * ER - 0.16275 * Db - 5.9077) + 0.00083048 * tansig(1.7705 * Ds - 1.194 * Alpha + 2.0979 * DT - 0.17825 * ER - 0.57311 * Db + 2.3419) - 1.9967 * tansig(-0.00096448 * Ds + 0.00073819 * Alpha - 0.45228 * DT - 0.47458 * ER + 0.037422 * Db - 0.13683) + 2.796 * tansig(-0.0030848 * Ds - 0.0017212 * Alpha - 0.071306 * DT + 0.34076 * ER + 0.011644 * Db - 2.1228) - 1.3461 * tansig(0.002462 * Ds + 1.5202 * Alpha - 0.26247 * DT + 3.2369 * ER - 0.98471 * Db + 15.6301) - 1.8572 * tansig(0.00080372 * Ds + 0.0018985 * Alpha - 0.20589 * DT - 0.67674 * ER + 0.035409 * Db + 1.6114) - 1.8427 * tansig(-0.0033276 * Ds - 0.0016549 * Alpha + 0.49151 * DT + 0.54666 * ER + 0.025507 * Db - 10.5262) - 1.8289 * tansig(-0.00047678 * Ds - 0.0018453 * Alpha - 0.20311 * DT + 0.62268 * ER - 0.038398 * Db + 6.8981) - 0.46146 * tansig(0.0041671 * Ds + 0.0040608 * Alpha + 0.18664 * DT - 2.7405 * ER - 0.11086 * Db + 3.3236) + 2.0822) \tag{10}$$

dict the ultimate uplift resistance of an under-reamed pile, which is given in Eq. 10. The architecture of the neural network used for the prediction of the ultimate uplift resistance consists of one input layer, one hidden layer, and one output layer. The activation function used at each node was Tansig (a built-in function in MATLAB), and the abs function was used to acquire the absolute value of the output. The architecture of the MLP model generated and the mathematical functioning of each neuron are shown in Fig. 14 (Moayedi & Rezaei, 2019).

Table 8 shows a comparison of the MLP neural network model, the polynomial regression model (MPR), and the Decision Tree Regression model (DTR). MAE and RMSE are the minimum for the Decision Tree Regression model with a maximum r^2-score of 0.9987 (~1).

Fig 15 shows the variations of MAE and RMSE for the different models. It is evident that the proposed Decision Tree Regression model (DTR) best predicts the ultimate uplift resistance (P_{ult}).

Tab. 8 *Comparison of the ML model with the existing MLP NN model*

Model	Input Parameter	Output Parameter	Statistical Parameter	
MLP neural network, Moayedi and Rezaei (2019)	D_b, D_s, β and λ	P_{ult}	MAE	0.26
			RMSE	0.89
			r^2-score	0.99
MPR model	D_b, D_s, β, λ and γ_d	P_{ult}	MAE	0.15
			RMSE	0.21
			r^2-score	0.97
DTR model	D_b, D_s, β, λ and γ_d	P_{ult}	MAE	0.005
			RMSE	0.01
			r^2-score	0.9989

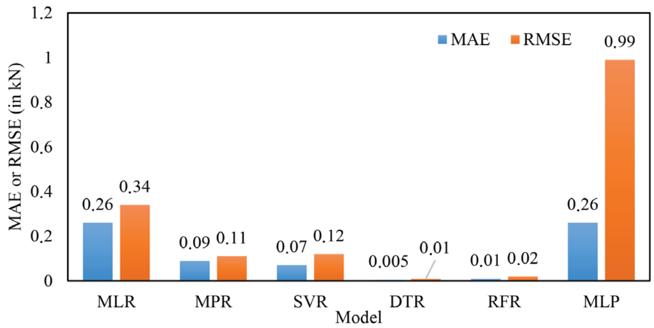

Fig. 15 *Comparative bar chart for the various models*

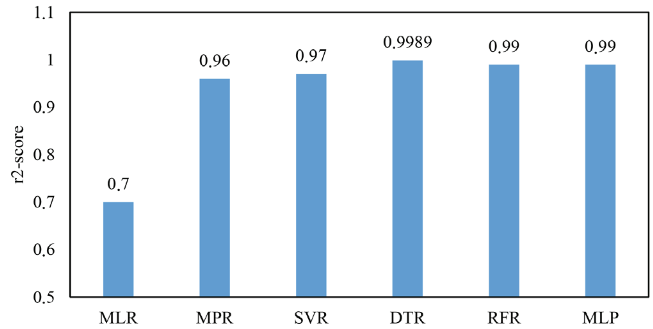

Fig. 16 *Comparative bar chart for the coefficient of determination*

7 CONCLUSIONS

Machine Learning algorithms were used for predicting the ultimate uplift resistance (P_{Ult}) of under-reamed piles. Various linear and non-linear machine learning models were compared to find the best model, and the best model was selected based on the overall MAE, RMSE, and r^2-score. Based on the study, the following conclusions can be drawn:

1. The correlation study shows that the uplift resistance of the under-reamed pile is chiefly dependent on the embedment ratio (λ) and base diameter (D_b).
2. The RMSE of the MPR model is 0.11kN with a 0.96 r^2-score in the case of loose sand, while in dense sand, it is 0.21kN with a 0.97 r^2-score, which shows the compatible performance of the MPR model for predicting the ultimate uplift resistance (P_{Ult}) of the under-reamed piles.
3. The SVR model was found to be the worst performing model among all the models developed and cannot be used for the ultimate uplift resistance (P_{Ult}) of the under-reamed piles.
4. The MAE of the Decision Tree Regression model in the training and testing phases is 0.00kN and 0.02kN, respectively, with an overall r^2-score nearly equal to 1 in the training and testing phases, which shows the compatible performance of the model for the prediction of the ultimate uplift resistance (P_{Ult}) of the under-reamed piles.
5. The outcomes from this study prove that the Decision Tree Regression model (DTR) can be used as a consistent solution due to the fast computation and precise results for the ultimate uplift resistance (P_{Ult}) of the under-reamed piles.

REFERENCES

Ahmadi, H., - Hajialilue-Bonab, M. (2012) *Experimental and analytical investigations on bearing capacity of strip footing in reinforced sand backfills and flexible retaining wall.* Acta Geotechnica, Vol. 7, No. 4, pp. 357-373.

Alkroosh, I., - Nikraz, H. (2014) *Predicting pile dynamic capacity via application of an evolutionary algorithm.* Soils and Foundations, Vol. 54, No. 2, pp. 233-242.

Arulmoli, K., - Martin, G. R., - Gasparro, M. G., - Shahrestani, S., - Buzzoni, G. (2004) *Design of pile foundations for liquefaction-induced lateral spread displacements.* Geotechnical Engineering for Transportation Projects, pp. 1673-1681.

Bartholomew, R. F. (1977) *Enlarged base piles form an important class*. Structural Engineer, 55(12), A7-A7.

Baziar, M. H., - Kashkooli, A., - Saeedi-Azizkandi, A. (2012) *Prediction of pile shaft resistance using cone penetration tests (CPTs)*. Computers and Geotechnics, Vol. 45, pp. 74-82.

Borel, S. (2001) *Calcul des fondations mixtes semelles-pieux sous sollicitation horizontale.* International Conference on soil mechanics and geotechnical engineering, pp. 847-850.

Briançon, L., - Simon, B. (2012) *Performance of pile-supported embankment over soft soil: full-scale experiment.* Journal of Geotechnical and Geoenvironmental Engineering, Vol. 138, No. 4, pp. 551-561.

Chae, D. - Cho, W. - Na, H. Y. (2012) *Uplift capacity of belled pile in weathered sandstones.* International Journal of Offshore and Polar Engineering, Vol. 22, No. 04.

Dadhich, S. - Sharma, J. K. - Madhira, M. (2021) *Prediction of ultimate bearing capacity of aggregate pier reinforced clay using machine learning.* International Journal of Geosynthetics and Ground Engineering, Vol. 7, No. 2, pp. 1-16.

El Sawwaf, M., - Nazir, A. (2006) *The effect of soil reinforcement on pullout resistance of an existing vertical anchor plate in sand.* Computers and Geotechnics, Vol. 33, No. 3, pp. 167-176.

Grigoryan, A. A., - Chinenkov, Y. A. (1990) *Bearing capacity and settlements of bored piles with enlarged bases in collapsible soils.* Proceedings of the 9th Danube-European Conference on Soil Mechanics and Foundation Engineering, pp. 203-210.

Harris, D. E., & Madabhushi, G. S. P. (2015) *Uplift capacity of an under-reamed pile foundation.* Proceedings of the Institution of Civil Engineers Geotechnical Engineering, Vol. 168, No. 6, pp. 526-538.

Hassanvand, M. - Moradi, S. - Fattahi, M. - Zargar, G. - Kamari, M. (2018) *Estimation of rock uniaxial compressive strength for an Iranian carbonate oil reservoir: Modeling vs. artificial neural network application.* Petroleum Research, Vol. 3, No. 4, pp. 336-345.

Honda, T. - Hirai, Y., - Sato, E. (2011) *Uplift capacity of belled and multi-belled piles in dense sand.* Soils and Foundations, Vol 51, No. 3, pp. 483-496.

Horpibulsuk, S., - Niramitkornburee, A. (2010) *Pullout resistance of bearing reinforcement embedded in sand.* Soils and Foundations, Vol. 50, No. 2, pp. 215-226.

Kordjazi, A. - Nejad, F. P. - Jaksa, M. B. (2014) *Prediction of ultimate axial load-carrying capacity of piles using a support vector machine based on CPT data.* Computers and Geotechnics, Vol. 55, pp. 91-102.

Li, Q. - Fang, Y. - Song, J. - Wang, J. (2010) *Measuring Technology and Mechatronics Automation.* IEEE, Vol. 3, pp. 13-14.

Liang, B. L. - Gao, Y. - Zhu, L. - Lv, G. B. - Li, X. (2005) *Prediction of pile displacement using PSO algorithm and artificial neural networks.* China Univ Geosciences Press, Wuhan.

Lin, J. G. - Hsu, S. Y. - Lin, S. S. (2015) *The new method to evaluate the uplift capacity of belled piles in sandy soil.* Journal of Marine Science and Technology, Vol. 23, No. 4, pp. 16.

Milad, F. - Kamal, T. - Nader, H. - Erman, O. E. (2015) *New method for predicting the ultimate bearing capacity of driven piles by using Flap number.* KSCE Journal of Civil Engineering, Vol. 19, No. 3, pp. 611-620.

Moayedi, H., - Rezaei, A. (2019) *An artificial neural network approach for under-reamed piles subjected to uplift forces in dry sand.* Neural Computing and Applications, Vol. 31, No. 2, pp. 327-336.

Moghaddas Tafreshi, S. N. - Javadi, S. - Dawson, A. R. (2014) *Influence of geocell reinforcement on uplift response of belled piles.* Acta Geotechnica, Vol. 9, No. 3, pp. 513-528.

Momeni, E. - Nazir, R. - Armaghani, D. J. - Maizir, H. (2015) *Application of artificial neural network for predicting shaft and tip resistances of concrete piles.* Earth Sciences Research Journal, Vol. 19, No. 1, pp. 85-93.

Mosquera, Z. S. - Tsuha, C. D. H. - Schiavon, J. A. - Thorel, L. (2015) *Discussion of Field investigation of the axial resistance of helical piles in dense sand*. Canadian Geotechnical Journal, Vol. 52, No. 8, pp. 1190-1194.

Nazir, R. - Chuan, H. S. - Niroumand, H. - Kassim, K. A. (2014) *Performance of single vertical helical anchor embedded in dry sand*. Measurement, Vol. 49, pp. 42-51.

Nazir, R. - Moayedi, H. - Mosallanezhad, M., - Tourtiz, A. (2015) *Appraisal of reliable skin friction variation in a bored pile.* Proceedings of the Institution of Civil Engineers-Geotechnical Engineering, Vol. 168, No. 1, pp. 75-86.

Nazir, R. - Moayedi, H. - Pratikso, A. - Mosallanezhad, M. (2015) *The uplift load capacity of an enlarged base pier embedded in dry sand.* Arabian Journal of Geosciences, Vol. 8, No. 9, pp. 7285-7296.

Nejad, F. P. - Jaksa, M. B. - Kakhi, M. - McCabe, B. A. (2009) *Prediction of pile settlement using artificial neural networks based on standard penetration test data.* Computers and geotechnics, Vol., 36, No. 7, pp. 1125-1133.

Rahman, M. S. - Wang, J. - Deng, W. - Carter, J. P. (2001) *A neural network model for the uplift capacity of suction caissons.* Computers and Geotechnics, Vol. 28, No. 4, pp. 269-287.

Saadat, S. - Seyedmohammadi, J. - Esmaeelnejad, L. (2018) *Selection of a suitable soft computing model for estimation of soil cation exchange capacity.* Communications in Soil Science and Plant Analysis, Vol. 49, No. 21, pp. 2664-2679.

Sakr, M. (2015) *Relationship between installation torque and axial capacities of helical piles in cohesionless soils.* Canadian Geotechnical Journal, Vol. 52, No. 6, pp. 747-759.

Sego, D. C. - Biggar, K. W. - Wong, G. (2003) *Enlarged base (belled) piles for use in ice or ice-rich permafrost.* Journal of cold regions engineering, Vol. 17, No. 2, pp. 68-88.

Shahin, M. (2014) *Artificial intelligence for modelling load-settlement response of axially loaded bored piles.* Numerical Methods in Geotechnical Engineering, pp. 491-495.

Shahin, M. A. (2016) *State-of-the-art review of some artificial intelligence applications in pile foundations.* Geoscience Frontiers, Vol. 7, No. 1, pp. 33-44.

Smola, A. J., - Schölkopf, B. (2004) *A tutorial on support vector regression.* Statistics and computing, Vol. 14, No. 3, pp. 199-222.

Suman, S. - Das, S. K. - Mohanty, R. (2016) *Prediction of friction capacity of driven piles in clay using artificial intelligence techniques.* International Journal of Geotechnical Engineering, Vol. 10, No. 5, pp. 469-475.

Tomlinson, M., - Woodward, J. (2007) *Pile design and construction practice.* CRC Press.

Tso, G. K., & Yau, K. K. (2007) *Predicting electricity energy consumption: A comparison of regression analysis, decision tree and neural networks.* Energy, Vol. 32, No. 9, pp. 1761-1768.

Tsuha, C. D. H. C., - Aoki, N. (2010) *Relationship between installation torque and uplift capacity of deep helical piles in sand.* Canadian Geotechnical Journal, Vol. 47, No. 6, pp. 635-647.

Yao, W. J. - Chen, S. P. (2014) *ELASTIC-PLASTIC ANALYTICAL SOLUTIONS OF DEFORMATION OF UPLIFT BELLED PILE.* Tehnicki vjesnik/Technical Gazette, Vol. 21, No. 6.

Zhao, N. - Geng, H. X. - Ma, K. - Li, K. N. (2011) *Elastic-plastic analysis on damaged multi-tower isolation structure with an enlarged base.* Advanced Materials Research, Vol. 255, pp. 2550-2554.

sciendo
Slovak Journal of Civil Engineering
Vol. 30, 2022, No. 3, 27 – 32
DOI: 10.2478/sjce-2022-0018

REGULATION OF TELESCOPIC WATER INTAKE OPERATIONS

Andrey LIPIN[1*]

Abstract

Telescopic water intake structures play an important role in a water management system. The article is devoted to the improvement of telescopic water intake structures and the development of a solution for regulating their operation. Different types of water intakes are analyzed, and their shortcomings are identified. The structures of known telescopic water intakes are reviewed, and their operating principles are analyzed. It has been determined that the design of existing telescopic water intake structures lacks a device for stopping the operation of the intake of water. A structural solution for stopping and regulating the operation of a telescopic water intake is proposed. The construction of an additional ballast pontoon to be welded to the first section of the telescopic pipeline is proposed in order to regulate and stop the operation of the water intake. A methodology for calculating and designing an additional ballast pontoon for a telescopic water intake has been developed, and a specific example for its implementation has been provided. Based on the results of the research, the main parameters of the additional ballast pontoon structure have been established, and the methodology for its calculations has been developed.

Address

[1] Azerbaijan Scientific and Production Association of Hydraulic Engineering and Land Reclamation, Baku, Azerbaijan

* ***Corresponding author:*** dorian.lipin@gmail.com

Key words

- Buoyancy,
- Calculations,
- Improvement,
- Ballast pontoon,
- Operation,
- Telescopic water intake.

1 INTRODUCTION

In water management, water supply, energy and other areas of the economy, water intake structures with various designs and operating principles are used to draw water from different sources. In the vast majority, depending on the topographical, geological, and geographical conditions, frontal, side, bottom and tower intakes are used (Urishev, 2021; Progulny et al., 2020; Gabl et al., 2018; Herrmann and Bucksch, 2014; Alawadhi et al, 2018; Missimer and Watson, 2018; Budzilo, 1999; Cole et al., 1988; Bazarov and Mavlyanova, 2019; Averkiev et al., 1969; Worrall, 1978). Each type of water intake structure has specific features and disadvantages. The main disadvantages of these water intake structures are as follows:

1. When the water level in the sources fluctuates, their productivity (consumption) changes;
2. In springs filled with snow melt and spring waters, as well as water from mountain rivers, the lower horizons have lower temperatures compared to the upper ones. The water taken from these sources and supplied for irrigation has a detrimental effect on soil fertility and crop productivity. When the water temperature drops below 20^{0}C, the yield of agricultural crops in arid zones decreases by 30-40%, and when the water temperature drops below 15^{0}C, most agricultural crops die (Nxawe et al., 2009; Brockwell and Gault, 1976; Bezdnina, 1986). In addition, when the temperature of the irrigation water drops below the temperature of the soil, its biological activity deteriorates,

thereby disrupting the process of nitrification and humification;

3. When water is taken by other types of water intake structures, the purity and clarity of the water taken is not maintained. This occurs because in these structures, the water is derived from a certain depth; hence, it is suspended, and bottom sediments enter inside the water intake structures.

In the mid-20th century in Japan, surface water intakes of various designs were developed under various names (Patent No. 53-39697; Patent No. 53-43728; Patent No. 57-40294; Patent No. 57-43686; Tadao F. et al., 2001). Analyzing the principles of operational and design features, as well as identifying the shortcomings of known surface water intake structures and devices, a new telescopic water intake device was subsequently developed (Hasanov, 1991).

The telescopic water intake developed contains a float, an inlet funnel, telescopically connected pipes that taper downward, an elbow with a discharge pipe, and the connecting elements. In order to prevent cavitation, a cone-shaped air supply pipe with a protrusion directed towards the inlet funnel is installed in the middle part of the float. To ensure the automatic movement of the float downwards until the inlet funnel is closed in the case of the absence of water (or liquid) or upon reaching a dead volume of water in the source, springs are installed in the lower part of the connecting elements (Fig. 1).

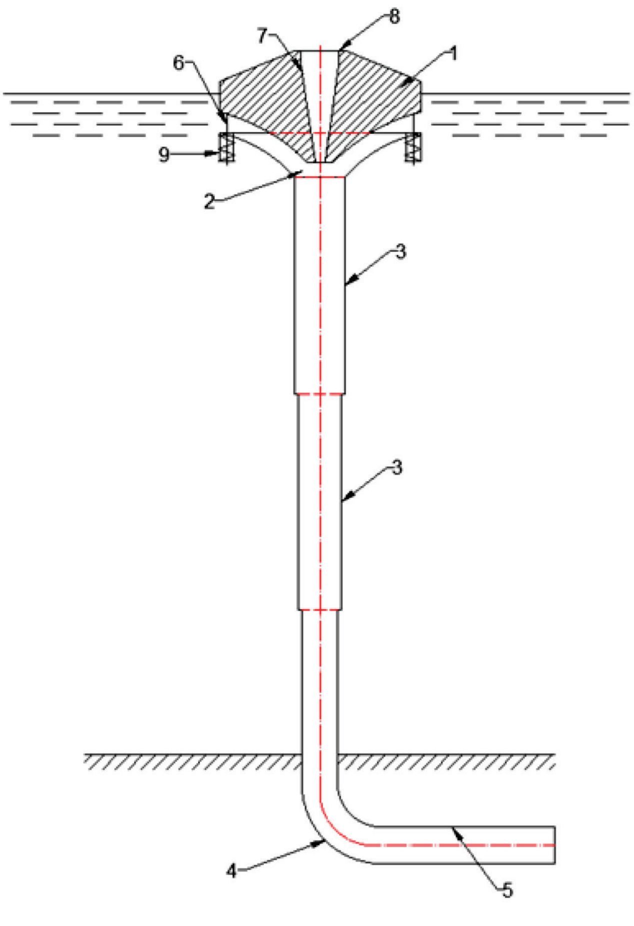

Fig. 1 *Vertical telescopic water intake: 1- flotation pontoon, 2- inlet funnel, 3- telescopically connected pipes (tapering downward), 4- elbow, 5- discharge pipe, 6- connecting elements, 7- conical air supply tube, 8- protrusions, 9- springs*

The float, which keeps the inlet funnel immersed in water, provides a constant pressure at its inlet. In this case, water from the upper layers enters the funnel. It goes from there into the telescopically connected pipes and then through the elbow into the outlet pipeline.

When the water level in the source drops, the telescopically connected pipes, funnel and float go down, and when the water level rises, they go up. As a result, an automated water intake and a constant flow rate are provided, regardless of the effective pressure in the source. The water intake is carried out from the upper horizons; it is therefore more clarified and cleaner. At the same time, it is warmer water, heated by direct sunlight, that enters the water intake.

When water enters the inlet funnel, the flow narrows and its speed increases, as a result of which a vacuum and cavitation are formed. Air is sucked into the vacuum zone through the air supply pipe, thereby preventing the process of cavitation, which is characterized by the release of vapor-gas bubbles from the flow, causing crackling, noises and vibrations, and ultimately the erosion and destruction of the device. In the absence of water or reaching a dead volume in the source, the springs installed under the connecting elements ensure the automatic closure of the inlet funnel.

The telescopic water intake device developed has a high degree of mobility and a broad field of application. At the same time, it is very simple and convenient to operate compared to other devices. Despite these advantages of the water intake, it has several disadvantages. The usual device does not provide an element for stopping the operation of the water intake.

In this regard, the purpose of the work is to improve the design of the usual telescopic water intake and to study design solutions for stopping the operation of the water intake.

2 STRUCTURAL SOLUTION

To regulate the water intake, a device for stopping its operation must be provided in the design of a vertical telescopic water intake. The most effective way to stop the water intake is to place a float on the funnel or raise the funnel to the level of the float.

In order to place the float (1) on the inlet funnel (2) (Fig. 2), positive buoyancy can be provided to the telescopic column. In this case, the water intake funnel will rise to the level of the float and be clamped to it, while a tight connection is formed between them, thus preventing water from entering into the funnel. The positive buoyancy of the telescopic column can be provided by the installation of an additional ballast pontoon.

In order to lift up the water intake's funnel, the additional ballast pontoon should be de-ballasted by means of compressed air. Water will be removed through the holes in the bottom of the pontoon, while it is filling with air. The pontoon can be supplied with air by means of an air compressor or compressed air cylinders, which can be located on top of the dam or on the shore (Fig. 3). In order to de-ballast the pontoon, a pressure of 0.6-1 MPa is required, depending on the size of the intake structure. The compressor can be connected to the ballast pontoon by means of a reinforced hose or flexible plastic tubing. There is a wide range of electric and diesel-powered air compressors with this working pressure available on the market. Cylinders with compressed air can be connected to the line through a gas reducer to reduce the pressure of the air leaving the cylinder to the required value.

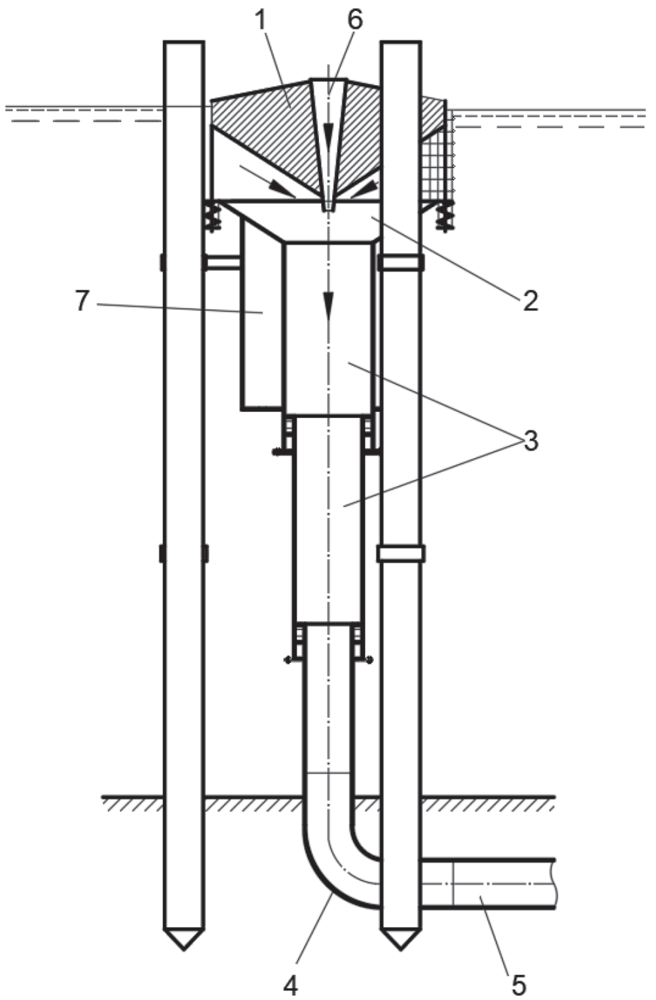

Fig. 2 *Structure of the vertical telescopic water intake equipped with an additional ballast pontoon: 1- float, 2- funnel, 3- telescopic pipeline, 4- elbow, 5- discharge pipeline, 6- diffuser, 7- additional ballast pontoon*

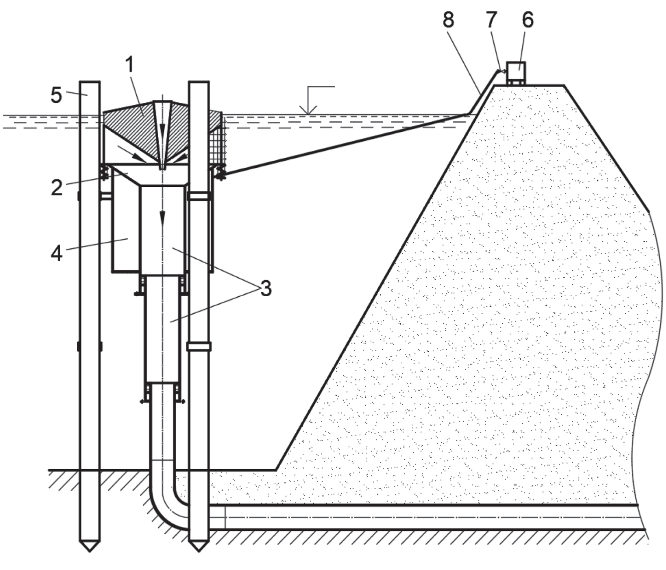

Fig. 3 *General arrangement: 1- float, 2 - funnel, 3 - telescopic pipeline, 4 - additional ballast pontoon, 5 - pile, 6 - air compressor, 7- non-return valve, 8 - air pipeline*

To resume the water supply, the water intake funnel should be lowered to the design position. By turning off the compressor and opening the non-return valve, the water will force the air out of the pontoon and it will fill with water. At the same time, the intake funnel, together with the telescopic column, will move downwards under its own weight.

This system can be controlled either manually or remotely using a radio signal. An air line should be connected to the ballast pontoon at the highest point. This arrangement will allow for the most effective removal of air from the pontoon when filling it with water.

The main advantages of this structural solution are its simplicity and reliability. The ballast pontoon has an easy-to-manufacture structure, and the use of a large-diameter pipe reduces the amount of construction and installation works. When the structure is moved up or down, the piles will act as guides, ensuring that the float is accurately clamped to the funnel.

This paper will not consider the hydraulic calculation of the telescopic water intake (Hasanov and Lipin, 2021**)**. However, it should be noted that when calculating the buoyancy of the float (1), the weight of the additional ballast pontoon should also be taken into account, in addition to the weight of the water intake funnel and telescopic pipe column.

3 ANALYTICAL CALCULATIONS OF THE ADDITIONAL BALLAST PONTOON

Calculating the additional ballast pontoon consists in defining its buoyancy, i.e., its functionality, taking into account the load imposed on it and thereby determining the height and diameter of the additional pontoon. The buoyancy of the pontoon is determined according to the theory of floating bodies, i.e., according to Archimedes' law (Shterenlikht, 2004; Ugingus and Chugaeva, 1971). According to this law, to ensure the buoyancy of the ballast pontoon, the lifting force P_b is equal to the force G, which tends to submerge it in the water:

$$\mathrm{P}_b = G - F_A, \tag{1}$$

where $F_A = g\rho_w V_{st}$ – Archimedes force, kN; g - acceleration of gravity, m/s^2; ρ_w – the density of the water, kg/m^3; V_{st} – volume of the structure, including the volume of the pontoon itself, funnel, telescopically connected pipes (suspended pipes), and other elements of the device, m^3.

The lifting force (kN) is determined by the formula:

$$\mathrm{P}_b = \gamma\omega_p h_p = \gamma W, \tag{2}$$

where $\gamma = \rho_w g$ - the volumetric weight of the water, kN/m^3; ω_p - the cross-sectional area of the pontoon, limited by the contour of the wetting, m^2; h_p – the height of the pontoon, *m*; W – the volume of water displaced by the pontoon or volumetric displacement, m^3.

The force trying to immerse the float in the water (G) includes the weight of the pontoon itself, the funnel, the telescopically connected pipes (suspended pipes) and other elements of the device. The weight of each element is determined by the following formula well known in physics:

$$G_i = g\sum\rho_i W_i = g\sum\rho_i S_i \delta_i\ ; \qquad (i=1, 2,\ldots n), \tag{3}$$

where ρ_i - density of material from which the element is made, kg / m^3; W_i - volume of material, m^3; S_i - surface area of the element, m^2; δi - thickness of the wall material, m.

Taking into account (2) and (3), equation (1) has the following form:

$$\gamma W = \sum G_i - F_A, \tag{4}$$

The buoyancy or working capacity of the pontoon and its dimensions are determined by means of equation (4).

The displacement is determined by the shape of the pontoon. In this specific case:

$$W = h_p \omega_p, \tag{5}$$

where h_p - height of the pontoon, m; $\omega_p = \pi \cdot \frac{{d_p}^2 - d_1^2}{4}$ - cross-sectional area of the pontoon, m^2; d_p - diameter of the pontoon, m; d_1 - diameter of the first pipe section, m.

If the load acting on the pontoon is defined, the displacement is determined by equation (4):

$$W = \frac{\sum G_i - F_A}{\gamma}. \tag{6}$$

With the known value of the displacement W and the diameter of the pontoon d_p, the height of the cylindrical pontoon is determined by equation (5):

$$h_p = \frac{W}{\omega_p}. \tag{7}$$

It should be noted that calculating the ballast pontoon is carried out by the approximation method, since the dimensions and, consequently, the weight of the pontoon, are not known. Therefore, in the first approximation, the height of the pontoon (h_p) is accepted, and then its weight is calculated. If, in the process of the calculations, the accepted height of the pontoon turns out to be less or significantly more than the calculated one, then in this case its value should be increased or decreased, and the calculations have to be performed again.

Calculating the pontoon can be carried out in another way; for example, by taking (accepting) the height of the pontoon, you can determine its diameter:

$$\gamma h_p \pi \cdot \frac{{d_p}^2 - d_1^2}{4} \geq \sum G_i - F_A. \tag{8}$$

where all the symbols are the same.

When the intake of the water is stopped, the water will go out of the structure, and the structure will be filled with air. In this case the telescopic column, together with the funnel, will acquire positive buoyancy. In order to start the water intake operation again, we should check the following equation:

$$G - F_A > P_{st}. \tag{9}$$

where - buoyancy of the telescopic column and funnel in the top position.

The buoyancy force trying to keep the structure afloat includes the buoyancy of the funnel and telescopically connected pipes.

$$P_{st} = \gamma \sum W_{st\,i}. \tag{10}$$

where - volumetric displacement of the element

4 RESULTS OF THE ANALYTICAL CALCULATIONS

4.1 Example

Calculate the additional pontoon with the following initial data of the telescopic water intake (Fig. 4):

Inlet funnel diameter: $D = 1.55$ m;
Diameter of the first section: $d_1 = d_{outlet} = 0.75$ m;
Diameter of the second section: $d_2 = 0.72$ m;
Diameter of the third section: $d_3 = 0.69$ m;
Funnel height: $h_f = D = 1.55$ m;
Length of the telescopic pipes: $l_1 = l_2 = l_3 = 5$ m;
Thickness of the steel cylindrical wall of the ballast pontoon, steel pipes and funnel: $\delta = 24$ mm;
Thickness of the wall of the steel top and bottom plates of the ballast pontoon: $\delta_{end} = 64$ mm.

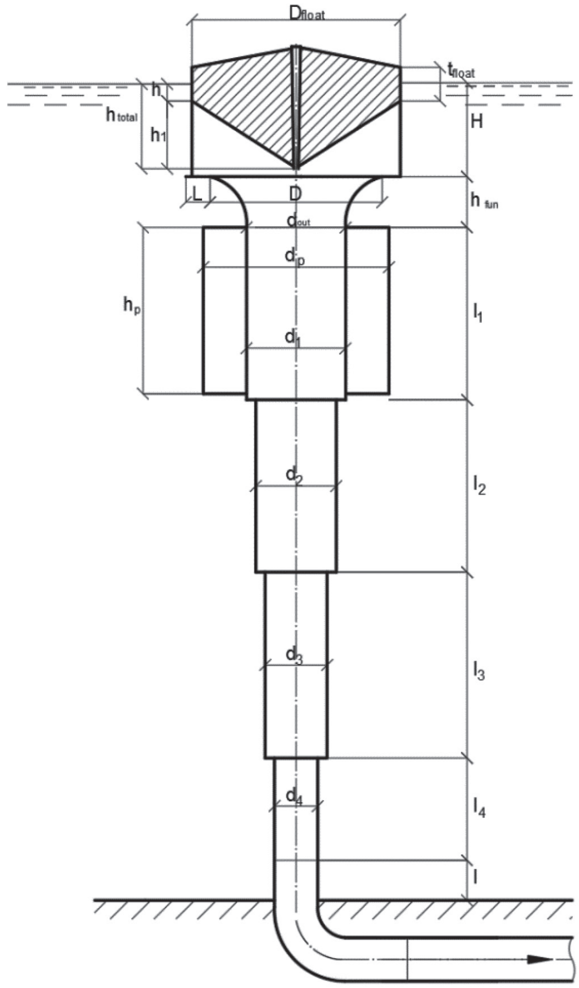

Fig. 4. *Scheme for calculating the additional ballast pontoon*

For calculating the weight of the additional pontoon, we set its diameter at $d_p = 2$ m. and its height at $h_p = 5$ m. According to the thickness of the sheet wall δ and the density of the steel ($\rho_s = 7850$ kg / m^3), using the formula (3), we find its weight:

$A_{p.\ wall} = 3.14 \cdot 2 \cdot 5 = 31.4$ m^2 - surface area of the additional pontoon's cylindrical wall;

$A_{end} = 2\left(3.14 \frac{2^2 - 0.75^2}{4}\right) = 5.4$ m^2 m^2 -surface area of the additional pontoon's top and bottom plates;

$$G_\text{p} = 9.81 \cdot 7850 \cdot (31.4 \cdot 0.024 + 5.4 \cdot 0.064) = 84.98 \text{ kN}.$$

In the same way, we can determine the weight of the pipes and funnel G_{pipe}=42,58, G_{fun}=21,29 kN.

$$\sum G = G_\text{p} + G_{fun} + G_{pipe} = 84.98 + 21.29 + 42.58 = 148.85 \text{ kN}.$$

According to equation (1), we have to consider the impact of the Archimedes force on the immersing force:

$$F_A=9.81\cdot 1000\cdot 1.93=18.9 \text{ kN}$$

Using equation (4), we find the displacement of the ballast pontoon with the volumetric weight of the water $\gamma = 10$ kN/m^3:

$$W = \frac{148.85-18.9}{10} = 13 \text{ m}^3$$

From formula (7), we can determine the height of the cylindrical pontoon.

$$h = \frac{13}{2.7} = 4.82 \text{ m.} \approx 5 \text{ m.}$$

By means of equation (8), we can check the buoyancy of the ballast pontoon:

$$10\cdot 5\cdot 3.14\cdot \frac{2^2-0.75^2}{4} \geq 129.85 \text{ kN.}$$

$$135\geq 129.85$$

Equation (8) complies with the accepted and determined values; therefore, calculating the ballast pontoon ends.

By means of equation (10) we can calculate the buoyancy of the telescopically connected pipes and funnel after they are filled with air: W_{1st}=2.21 m^3; W_{2nd}=2.04 m^3; W_{3st}=1.87 m^3; W_{fn}=6.69 m^3:

$$10\cdot(2.21+2.04+1.87+6.69) = 128.1 \text{ kN}$$

By means of equation (9), we can check the funnel's opening condition to start the water intake:

$$129.85 > 128.1 \text{ kN}$$

Equation (9) complies with the accepted and determined values; therefore, the calculations end.

5 CONCLUSION

In this work, the structural solution for the regulation and end of the operation of a telescopic water intake was analyzed. The main conclusions are as follows:

1. The principle of the operation of the telescopic water intake was analyzed.
2. The design of an additional ballast pontoon has been proposed, and the principles of its operation are described.
3. The methodology for calculating a ballast pontoon has been developed, and the main parameters of the pontoon have been determined.

REFERENCES

Alawadhi A. - Sajwani Z. - Salman F. - Kayani F. - Alteneiji S. - Alras Z. (2018) *Water intake among Sharjah*. International Journal of Recent Scientific Research Vol. 9, N$_o$. 10(D), pp. 29331-29334. DOI: 10.24327/ijrsr.2018.0910.2840

Averkiev A.G. - Makarov I.I. - Sinotin, V.I. (1969) *Damless water intake structures*. Energiya, 164 pp. [in Russian].

Bazarov D.R. - Mavlyanova D.A. (2019) *Numerical studies of long-wave processes in the reaches of hydrosystems and reservoirs*. Magazine of Civil Engineering. 87(3). pp. 123-135. DOI:10.18720/MCE.87.10.

Bezdnina S. Ya. (1986) *Optimal parameters of soil reclamation regime*. Hydrotechnics and melioration. No. 11; pp. 58-63 [in Russian].

Brockwell J. - Gault R. R. (1976) *Effects of irrigation water temperature on growth of some legume species in glasshouses*, Australian Journal of Experimental Agriculture 16(81). pp. 500-505. DOI: 10.1071/EA9760500

Budzilo B. (1999) *Reliability subsystem of surface water intakes*. Water Engineering and Management 146(7). pp.18-21.

Cole J. A. - Hawker P. J. - Lawson J. D. - Montgomery H. A. C. (1988) *Pollution Risks and Countermeasures for Surface Water Intakes*. Water and Environment Journal 2(6). pp. 603-625. DOI: 10.1111/j.1747-6593.1988.tb01349.x

Gabl R. - Gems B. - Birkner F. - Hofer B. - Aufleger M. (2018) *Adaptation of an Existing Intake Structure Caused by Increased Sediment Level*. Water, 10, pp. 1066. doi:10.3390/w10081066

Hasanov S.T. (1991) *Water intake device*. USSR patent by Application No. 4883468/15 (111716), M. Kl5E02 B5 / 08.

Hasanov S. - Lipin A. (2021) *Modernization and increasing of stability of telescopic water intake*. Hydraulic Engineering Journal ISSN 0016-9714. No. 4, pp. 58-63 [in Russian].

Herrmann H. - Bucksch H. (2014) *Water intake*. Dictionary of Geotechnical Engineering/Wörterbuch GeoTechnik. Springer, Berlin, Heidelberg. https://doi.org/10.1007/978-3-642-41714-6_230502

Japanese application Patent No. 53-39697, M.cl. EO2 B 9/04, 1978.

Japanese application Patent No. 53-43728, M.cl. EO2 B 9/04, EO2 B 13/00, 1978.

Japanese application Patent No. 57-40294, M.cl. EO2 B 7/032, 5/08, 1983.

Japanese application Patent No. 57-43686, M.cl. EO2 B 7/32, 1986.

Missimer T. M. - Watson I. C. (2018) *Conventional Surface Water Intake Designs*. Water Supply Development for Membrane Water Treatment Facilities. pp. 47-55. DOI: 10.1201/9781351077637-7

Nxawe S. - Laubscher C. - Ndakidemi P. (2009) *Effect of regulated irrigation water temperature on hydroponics production of spinach (Spinacia oleracea L)*, African Journal of Agricultural Research Vol. 4 (12), pp. 1442-1446.

Progulny V. - Hurinchyk N. - Grachov I. - Borysenko K. (2020) *Porous constructions of water intake structures*. Bulletin of Odessa State Academy of Civil Engineering and Architecture, No. 81, pp. 149-155. DOI: 10.31650/2415-377X-2020-81-149-155

Shterenlikht D.V. (2004) *Hydraulics*, 3rd ed., Moscow. Kolos. p. 656 [in Russian].

Tadao Fukushima. - Junsheng Gao. - Masayuki Fujihara (2001) *Selective Intake from Middle-High Water Flow in a Small River*. Design Concept of Settling Basin and Surface Water Intake. Journal of Rainwater Catchment Systems 6(2). pp. 39-42. DOI: 10.7132/jrcsa. KJ00003257877

Ugingus A. A. - Chugaeva E. A. (1971) *Hydraulics*. Leningrad: Stroyizdat. p. 350 [in Russian].

Urishev A. (2021) *Current use of water intake structures of reservoirs*. IOP Conference Series Materials Science and Engineering 1030:012119. DOI: 10.1088/1757-899X/1030/1/012119

Worrall R.J. (1978) *The Effect of Irrigation Water Temperature on the Germination and Growth of Plants*, Acta Horticulturae. pp. 145-152. DOI: 10.17660/ActaHortic.1978.79.16

sciendo
Slovak Journal of Civil Engineering
Vol. 30, 2022, No. 3, 33 – 42
DOI: 10.2478/sjce-2022-0019

FEASIBILITY OF USING ENERGY PERFORMANCE CONTRACTING FOR THE RETROFIT OF APARTMENT BUILDINGS IN SLOVAKIA

Veronika GOMBOŠOVÁ[1], Michal KRAJČÍK[1*], Ondřej ŠIKULA[2]

Abstract

This study is focused on the feasibility of using energy performance contracting (EPC) for the retrofit of two apartment buildings constructed using precast concrete technologies in Slovakia decades ago. The retrofit packages were defined, and their suitability for EPC was evaluated through discounted payback. The uncertainties in the profitability calculations were covered by designing five possible economic developments and defining input ranges instead of just single inputs. The measures in the technical systems were shown to be more feasible than the retrofit of the building envelopes. The potential to finance the selected measures for technical systems through EPC was further evaluated. It was shown that, for at least one of the two buildings studied, the EPC was recommended only for the economic developments with a notable increase in energy prices compared to the baseline that referred to the situation before the Covid-19 pandemic. In the best case, the payback was four years for one building and seven years for the other; thus, both were potentially suitable for EPC. However, for a complex retrofit, the EPC must be combined with a different funding source to also finance other retrofit measures.

Address

[1] Faculty of Civil Engineering, Slovak University of Technology, Bratislava, Slovak Republic
[2] Faculty of Civil Engineering, Brno University of Technology, Brno, Czech Republic

* ***Corresponding author:*** michal.krajcik@stuba.sk

Key words

- Apartment building,
- Energy performance contracting (EPC),
- Profitability,
- Building retrofit.

1 INTRODUCTION

The reduction of fossil fuel consumption is one of the most urgent challenges worldwide due to the need to mitigate impending climatic changes. Furthermore, for many countries, phasing out fossil fuels is vital for decreasing their dependence on the import of energy carriers. This triggers various incentives for the reduction of energy consumption and the decarbonisation of economies. For example, just recently, the European Commission adopted a set of proposals to make the European Union's (EU) climate, energy, transport, and tax policies capable of reducing net greenhouse gas emissions by at least 55% by 2030, compared to 1990 levels (European Commission, 2022 a). Retrofitting old buildings is an important means of reducing energy consumption and decarbonising building stock (Życzyńska et al., 2020; Vargová and Ingeli, 2021; Cholewa et al., 2022). One of the potentially feasible methods to fund and execute a retrofit is the use of energy performance contracting (EPC), which is an energy service with guaranteed energy savings provided under a contract concluded between an energy service provider and a recipient of the energy service (Act No. 321/2014 Coll.).

The EPC is provided by an energy service company (ESCO). Funding a retrofit project through EPC means that if the project does not provide returns on the investment, the ESCO is responsible for paying the difference, thus assuring their clients of any energy and cost savings. Therefore, ESCOs accept some degree of risk to achieve improved energy efficiency in a user facility and receive their payments based on the achievement of those energy efficiency improvements (European Commission, 2022 b). The risk-free nature of the service provided by ESCOs offers a convincing incentive for their clients to invest. The result is a verifiable, measurable, or estimable energy savings that improves energy efficiency and allows for a financial or material advantage for all parties involved due to more energy-efficient technology or activity (Act No. 321/2014 Coll.). Another important advantage of the EPC is the significant potential to retrofit public buildings without the need for public funds.

Apartment buildings are an essential component of the building sector. In Slovakia, most apartment buildings were built several decades ago in an era of massive prefabrication. Most of these buildings have only been partially renovated or are almost entirely in their original condition. The majority of the apartment buildings, where a large part of the population in Slovakia lives, are in private ownership (European Commission, 2017; MDV SR, 2020). In addition, apartment buildings can also be owned by governmental bodies and municipalities and used, for example, as social housing, care centres for the elderly, and dormitories. Due to the risk-free nature of EPC and the lack of a need of funding, EPC could be a feasible method to retrofit these apartment buildings. The advantage is that an ESCO could guarantee energy savings without the need for the building owner to look for funding. Apartment buildings owned by the government and municipalities could especially be retrofitted without the need for public funds.

Currently, there are several potential barriers to the use of EPC for building retrofits, which do not apply only to apartment buildings. First, research on the use of EPC for retrofitting is scarce, while studies on the use of EPC for retrofitting apartment buildings are entirely lacking. Research on the use of EPC for building retrofits includes Bizzarri and Morini (2006), who focused on the environmental benefits achievable in hospitals in Ferrara, Italy, through a shift from conventional systems to various hybrid plants. The high costs of the energy sources there represented an insurmountable market barrier. More recently, Principi et al. (2016) presented an analysis of the suitability of EPC for three acute care hospitals and two community clinics in Italy. The best renovation activities included improving the control and regulation of existing subsystems without the replacement or with the partial replacement of subsystems and the integration of renewables. For such low-cost actions, the savings were at least 35 to 40%, and payback was 9 to 11 years, which could be potentially suitable for EPC.

Furthermore, as concluded by Labanca et al. (2015) and based on a literature search and questionnaire survey, "*despite the substantial economic energy saving potential in the building sector of the European Union (EU), the energy efficiency service market is not correspondingly developed. Especially in the residential sector, the energy service market is much less developed in this market segment than in other demand sectors such as, for example, the industry or the public/service sector*". The use of EPC for retrofitting buildings is also hampered by the fact that a complex renovation increases investment costs. For a complex retrofit, the retrofit packages should also include unprofitable measures that are not suitable for financing through EPC. In addition, a significant risk for ESCOs using EPC is an erroneous estimate of the energy-saving potential and profitability of the project. This may lead to economic losses for an ESCO, which has to balance any discrepancies between the contract and the real energy savings. Therefore, it is critical to accurately estimate the energy savings and financial developments.

Various studies have been aimed at estimating the energy savings potential of apartment buildings and the profitability of their retrofit (e.g., Kuusk et al., 2014; Kuusk and Kalamees, 2015; Patiño-Cambeiro et al., 2016). However, as Giretti et al. (2018) stated, "*gathering comprehensive and reliable technical information is a time-consuming and expensive process that must be carried out within the submission deadline. In these conditions, the standard approach to energy performance forecasting which uses detailed simulation is practically unfeasible*." This is one of the reasons why energy simulations are not widely used for energy audits of building in practice; on the other hand, professionals tend to use simpler calculation tools such as commercial software or custom Excel spreadsheets. This also can lead to erroneous estimations due to, for example, the lack of precision and lack of capability to fully take into account some components of the energy balance. These factors prevent reliable estimations of the energy-saving potential and profitability of retrofitting. For these reasons, part of these investigations aims to develop simplified procedures to reliably estimate savings and reduce the uncertainty of the calculations (Faggianelli et al., 2017; Giretti et al., 2018; Lee et al., 2018; Ramos et al., 2019). An alternative approach is to generate many predefined combinations of energy efficiency measures in various climates that can be used to select suitable retrofit scenarios (Gustafsson et al., 2017; Dipasquale et al., 2019).

Based on the above discussion, several conclusions can be drawn: research on the use of EPC for the retrofit of apartment buildings is scarce, and suitable combinations of retrofit measures for financing through EPC must be determined; to this end, reliable and affordable methods to estimate the calculations precisely are needed. EPC often needs to be combined with other sources of financing for the retrofit to be successful, while also being profitable for the ESCO. This study focuses on the possibilities of using EPC for typical old apartment buildings in Slovakia. Potentially feasible retrofit packages were defined, and their suitability for EPC was evaluated through discounted payback (PB). The uncertainties in the energy and economic calculations were covered by devising several possible scenarios of economic development and defining input ranges instead of just single inputs. The present study contributes the very limited body of research on the use of EPC for the retrofit of apartment buildings. It defines retrofit measures that are potentially suitable for apartment buildings and shows the feasibility of financing the retrofit measures through EPC under several possible economic developments. Although this study refers to apartment buildings in Slovakia, the results can also be applied internationally, especially in countries with a similar climate and building construction technologies.

2 MATERIALS AND METHODS

2.1 Description of the buildings

Two apartment buildings are presented here as representatives of the old building stock. The buildings were constructed using precast concrete technologies in the 1980s. In this sense, the two buildings are similar to many other apartment buildings built with precast concrete technologies several decades ago that currently represent a substantial part of the housing stock in Slovakia. The schematic geometry of the apartment buildings is shown in Fig. 1. Both buildings are located in Bratislava, Slovakia.

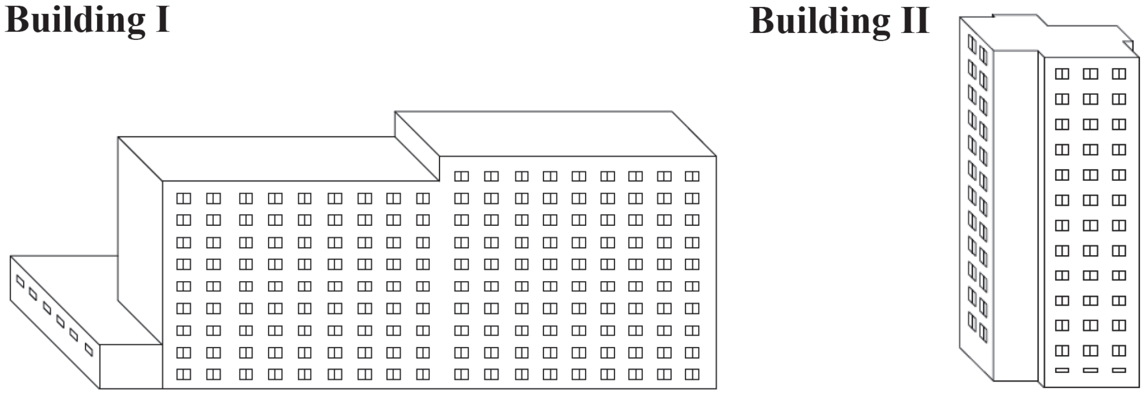

Fig. 1 *Geometry of the apartment buildings (not to scale)*

2.1.1 Building I

Building I is a 10-story apartment building with an outbuilding located on the left side of the building. The floor plan of the building is a simple rectangle with external dimensions of 13.5 x 88 m and each floor has an average construction height of 2.8 m. The heated volume is 32,992 m^3. The peripheral walls mainly consist of 300 mm-thick walls made of reinforced concrete panels with thermal insulation in between them. Some of the walls consists of bricks made of aerated concrete (300 m). The walls of the outbuilding are made of reinforced concrete (300 mm) insulated with expanded polystyrene (120 mm). The original roof structure is flat and made of reinforced concrete and perlite concrete. It is insulated with 70 mm-thick expanded polystyrene and has waterproofing made of asphalt strips. The original insulation is in poor condition. The roof of the outbuilding is made of reinforced concrete, perlite concrete, 200 mm-thick expanded polystyrene, and waterproofing. The opening structures were previously renovated and are made of triple glazing with an insulated plastic frame. The heat emission elements are plate radiators and fitted with thermostatic heads. The space heating and DHW distribution pipes are in their original condition and partially insulated with original insulation. The heat for the space heating and domestic hot water (DHW) is supplied from a district system, which is connected to a heat exchange station located outside of the building. The heat consumption is measured at the entrance to the building. The thermal gradient is 90/70°C. The lighting system has undergone a partial renovation. The building is equipped with linear fluorescent lamps with a classic ballast, LED lamps, or lamps with a classical incandescent bulb.

2.1.2 Building II

Building II has a pointed shape and thirteen above-ground storeys. The floor plan is irregular in shape, and the construction height of each storey is 2.8 m. The heated volume is 13,649 m^3. There is a gas boiler room, auxiliary rooms, and storage areas on the first floor. On the second storey, there is the main entrance to the building, a gatehouse, living quarters, rented premises, a cleaning room, and auxiliary and storage spaces. The third storey contains apartments, offices, and auxiliary premises. There are apartments on the fourth to the thirteenth stories. The peripheral walls are 290 mm-thick sandwich panels made of reinforced concrete panels with thermal insulation in between them. The roof is flat and uninsulated. The opening structures are mostly made of double glazing and a plastic frame. The radiators are cast iron with steel plates and thermostatic heads for individual control. The pipes for the space heating and DHW systems are newly insulated in the boiler room but are in their original condition otherwise. The heat source is a gas boiler room located on the first storey, with seven gas condensing boilers with a total heat output of 400 kW and an expected efficiency of 86%. The thermal gradient is 90/70°C. The DHW is centrally prepared using two storage heaters with a volume of 750 litres each. The lighting system has undergone a partial renovation. It consists of luminaires with linear fluorescent lamps and classic and electronic ballasts, LED bulbs, or old luminaires with classical incandescent bulbs, and one halogen light.

2.2 Calculation methodology

The calculation procedures regarding the energy needs for the heating, thermal losses and auxiliary energy for the heating system, the auxiliary energy, and losses for the DHW system, the energy balance of the solar thermal system, and the entire economic calculation procedure were custom programmed in MS Excel.

2.2.1 Energy calculations

The energy calculations for the space heating system follow the latest European standards. These included the energy need for heating (EN ISO 52016-1), heat losses from emission (EN 15316-2), distribution (EN 15316-3), storage (EN 15316-5) and generation systems, including electricity for circulating pumps (EN 15316-3). The calculations of the DHW system involved thermal losses of the distribution system, including electricity for circulating pumps (EN 15316-3), storage losses (EN 15316-5), and generation losses. The energy balance of the solar thermal system was calculated as defined in EN 15316-4-3. The EN standards provide calculation procedures with a seasonal, monthly, and hourly calculation step. In the present work, the monthly calculation step was used compared with the seasonal step, which was considered too inexact for the purpose. The calculation procedure was programmed into a customized MS Excel tool that was easy to modify and suited for practical calculations. In addition, it permitted calculations of emission, distribution, storage, and generation losses from space heating and DHW systems.

The values calculated were compared with the invoiced data measured. Furthermore, to obtain realistic results, data on the physical condition of the buildings were carefully collected through a study of the project documentation, detailed inspection of the buildings, and interviews with the caretakers responsible for the buildings and their energy systems. The invoiced data was used to adjust the calculation inputs. However, the invoiced data provided information on the total energy consumption. This overall value was divided between space heating and DHW. First, the energy budget for the space heating system was determined, and the rest was attributed to the DHW, making sure that the values were realistic. After determining the energy needs and losses, the energy delivered was divided among the energy carriers. In the end, the calculated and measured values were 1355 MWh versus 1322 MWh for Building I and 905 MWh versus 934 MWh for Building II.

The energy balance of the photovoltaic system was calculated using a verified online calculation tool (European Commission, 2022 c). The modernization of the lighting system was based on an evaluation of the individual types of luminaires and their current state and wattage. As the electricity consumption for the lighting was not measured separately, it was necessary to approximate it according to the number of hours of lighting, which was determined based on the operating characteristics for this type of building. Electricity consumption was determined for each luminaire separately as the product of the total number of hours of lighting per year and the total wattage of the given type of luminaire. This consumption was further increased by 15% for obsolete lamps with a classic magnetic ballast. This value is routinely used by energy auditors in practice.

2.2.2 Economic calculations

Net present value (NPV) is the present value of future cash flows generated by a retrofit measure or a project; it also includes the initial investment. Using the terminology and notation defined in EN 15459-1, it can be expressed as follows:

$$NPV = \sum_{t=1}^{n} CF_t \cdot \left(\frac{1}{1+RAT_{\mathrm{disc}}}\right)^t - CO_{INIT} + CO_{INIT,ref} \quad (€)\ (1)$$

where CF_t is the difference in cash flows between the optional case and the reference case in year *t*; *n* is the lifetime or calculation period; RAT_{disc} is the discount rate; CO_{INIT} are the initial investment costs; and $CO_{\mathrm{INIT,ref}}$ are the initial investment costs for the reference case (0 is for the option of doing nothing).

For an ESCO that guarantees the value of energy savings for a certain period, knowing the payback is critical. Therefore, the discounted payback (PB) is an important profitability indicator for an ESCO that needs to be sure that the investment will pay for itself before the contract is terminated. PB is the time when the NPV equals zero. It is calculated as follows (EN 15459-1):

$$PB = \sum_{t=1}^{TPB} CF_t \cdot \left(\frac{1}{1+RAT_{\mathrm{disc}}}\right)^t - CO_{INIT} + CO_{INITref} = 0 \quad (a)\ (2)$$

where *TPB* is the last year for the payback period (the time when the sum is stopped because the formula becomes negative or equal to 0).

The discounted payback was used to evaluate the suitability of retrofit measures for EPC in the present study. The reason was that in EPC projects, it is crucial to assure that the investment in the retrofit measures returns before a certain interval, typically 10 to 15 years. For this reason, from the point of view of suitability for EPC, the discounted payback is considered to be the single most important indicator.

When calculating the investment in an EPC energy efficiency measure, it is necessary to consider the additional costs of financing through EPC by increasing the investment in the measure. The existing legislative framework requires that additional costs related to risk, management, insurance, or repairs be reflected in the investment costs. These additional costs were expressed as a percentage of the initial investment per measure as follows: EPC project financing 20%, EPC project management 2%, repair costs for building structures 1%, repair costs for technical systems 2%, and insurance 1%.

Tab. 1 *Retrofit measures and subpackages considered*

System	Retrofit measure	Subpackage
Building structures	Replacement of opening structures	*EEM0*
	Insulation of perimeter walls	
	Insulation of roof	
	Insulation of floor above basement	
	Insulation of attic floor	
Space heating	Replacement of heat source	*EEM1*
	Insulation of piping	
	Hydraulic regulation and temperature control	
	Adjustment of temperature gradient (supply/return)	
	Renovation of measurement and control system	
Domestic hot water (DHW)	Insulation of piping	*EEM2*
	Replacement of circulating pump	
Indoor lighting	Renovation of lighting system	*EEM3*
Renewable energy sources (RES)	Solar thermal system	*EEM4*
	Photovoltaics	*EEM5*
Energy management	Energy management system (EMS)	*EEM6*

2.3 Retrofit measures considered

The retrofit measures are divided into two categories, i.e., measures for building structures and measures for technical equipment. Table 1 shows the combinations of retrofit measures considered. At the beginning, several retrofit measures were selected to allow for the creation of various combinations of measures (packages). This set of measures was created based on the scanning of the buildings and the experience from previous energy audits. The retrofit measures were divided into subpackages, because some of the measures were implemented meaningfully or typically together. Another reason is that, in some cases, it may be difficult to determine the energy savings of an individual measure, and it makes sense to determine the savings together for a group of measures. Two combinations of retrofit measures were created. Combination 1 only included the retrofit of the building envelope. These measures are part of the EEM0 subpackage (Table 1). An energy management system (EMS) was also included because it is mandatory in EPC projects (EEM6). Combination 2 involved retrofit measures on technical equipment (subpackages EEM1 to EEM6). Combinations of measures were selected so as to achieve paybacks that indicate the suitability of the project for EPC.

3 RESULTS

The formulation of the results included two phases. First, retrofit measures that could potentially be suitable for financing through EPC were selected. Subsequently, the suitability of the chosen retrofit package for financing through EPC under various possible economic developments was discussed, based on the detailed energy and economic calculations.

3.1 Selection of retrofit measures

One of the retrofit packages contained measures regarding the insulation of the building envelope, whereas the other focused on the retrofit of the technical systems. The measures on the envelope and technical systems were treated separately because they tend to have very different initial investments and profitability.

3.1.1 Retrofit package 1

The retrofit measures regarding the building structures were primarily aimed at the reduction of heat transmission losses. For each structure, the proposed level of thermal insulation was based on the requirements defined in the national standard STN 73 0540-2+Z1+Z2 (Table 2). The corresponding EEM0 subpackage included measures such as insulation of the roof structure, insulation of the walls, and replacement of the opening structures. The measures were selected separately for each building according to its renovation needs. For Building I, Combination 1 included insulation of the perimeter walls, replacement of the opening structures, and the installation of EMS. For Building II, the measures included insulation of the perimeter walls, insulation of the roof, and the installation of EMS. For both buildings, the payback calculations showed the measures on the building envelope to be relatively unfeasible and thus not suitable for EPC. These results referred to the use of mineral wool as thermal insulation.

Tab. 2 *Requirements for the thermal insulation of building structures of retrofitted buildings as defined in STN 73 0540-2+Z1+Z2*

Building structure	Indicator	Requirement
External wall and slope roof above inhabited space (slope > 45°)	U, W/(m^2.K)	0.22
Flat or slope roof (slope ≤ 45°)	U, W/(m^2.K)	0.15
Ceiling above outdoor environment	U, W/(m^2.K)	0.15
Ceiling beneath unheated space	U, W/(m^2.K)	0.20
Windows, doors in external wall	U, W/(m^2.K)	0.85
Floor above unheated space (Difference in air temperature between spaces of up to 15 K)	U, W/(m^2.K)	0.60
Floor of heated space on the ground	R, (m^2.K)/W	2.50

Explanation: U – heat transfer coefficient, R – thermal resistance

3.1.2 Retrofit package 2

The assessment of the suitability of the measures was based on the terms of the EPC signed between the provider and the beneficiary. In our case they were ESCO and the owner of the buildings in question. It was assumed that the contract could be signed for a maximum duration of 15 years, which is typical of EPC projects. For this reason, appropriate measures were selected so that the payback of the combination did not exceed a payback period of 15 years. The retrofit sub-packages proposed for each building are summarized in Table 3. The measures considered for the EPC are marked by a cross. An overview of the calculation inputs and outputs is shown in Table 4. The costs of the heat and electricity used in the calculations were based on invoices. The difference in the cost of the heat between Building I and Building II was caused by different heat sources, that is, the district heating plant versus the boiler room located in the building.

Tab. 3 *Proposed retrofit measures on the technical systems*

	EEM1	EEM2	EEM3	EEM4	EEM5	EEM6
Building I	x	x	x		x	x
Building II	x	x	x	x		x

Tab. 4 *Inputs and profitability indicators for Buildings I and II – retrofit package 2*

	Building I	Building II
Discount rate (RAT_{disc})	1%	1%
Investment (€)	249,906	115,981
Investment with EPC (€)	299,887	139,178
Inflation rate (%)	3%	3%
Price of heat (€/kWh)	0.1500	0.0450
Price of electricity (€/kWh)	0.1496	0.1496
Energy saving – heat (MWh/a)	183.6	38.3
Energy saving – electricity (MWh/a)	136.9	82.2
Financial saving (€/a)	43,828	14,019
Discounted payback (a)	6.8	14.4

3.2 Suitability for EPC under various economic developments

Here, we evaluate in detail the suitability of the retrofit measures selected in the previous section (retrofit package 2) for EPC. The effect of the input parameters on profitability is also discussed. The economic calculations are performed for several possible economic developments. The EPC project is based on the Energy Saving Performance Contract, which defines the basic terms, the subject of the contract, the obligations of the provider and the client, payments for the EPC, the financing and insurance of the project, sanctions, and the termination of the contract. The duration of the contract should be at least eight years, and it is defined in the contract. A typical duration is 10 years, but contracts for up to 15 years are not uncommon. One of the most important criteria for the suitability of retrofit measures for EPC is the payback of the EPC project compared to the duration of the contract. The payback must be lower than the duration of the contract, even when uncertainties are taken into account.

3.2.1 Definition of possible economic developments

Unfortunately, it is not possible to precisely characterize the current situation because it is constantly changing. For example, most of the calculation inputs were prepared and the calculations performed during a relatively stable economic situation. Recently, the economic situation has become turbulent. The cost of building materials has been increasing, as has the energy costs. It is not clear how the situation will develop in the future. In addition, there is always uncertainty in energy savings due to simplification of the calculation models and input data. The uncertainty in inputs includes the insulation level of building structures, the geometry, the internal and solar heat gains, the indoor temperature and air change rate, etc. To cover this uncertainty at least partially, five economic developments have been devised to cover the range of possible developments of investment and energy costs (Table 5). However, the rate of increase is not the same for the investments and energy. Investments tend to rise at a lower rate relative to the baseline, whereas energy prices can double or even triple. The economic developments are briefly described as follows:

- **INV -10%, EP -10%** – Favourable development of the economy i.e., materials are abundant and cheaper compared to the baseline. In addition, energy costs are relatively favourable for consumers. Investments (INV) and energy prices (EP) are 10% lower than the baseline. This development is unlikely to occur but is included for purposes of comparison.
- **Baseline (INV 0%, EP 0%)** – This is a basic scenario that assumes a realistic input based on the searches and documents available in the input preparation phase. It reflects the situation just before the Covid-19 pandemics before costs began to increase sharply. It serves as a reference.
- **INV +30%, EP +50%** – Investments (INV) are 30% higher and the energy prices (EP) are 50% higher than the baseline. In the current situation, this development is more realistic than the baseline.
- **INV +50%, EP +100%** – It represents unfavourable economic developments. It assumes that the investments (INV) are 50% higher and energy prices (EP) are 100% higher than the baseline.
- **INV +100%, EP +150%** – Least favourable of all the economic developments. It assumes that investments (INV) will double and that energy costs (EP) will increase by as much as 150%.

For each economic development, the middle, upper, and lower values were calculated. The middle values represent the estimated parameters that were input. The upper and lower values represent the estimated ranges of the parameters that were input to assess the uncertainty of the calculations. The ranges of the parameters input were chosen so as to be realistic, i.e., not too narrow to account for the errors in the calculation, but not too wide so that the calculated payback is specific enough to allow drawing conclusions. The values that were input represented the initial calculation values. The average inflation in the energy costs during the calculation period was assumed to be 3%. The discount rate (RAT_{disc}) was selected as 3%. The zero discount was also considered to represent a situation with a stronger intent to retrofit without considering the discounting of the money. The uncertainty in the investment was ±10%; the uncertainty in the energy costs was ±20%; and the uncertainty in the energy savings was also ±20%. The upper and lower limits were obtained by combining the parameters that were input in the most unfavourable way possible to determine the maximum overestimation and underestimation of the payback.

Tab. 5 *Definition of the economic developments*

Economic development	Value	Change in inputs relative to the reference (Baseline - middle)		
		Investment	Energy costs	Energy savings
1 INV -10%, EP -10%	lower	-20%	10%	20%
	middle	-10%	-10%	0%
	upper	0%	-30%	-20%
2 **Baseline** (INV 0%, EP 0%)	lower	-10%	20%	20%
	middle	**0%**	**0%**	**0%**
	upper	10%	-20%	-20%
3 INV +30%, EP +50%	lower	20%	70%	20%
	middle	30%	50%	0%
	upper	40%	30%	-20%
4 INV +50%, EP +100%	lower	40%	120%	20%
	middle	50%	100%	0%
	upper	60%	80%	-20%
5 INV +100%, EP +150%	lower	90%	170%	20%
	middle	100%	150%	0%
	upper	110%	130%	-20%

Explanation: INV – investment, EP – energy costs

3.2.2 Suitability for EPC – Building I

The values that were input and results for Building I are shown in Table 6 and visualized in Fig. 2. In general, the payback is favourable for the EPC. This was because only profitable retrofit measures on technical systems were selected for the EPC project and the systems were mostly in the original condition. For a complex retrofit, the EPC would probably need to be combined with a different funding scheme. It can be seen that any deterioration in the economic conditions did not negatively affect the profitability of the retrofit. This was caused by the fact that, with the increase in the initial investment, the energy costs also increased. This can be considered realistic because, percentage-wise, energy costs are likely to increase more rapidly than the investment costs in time of crisis. The outcome would be different if the investment increased much more dramatically than the energy costs.

The payback for the favourable economic development (INV -10%, EP -10%) was almost identical to that for the baseline scenario. However, in the current situation, neither of these two developments is likely to happen in the foreseeable future. The more pessimistic developments are more likely to occur. It is seen that with any negative developments in the economy, that is, with the increase of the investments but mainly of the energy costs, the payback decreased down to five years. Regardless of the economic developments considered, the payback was reasonably low, indicating potential suitability for EPC.

The potential suitability for EPC is retained even if we take into consideration the uncertainty ranges, which are indicated by the error bars in Fig. 2. In the figure, the points represent the middle values, and the error bars represent the lower and upper values from Table 5. The lower and upper uncertainty ranges are not symmetrical, and the upper uncertainty range is wider than the lower range. For the EPC project, the upper uncertainty range is relevant because it signifies the risk that the payback will exceed the duration of the contract. The uncertainty decreases with the deterioration of the economic situation. Increases in investments and energy prices are likely to occur. In such a case, the upper uncertainty range is 2-3 years. In the two developments with the highest prices (INV +50%, EP +100% and INV +100%, EP+150%), the expected payback was up to seven years, also taking the uncertainty into account. This suggests the suitability of the retrofit project for EPC.

3.2.3 Suitability for EPC – Building II

The results for Building II were somewhat similar to those for Building I (Table 7). The optimistic economic developments (INV -10%, EP -10% and Baseline) were not suitable for EPC, whereas the developments that involved cost increases were po-

Tab. 6 *Inputs and discounted payback for the various economic developments for Building I*

Economic development	Value	Investment (€)	Inputs varied			RAT_{disc}	PB	RAT_{disc}	PB
			Electricity costs	**Heat costs**	**Energy savings**				
			(€/MWh)		**(kWh/a)**	**(%)**	**(a)**	**(%)**	**(a)**
1 INV -10%, EP -10%	lower	239,910	165	165	384,620	3	4	0	4
	middle	269,899	135	135	320,517	3	7	0	6
	upper	299,887	105	105	256,414	3	12	0	10
2 **Baseline** (INV 0%, EP 0%)	lower	269,899	180	180	384,620	3	4	0	4
	middle	**299,887**	**150**	**150**	**320,517**	**3**	**7**	**0**	**6**
	upper	329,876	120	120	256,414	3	11	0	10
3 INV +30%, EP +50%	lower	359,865	254	255	384,620	3	4	0	3
	middle	389,853	224	225	320,517	3	6	0	5
	upper	419,842	194	195	256,414	3	9	0	8
4 INV +50%, EP +100%	lower	419,842	329	330	384,620	3	3	0	3
	middle	449,831	299	300	320,517	3	5	0	4
	upper	479,820	269	270	256,414	3	7	0	6
5 INV +100%, EP +150%	lower	246,346	404	122	384,620	3	3	0	3
	middle	259,312	374	113	320,517	3	5	0	4
	upper	272,277	344	104	256,414	3	7	0	6

Explanation: INV – investment, EP – energy costs

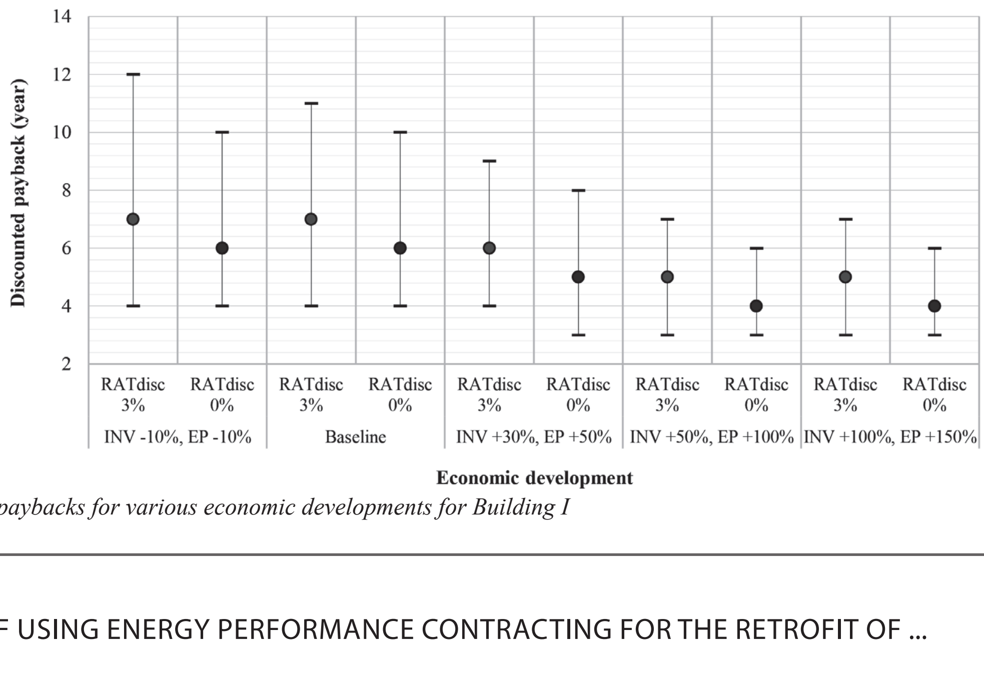

Fig. 2 *Discounted paybacks for various economic developments for Building I*

tentially suitable, especially the two most pessimistic ones (INV +50%, EP +100% and INV +100%, EP+150%). However, Fig. 3 shows that unlike Building I, in this case, the upper uncertainty level in the favourable developments (INV -10%, EP -10% and Baseline) exceeded 20 years, thus indicating a risk of exceeding the maximum contract duration of 15 years. The middle payback for these developments was eight to nine years, and the upper calculation of uncertainty was 12 years. The difference in payback, and, therefore, suitability for EPC, between the buildings, was partially caused by the difference in the cost of heat. This was because in Building II, the heat sources were gas boilers installed in the buildings; therefore the heating costs were lower. Lower heating costs mean less financial savings.

4 CONCLUSIONS

The present study has summarized the potential of various retrofit measures that can be applied to apartment buildings constructed several decades ago using old technologies. The measures were assembled into retrofit packages, and their suitability for financing through EPC was studied. The specifics of EPC are that it needs to generate enough revenue for the provider within a relatively short time frame and also cover the uncertainties in profitability calculations. Therefore, a suitable retrofit must be selected for the EPC project to achieve a reasonable payback. Research on this topic is scarce, even on the international level. Furthermore, existing studies did not consider using EPC to finance the retrofit of apartment buildings. The present research adds to the existing knowledge in this regard. The results refer to selected apartment buildings in Slovakia but are also applicable in other countries with a similar climate and building construction technologies.

The retrofit measures in technical systems were shown to be considerably more feasible than the retrofit of the building envelope. Therefore, the potential to finance the selected package of retrofit measures for technical systems through EPC was further evaluated. Five possible economic developments, representing different starting points in terms of investments and energy costs, were devised. It was shown that even with filtering out potentially unfeasible retrofit measures, the profitability and suitability of EPC depended significantly on economic developments. For

Tab. 7 *Inputs and discounted payback for the various economic developments for Building II*

Economic development	Value	Investment (€)	Inputs varied			RAT_{disc}	PB	RAT_{disc}	PB
			Electricity costs	**Heat costs**	**Energy savings**				
			(€/MWh)		**(kWh/a)**	**(%)**	**(a)**	**(%)**	**(a)**
1 INV -10%, EP -10%	lower	111,342	165	50	144,609	3	7	0	6
	middle	125,260	135	41	120,507	3	13	0	11
	upper	139,178	105	32	96,406	3	22	0	17
2 **Baseline**	lower	125,260	180	54	144,609	3	7	0	6
	middle	**139,178**	**150**	**45**	**120,507**	**3**	**13**	**0**	**11**
	upper	153,095	120	36	96,406	3	21	0	16
3 INV +30%, EP +50%	lower	167,013	254	77	144,609	3	6	0	6
	middle	180,931	224	68	120,507	3	10	0	9
	upper	194,849	194	59	96,406	3	15	0	13
4 INV +50%, EP +100%	lower	194,849	329	99	144,609	3	5	0	5
	middle	208,766	299	90	120,507	3	8	0	7
	upper	222,684	269	81	96,406	3	12	0	10
5 INV +100%, EP +150%	lower	264,438	404	122	144,609	3	6	0	5
	middle	278,355	374	113	120,507	3	9	0	8
	upper	292,273	344	104	96,406	3	12	0	10

Explanation: INV – investment, EP – energy costs

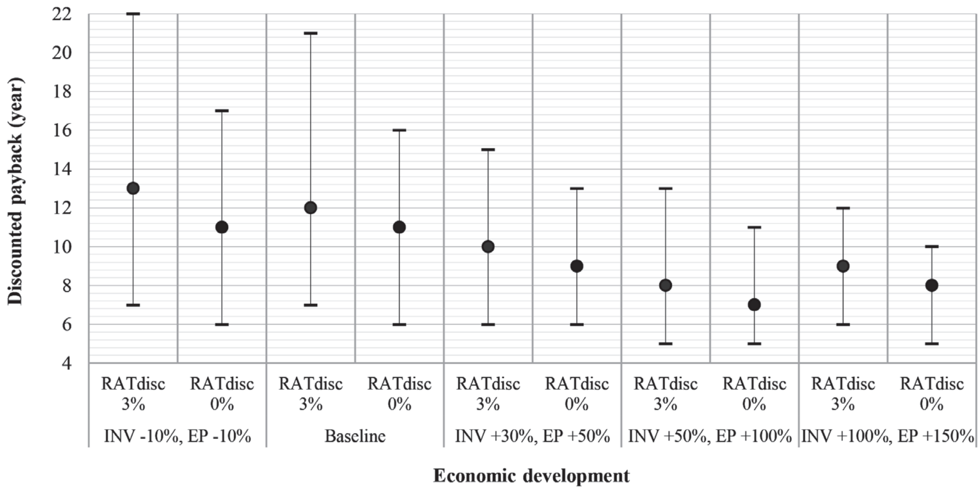

Fig. 3 *Discounted paybacks for various economic developments for Building II*

both buildings considered, financing the retrofit through EPC was realistic. However, it was shown that the use of EPC may not be preferred in a favourable economic situation involving relatively low energy costs. At least for one of the two buildings studied, the EPC was recommended only for economic developments that involved a sharp increase in energy costs.

Furthermore, the paybacks were 1-2 years shorter when assuming a discount rate of 0% instead of 3%. These findings suggested that a negative economic outlook, especially an increase in energy costs, and an incentive for energy-efficient retrofits to support the economy and reduce dependence on fuel imports (represented by the zero discount rate), help make the EPC a suitable financing method for building retrofits. However, this pertains only to the measures selected in the technical systems. For a complex retrofit, the EPC must be combined with another financing method.

Acknowledgements

This work was supported by the Ministry of Education, Science, Research and Sports of the Slovak Republic grants VEGA 1/0303/21 and 1/0304/21 and KEGA 005STU-4/2021 and Brno University of Technology project FAST-S-22-8060.

REFERENCES

National Council of the Slovak Republic (2014) Act No. 321/2014 Coll. on energy efficiency and on the amendment of certain laws.

Bizzarri, G. – Morini, G.L. (2006) *New technologies for an effective energy retrofit of hospitals*. Applied Thermal Engineering, 26, pp. 161-169. DOI: 10.1016/j.applthermaleng.2005.05.015.

Cholewa, T. – Balaras, C.A. – Kurnitski, J. – Mazzarella, L. – Siuta-Olcha, A. – Dascalaki, E. – Kosonen, R. – Lungu, C. – Todorovic, M. – Nastase, I. – Jolas, C. – Çakan, M. (2022) *Energy efficient renovation of existing buildings for HVAC professionals*, Brussels: REHVA, 2022, 103 pp. ISBN 978-2-930521-31-2.

Dahlsveen, T. – Petráš, D. – Chmúrny, I. – Smola, A. – Lulkovičová, O. – Füri, B. – Konkoľ, R. (2008) *Energetický audit a certifikácia budov (Energy audit and certification of buildings)* [in Slovak], Bratislava: Jaga Group, 2008. 163 pp. ISBN 978-80-8076-063-2.

Dipasquale, C. – Fedrizzi, R. – Bellini, A. – Gustaffson, M. – Ochs, F. – Bales, C. (2019) *Database of energy, environmental and economic indicators of renovation packages for European residential buildings*. Energy and Buildings, 203, 109427. DOI: 10.1016/j.enbuild.2019.109427.

EN ISO 52016-1:2017 Energy performance of buildings. Energy needs for heating and cooling, internal temperatures and sensible and latent heat loads. Part 1: Calculation procedures.

EN 15316-2:2017 Energy performance of buildings - Method for calculation of system energy requirements and system efficiencies - Part 2: Space emission systems (heating and cooling).

EN 15316-3:2017 Energy performance of buildings - Method for calculation of system energy requirements and system efficiencies - Part 3: Space distribution systems (DHW, heating and cooling).

EN 15316-5:2017 Energy performance of buildings - Method for calculation of system energy requirements and system efficiencies - Part 5: Space heating and DHW storage systems (not cooling).

EN 15316-4-3:2017 Energy performance of buildings - Method for calculation of system energy requirements and system efficiencies - Part 4-3: Heat generation systems, thermal solar and photovoltaic systems.

EN 15459-1:2007 Energy performance of buildings. Economic evaluation procedure for energy systems in buildings. Part 1: Calculation procedures.

European Commission (2017) *Update of the Residential and Non-residential Building Stock Renovation Strategy, Slovak Republic*. Available at: https://ec.europa.eu/energy/sites/ener/files/documents/update_of_the_residential_and_non-residential_building_stock_renovation_strategy_slovak_republic.pdf (Accessed 3 August 2022).

European Commission (2022 a) *A European Green Deal: Striving to be the first climate-neutral continent*. Available at: https://ec.europa.eu/commission/presscorner/detail/en/ip_21_6683 (Accessed 7 July 2022).

European Commission (2022 b) *Energy Service Companies (ESCos)*. Available at: https://e3p.jrc.ec.europa.eu/node/190 (Accessed 7 July 2022).

European Commission (2022 c) *Photovoltaic geographical information system*. Available at: https://re.jrc.ec.europa.eu/pvg_tools/en/tools.html (Accessed 7 July 2022).

Faggianelli, G.A. – Mora, L. – Merheb, R. (2017) *Uncertainty quantification for Energy Savings Performance Contracting: Application to an office building*. Energy and Buildings, 152, pp. 61-72. DOI: 10.1016/j.enbuild.2017.07.022.

Giretti, A. – Vaccarini, M. – Casals, M. – Macarulla, M. – Fuertes, A. – Jones, R.V. (2018) *Reduced-order modeling for energy performance contracting*. Energy and Buildings, 167, pp. 216-230. DOI: 10.1016/j.enbuild.2018.02.049.

Gustafsson, M. – Dipasquale, C. – Poppi, S. – Bellini, A. – Fedrizzi, R. – Bales, C. – Ochs, F. – Sié, M. – Holmberg, S. (2017) *Economic and environmental analysis of energy renovation packages for European office buildings*. Energy and Buildings, 148, pp. 155-165. DOI: 10.1016/j.enbuild.2017.04.079.

Kuusk, K. – Kalamees, T. – Maivel, M (2014) *Cost effectiveness of energy performance improvements in Estonian brick apartment buildings*. Energy and Buildings, 77, pp. 313-322. DOI: 10.1016/j.enbuild.2014.03.026.

Kuusk, K. – Kalamees, T. (2015) *Retrofit cost-effectiveness: Estonian apartment buildings*. Building Research & Information, 44, pp. 920-934. DOI: 10.1080/09613218.2016.1103117.

Labanca, N. – Suerkemper, F. – Bertoldi, P. – Irrek, W. – Duplessis, B. (2015) *Energy efficiency services for residential buildings: market situation and existing potentials in the European Union*. Journal of Cleaner Production, 109, pp. 284-295. DOI: 10.1016/j.jclepro.2015.02.077.

Lee, P. – Lam, P.T.I. – Lee, W.L. (2018) *Performance risks of lighting retrofit in Energy Performance Contracting projects*. Energy for Sustainable Development, 45, pp. 219-229. DOI: 10.1016/j.esd.2018.07.004.

Ministry of Transport and Construction of the Slovak Republic (MDV SR) (2020) *Dlhodobá stratégia obnovy fondu budov (Long-term strategy of renovation of the building stock)* [in Slovak]. Available at: https://ec.europa.eu/energy/sites/default/files/documents/sk_2020_ltrs.pdf (Accessed 3 August 2022).

Patiño-Cambeiro, F. – Armesto, J. - Patiño-Barbeito, F. – Bastos, G. (2016) *Perspectives on Near ZEB Renovation Projects for Residential Buildings: The Spanish Case*. Energies, 9, pp. 628-643. DOI: 10.3390/en9080628.

Principi, P. – Fioretti, R. – Carbonari, A. – Lemma, M. (2016) *Evaluation of energy conservation opportunities through Energy Performance Contracting: A case study in Italy*. Energy and Buildings, 128, pp. 886-899. DOI: 10.1016/j.enbuild.2016.06.068.

Ramos, J.S. – Guerrero Delgado, M. – Álvarez Dominguez, S. – Félix Molina, J.L. – Sánchez de la Flor, F. – Tenorio Rios, J.A. (2019) *Systematic Simplified Simulation Methodology for Deep Energy Retrofitting Towards Nze Targets Using Life Cycle Energy Assessment*. Energies, 12, pp. 3038-3064. DOI: 10.3390/en12163038.

STN 73 0540-2+Z1+Z2:2019 *Tepelná ochrana budov. Tepelnotechnické vlastnosti stavebných konštrukcií a budov.* Časť *2: Funkčné požiadavky*. Konsolidované znenie (*Thermal protection of buildings. Thermal performance of buildings and components. Part 2: Functional requirements*) [in Slovak].

Vargová, A. – Ingeli, R. (2021) *Assessment of the energy demands for heating in a historic building. Case study: Renewal of a functionalist building of the infectious diseases pavilion in Topoľčany, Slovakia*. Slovak Journal of Civil Engineering, 29, pp. 29-36. DOI: 10.2478/sjce-2021-0025.

Życzyńska, A. – Suchorab, Z. – Dyś, G. – Čurpek, J. – Čekon, M. (2020) *An evaluation of the structure of energy consumption in educational buildings in Poland after thermal retrofitting*. Slovak Journal of Civil Engineering, 28, pp. 29-37. DOI: 10.2478/sjce-2020-0028.

sciendo Slovak Journal of Civil Engineering

Vol. 30, 2022, No. 3, 43 – 52
DOI: 10.2478/sjce-2022-0020

THE IMPACT OF CAR TRANSPORT ON THE ENVIRONMENT AND PUBLIC SPACES IN CITIES: CASE STUDY FROM SLOVAKIA

Michal FEIK[1*]

Abstract

The increasing traffic volume of individual car transport results in environmental damage and new space requirements for parking. Parked cars occupy public space that a municipality could use for non-transport purposes. An effective urban parking policy is a solution that could influence transport and significantly improve the quality of public spaces and the environmental burden of traffic. Effective parking management can increase revenues to a city budget to be used for further urban development. The regulation of parking and charging are unpopular topics for politicians. They are afraid of the adverse reactions of local inhabitants and fear that they will not be re-elected. However, experience has shown that if the process and implementation of regulated parking are well managed, citizens will appreciate its benefits. People will begin to value public space more and transform it into space for all residents and not just car owners. The goal of this paper is to present research in which people were asked what they would motivate them to use a different mode of transport instead of a car. The most common answer was more public transport connections and cheaper traveling or traveling free of charge.

Address

[1] Dept. of Transportation Engineering, Faculty of Civil Engineering, Slovak University of Technology, Bratislava, Slovak Republic

* ***Corresponding author:*** michal@feik.sk

Key words

- Public space,
- Car ownership,
- Parking policy.

1 INTRODUCTION

The increasing of traffic volume negatively impacts the environment and results in new requirements for static transport solutions. Parked cars occupy public spaces that could be used for non-transport purposes, i.e., leisure, sports or culture, the planting of trees or greenery, and setting up of pedestrian zones. However, residential structures have their spatial limits, so the lack of parking spaces results in unregulated parking outside legal parking places, e.g., on sidewalks, at public transport stops, in intersections, and often on greenery.

There is empirical evidence relating to the impact of parking policy measures on demands for parking and travel (Feeney & Feeney, 1989). The more parking spaces in a city, the more cars go to the city. The absence of parking regulations in urban environments exacerbates this problem.

An effective urban parking policy is a solution that can influence transport and significantly improve the quality of public spaces and reduce the environmental burden caused by transport. Finally, efficient static transport management can bring funds to city budgets that can be used for further urban development.

1.1 Impact of transport on the environment

Transport causes significant external effects that have a harmful impact on the environment, human health, and the economy. The costs of these external effects (congestion, accidents) are not

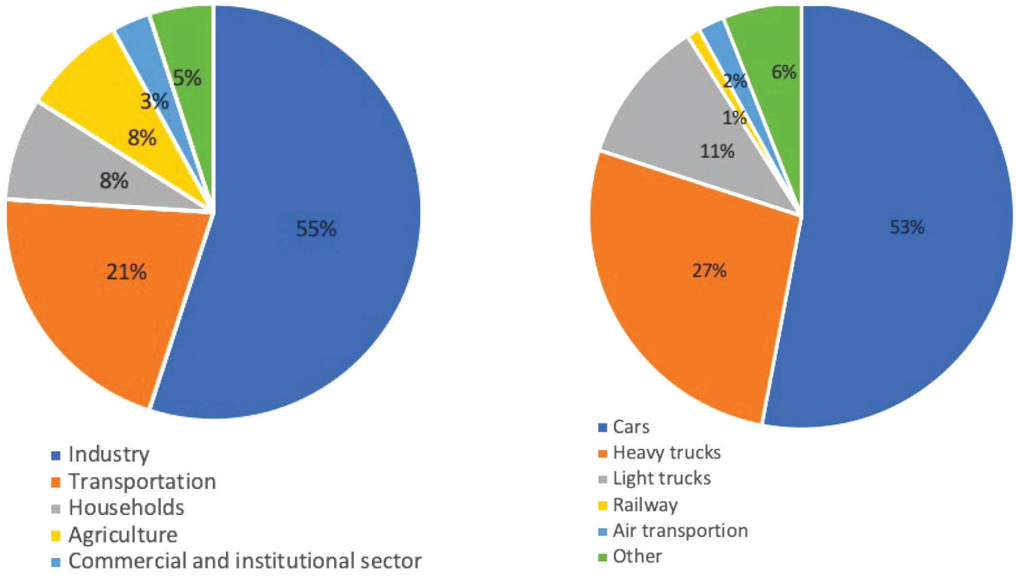

Fig. 1 *Emissions in Slovakia according to sectors and transport modes*

borne directly by those who cause them, but by other road users and society as a whole (environmental pollution costs). This results in making wrong decisions in the transport market, which further leads to an inefficient use of available resources and the loss of social welfare (Petrović, 2022). The problem of road transport is also related to safety and the accident rate (Sándor, 2020).

Transport consumes one third of all energy in the EU. The bulk of this energy comes from oil. This means that transport is responsible for a large share of the EU's greenhouse gas emissions and is a major contributor to climate change. While many other economic sectors, such as power production and industry, have reduced their emissions since 1990, those related to transport have risen. They now account for more than one quarter of the EU's total greenhouse gas emissions. A reversal of this trend is currently not in sight, which makes the transport sector a major obstacle to realizing the EU's climate protection goals. Cars, vans, trucks, and buses produce more than 70% of the overall greenhouse gas emissions from transport. The remainder mainly comes from shipping and aviation (European Environment Agency, 2021).

Transport continues to be a significant source of air pollution, especially in cities. Air pollutants, such as particulate matter (PM) and nitrogen dioxide (NO_2), harm human health and the environment. Although air pollution from transport has decreased in the last decade because of the introduction of fuel quality standards, the Euro vehicle emission standards and the use of cleaner technologies, air pollutant concentrations are still too high (European Environment Agency, 2021).

Noise pollution is another major environmental health problem linked to transport. Road traffic is the most widespread source of noise, with more than 100 million people affected by harmful levels in the EEA's member countries. Air traffic and railways are also major sources of noise. Furthermore, transport infrastructure has a serious impact on the landscape because it divides natural areas into small patches with serious consequences for animals and plants (European Environment Agency, 2021).

The contribution of fuel combustion in transport to total greenhouse gas emissions in Slovakia was about 21 % in 2019 and has increased significantly since 1990 (Fig. 2). Although greenhouse gas emissions in Slovakia have decreased over the medium term, transport emissions have increased. Cars contribute to emissions in the transport sector (Fig. 1) by up to 53 % of the emissions in the transport sector (National Bank of Slovakia, 2021).

The impact of cars on the environment is enormous. From the factory to the scrap yard, cars consume resources. They pollute the air, soil, and water. Car production requires a large number of natural resources such as metal, glass, plastic, rubber, and other materials. Manufacturing itself consumes energy, and the factory itself produces a lot of waste and emissions. Cars on the road are significant consumers of oil and gas, which requires increased extraction, transportation, and refining of petroleum products. Since the internal combustion engine continues to dominate automobile propulsion, cars release large amounts of emissions into the air and produce noise, used oil, and disposable parts. Abandoned or scrapped vehicles are on the rise (Melosi, 2019).

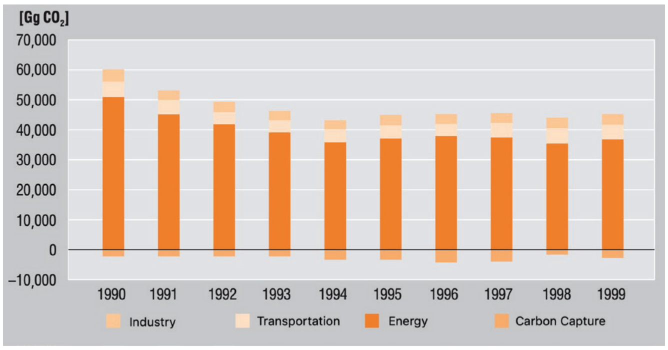

Fig. 2 *The share of sectors in the economy in the production of greenhouse gas emissions. Slovakia 1990-1999 (Ministry of the Environment of the Slovak Republic, 2001)*

Despite the above mentioned facts, car manufacturers try to convince consumers that car transport is environmentally friendly and sustainable. They invest large sums of money in media campaigns. In the European Union, the top 20 car brands spent 3.94 **billion** € on TV and print advertising in 2017 (Statista Research Department, 2017). Car manufacturers are also big advertisers in Slovakia. Volkswagen Slovakia, which owns the brands of Volkswagen, Audi, Porsche, Seat, and Skoda, spent 107 million € on sales and marketing services in 2019 (Volkswagen Slovakia, 2019).

1.2 Increase in number registered cars

In the period under consideration, the stock of passenger cars presented a trend of continuous growth. Between 1990 and 2017, the number of registered cars in the 28 European Union member states increased from 163 million to 264 million (Fig. 2). In 2017, the number of registered passenger cars in the EU 28 reached 264.2 million vehicles (Statista, 2017).

The total amount of registered vehicles in Slovakia since 1983 has increased from less than 1.3 million to the current number of more than 3.3 million (Fig. 3). In half a century, the number of registered motor vehicles has increased up to 15 times. In 1965, there were only 28,000 cars. The number of cars has actually increased 30 times over the same period, to the current level of approximately 325,000 cars. Over the last decade, from 2010 to 2020, the number of cars in Bratislava increased by 38% (Statistical Office of the Slovak Republic, 2020). A significant increase was recorded in the 1990s when the number of cars increased by 70% compared to the previous decade. However, parking capacities have not increased proportionally.

The amount of urban space has its limits; it is therefore impossible to build new parking spaces indefinitely. Drivers usually solve the lack of parking spaces in the streets of Slovak cities by spontaneously parking outside the legal parking places. They park in bus lanes, on sidewalks, at public transport stops, in curves and intersections, or on the grass. At the same time Slovak legislation legally allows parking on sidewalks (Slovak National Council, 2009).

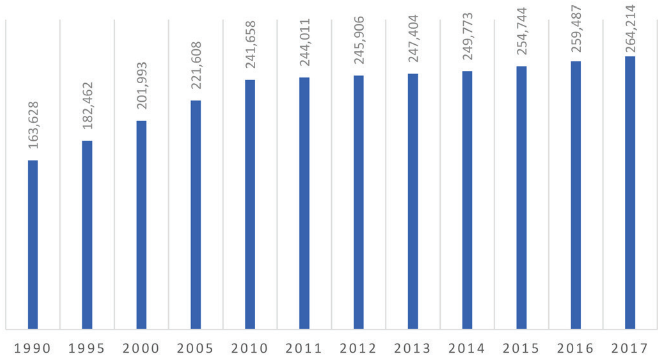

Fig. 3 *Registered passenger cars in Europe 1990-2017* (Statista, 2017)

An effective parking policy seems to be a solution that could influence traffic dynamics. It could also make a significant contribution to improving the quality of public space. However, it is highly unpopular in Slovakia. The share of toll parking places in the largest Slovak cities reaches less than 5% of the total parking places. The average annual fee per inhabitant was approximately 6,9 € in 2020 in Slovakia.

1.3 Public space

The occupation of land by the transport infrastructure in 2018 represented 0.56% of the total area of the Slovak Republic (4,903,407 ha) (Enviroportál, 2018). The total area occupied by parked cars in Slovakia is not known, but we believe that considering approximately 3.35 million vehicles are registered in Slovakia and that one parking space occupies 10.125 m^2 (according to the technical standard of 2.25 x 4.5 m), all the vehicles occupy an area of 33,917,000 m^2 (Office for Standardization, Metrology and Testing of the Slovak Republic, 2014). That is the equivalent of more than 4,750 national football stadiums (National Football Stadium, 2022). The length of these cars would form a column more than 15 million meters long.

Car transport can take up a lot of space. Fifty people in 33 cars occupy an area of 334 m^2; 50 people on a bicycle occupy an area of 125 m^2, while 50 people in one bus occupy only 33 m^2. A visual comparison is in Fig. 5 (Citizen Cycling Initiative Banská Bystrica, 2018).

1.4 Parking on sidewalks in Slovakia

The general possibility of parking on sidewalks in Slovakia was made possible by Act No. 8/2009 on road traffic in 2009 (National Council of Slovak Republic, 2009) if the driver leaves a pedestrian walking area of at least 1.5 meters wide. The argument for parking on the sidewalks was the lack of formal parking

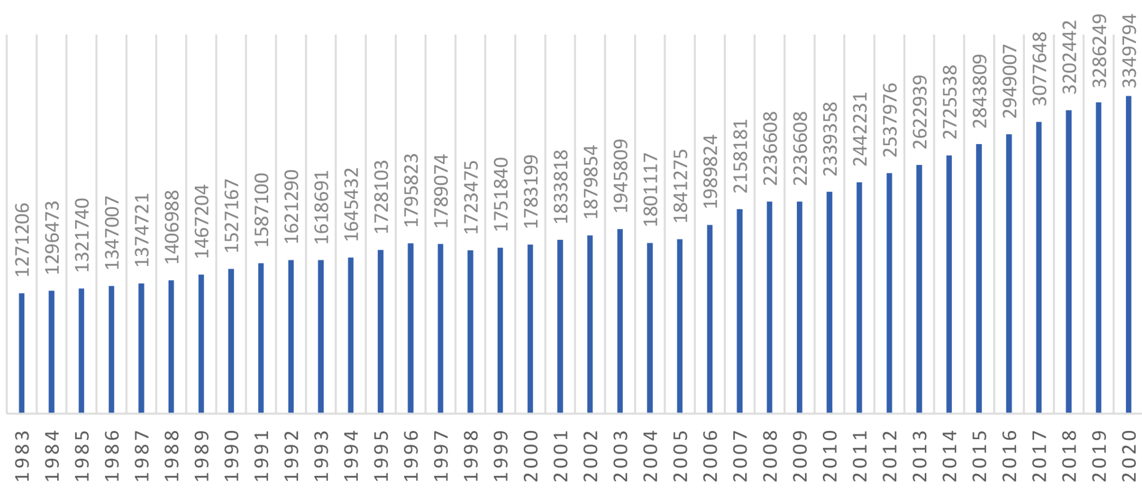

Fig. 4 *Number of registered vehicles in the Slovak Republic* (Ministry of the Interior of the Slovak Republic, 2020)

Fig. 5 *Comparison of the space requirements for the static transport of 40 people using different modes of transport - car, bus, and bicycle during the European Mobility Week in Banská Bystrica (Citizen Cycling Initiative, Banská Bystrica, 2013)*

Fig. 6 *Breaking the rules (bus stop, pedestrian crossing, on the grass)*

spaces, but it has brought about a massive amount of negative effects. The number of cars on the streets, congestion, and transport time has increased, and the environment has become even more degraded by emissions, dust, and noise. The public space has consequently decreased.

Most sidewalks were not constructed for the load that cars can cause. As a result, curbs, cracked and missing asphalt, potholes, holes, depressions, and the sidewalks themselves have been destroyed. Municipalities spend considerable resources on repairs and make walking uncomfortable for pedestrians. The barriers those cars create on the sidewalks are also a problem. The safety of pedestrians has been reduced. The big problem is parked cars at public transport stops, intersections or pedestrian crossings.

General parking on the sidewalks was abolished by an amendment to the Road Traffic Act in 2021 by mistake. Members of Parliament therefore re-introduced the possibility of parking cars on the sidewalk in 2022.

2 RESEARCH METHODS AND METHODOLOGY

Data from the eight largest cities in Slovakia was analysed for the research; it was processed using standard statistical methods. Quota surveys of public opinion were conducted using the Com-

Fig. 7 *Parking on sidewalks in Slovakia is legal.*

Tab. 1 *Parking strategies*

Strategy	Description
regulation	according to the type of vehicles or users
parking time restrictions	e.g., 10-minute supply zones, 30-minute parking near shop entrances, 1- or 2-hour street parking restrictions for shopping purposes) to boost turnover and favor shorter-time users
motivating employees	to use less attractive parking spaces during peak hours (for example, parking spaces on the outskirts of urban areas) to leave parking spaces for customers
higher parking fees	in more attractive zones and shorter intervals - for example, in areas with a high degree of attractiveness, introduce charging in 15-minute intervals, for a maximum of two hours, while in less attractive zones, charge lower amounts and extend the upper limit of the parking time to 4 hours, for example, without smaller periods
more flexible pricing methods	allowing motorists to pay only for actual parking time, making shorter parking time more attractive
restricting street parking	in residential areas or providing a discount for residents
restriction of parking of large vehicles on the street	e.g., vehicles over 3.5 tons are able to facilitate traffic and discourage the use of public parking for parking trucks or commercial vehicles
permission to park vehicles only for M1 category	exclusion of other categories, e.g., in housing estates
ban on-street parking	at selected locations and times (for example, during peak hours) to increase the number of lanes
allow off-peak street	parking using one of several lanes

Source: (Litman, Parking Management, Strategies, Evaluation and Planning, 2008)

puter Aided Technology method (CATI). Quotas are a specific number or percentage that a survey needs to meet by screening in participants that meet the requirements. They are based on demographics (age, sex, education, and region of residence). The research sample was representative of the population of the Slovak Republic and the Bratislava Region.

A significant part of the resources came from public institutions such as the Ministry of Transport and Construction of the Slovak Republic, Capital City of Bratislava, the Ministry of the Environment, the Ministry of the Interior of the Slovak Republic, the Slovak Road Administration, the Statistical Office of the Slovak Republic, and the European Commission.

In the article legislative and non-legislative regulations in Slovakia and in the European Union, which come from national legislation, technical standards and technical regulations were analysed. Sources outside of Slovakia mainly consist of the European Commission, ministries and municipalities.

The Parking methodology was based on a National project of the modernization of municipalities, the Association of Municipalities of Slovakia, the Act on Road Traffic, the Slovak technical standard "Parking and parking areas of vehicles", as well as the technical regulation "Principles of design of traffic calming elements." The design of the methodology was based on the general regulations of Bratislava, the Capital City.

3 RESULTS

3.1 Parking policy strategy

A parking strategy serves for efficient static traffic management. Various parking strategies are intended to act as a regulation of static traffic, i.e., to discourage using a car. Here are the most often used strategies (Litman, Parking Management, Strategies, Evaluation and Planning, 2008).

3.2 Analysis of parking in Slovakia

As part of the research task, data was analyzed in 2020 from the eight largest cities in Slovakia, which are also regional headquarters. The input values were the population, the number of regulated parking places, the number of inhabitants, and revenues from parking. The output values were the number of regulated parking places per 1000 inhabitants, the number of registered cars per 1000 inhabitants, and the revenues from parking per inhabitant.

The results (Tab. 3) show a high level of car ownership and a low level of parking regulation in Slovakia. The average number of regulated parking places per 1,000 inhabitants is 48.62, while the average number of registered cars per 1,000 inhabitants is 800.72.

Tab. 2 *Analysis of parking in Slovakia – inputs*

City	Population	Number of regulated parking places	Number of registered cars	Annual revenue from parking (€)
Bratislava	429,564	27,285	326,228	267,4041
Košice	239,095	8277	95,869	830,156
Prešov	89,138	1185	64,743	338,489
Žilina	80,978	3915	72,816	558,218
B. Bystrica	78,484	1922	50,007	371,324
Nitra	77,048	1902	81,320	732,952
Trnava	65,382	1350	66,018	1,095,848
Trenčín	55,537	8852	50,954	1,103,233
Total	**1,115,226**	**54,688**	**80,795**	**7,704,261**

Tab. 3 *Analysis of parking in Slovakia - outputs*

City	Number of regulated parking spots per 1000 inhabitants	Number of registered cars per 1000 inhabitants	Annual revenue from parking per inhabitant (€)
Bratislava	63.52	759.44	6.23
Košice	34.62	400.97	3.47
Prešov	13.29	726.32	3.80
Žilina	48.35	899.21	6.89
B. Bystrica	24.49	637.16	4.73
Nitra	24.69	1055.45	9.51
Trnava	20.65	1009.73	16.76
Trenčín	159.39	917.48	19.86
Average	**48.62**	**800.72**	**6,91**

In Slovakia, municipalities on average, receive 6.91 € per capita per year for parking. The table above answers the question of why the demand for car transport in Slovakia is not being reduced. Parking fees and fines represent contested issues in cities, as they conflict with vehicle owners' opinions over 'rights' to public space. As cities have moved to regulate vehicle density by introducing parking fees, a certain share of drivers may feel compelled to "cheat", i.e., weigh the price of parking fees against the price of fine or simply parking illegally outside designated areas (Gössling, Humpe, Hologa, Riach, & Freytag, 2022).

3.3 Quantitative public opinion poll

In 2019, as part of a research task at the Ministry of Agriculture and Rural Development, was conducted a representative nationwide public opinion survey. It aimed to find out the population's opinion on topics related to rural development, including transportation. Citizens' views on mobility were also an essential part of the survey. Respondents were asked, "What would motivate you to use a different mode of transport instead of a car?" The most common answer (14.7%) was "more public transport connections." In second place (12.6%) was "cheaper transport" or "traveling free of charge."

N = 2000
Sample = representative sample
Data collection: 30.8. - 5.9.2019
Data collection methodology: quota characters
Quota characters: age, sex, education, and region of permanent residence.
Research sample: quota survey

As part of a research task on the Bratislava Region, the research team carried out a local public opinion survey in 2020. The same question was asked to the respondents as in the nationwide survey: "What would motivate you to use a different means of transport instead of a car?"

N = 600
Sample = representative sample
Data collection: 1.12. - 15.12.2020
Quota characters: age, sex, education, region of residence (Bratislava region).
Research sample: the research sample is representative of the population of the Bratislava region in all quota characters.

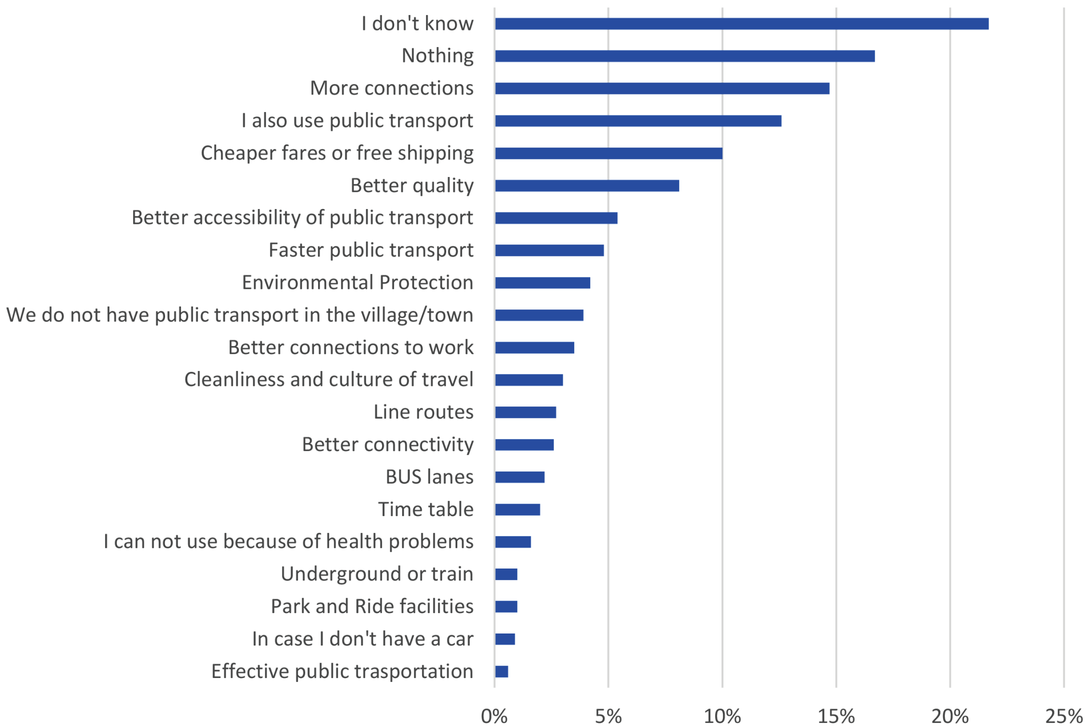

Fig. 8 *What would motivate you to use a different mode of transport instead of a car? (multiple answers possible)*

 Vol. 30, 2022, No. 3, 43 – 52

Tab. 4 *What would motivate you to use a different mode of transport instead of a car? (multiple answers possible)*

Answer	Rate
I am dependent on a car (illness, work tools, distance)	37.09%
Better public transport (more modern, clean, cost, frequency, and interconnection)	33.28%
Better conditions for cyclists	11.61%
Other	18.02%

In Slovakia, 10% of the respondents answered that the motivation to use public transportation instead of a car would be a lower cost or traveling for free. The effectiveness of this strategy is confirmed by the case of Tallinn, Estonia, in which a full-scale experiment provided a unique opportunity to investigate the impacts of free-fare public transport (FFPT). Almost a year after the introduction of FFPT in year, public transport usage increased by 14%; moreover, there is evidence that the mobility of low-income residents has improved. The effect of FFPT on ridership is substantially lower than those reported in previous studies due to the good level of service provision, high public transport usage, and low public transport fees that already existed prior to the FFPT (Susilo, Reimal, & Cats, 2017).

Another public opinion poll was conducted in 2022. The main goal was to find out the opinions of Bratislava residents on the introduction of a parking policy, which was launched in February 2022. The survey sample consisted of two groups: residents living with an established parking policy and residents living without any parking regulation.

N = 1018
Sample = representative sample
Data collection: 21.3. – 29.4. 2022
Quota characters: age, sex, education, region of residence (Bratislava).
Research sample: online research

One third of the drivers could find a parking place more easily after the introduction of parking regulations. It remained the same for another third. More than half (55%) of the respondents considered an annual fee reasonable. One third thought it was too much. Up to 51% recommended introducing regulated parking throughout Bratislava. Less than a third were against it.

Among the drivers who did have regulated parking, one third supported the introduction of regulated parking. Less than a third was against it. Up to two-thirds of the drivers expected residents to be prioritized by the parking policy. About half of the people demanded more parking spots. Two thirds of the drivers thought that parking spaces should be constructed first and then parking fees should be charged. Less than a quarter of the people (23%) thought that the fee should be 5 € per month. Another quarter (24%) had no problem even with the amount of 10 € per month. On the contrary, 28% of the drivers thought that parking should be free.

3.4 Paradigm shift

In Slovakia, the lack of parking spaces is usually not solved by regulations, but by constructing (promising) new spaces. The reason is mainly pressure by citizens on their elected representatives. In local elections, politicians repeatedly promise to increase the number of parking spaces, even if it is not possible to do so indefinitely. However, a well-designed city parking policy brings many benefits: it removes chaos, regulates the demand for parking, and produces financial income to the city budget.

Parking planning is undergoing a paradigm shift, i.e., a fundamental change in how a problem is perceived and solutions evaluated. The old paradigm tended to resist change. It placed a heavy burden of proof on any innovations. The new paradigm recognizes that transport and land use conditions evolve so that parking planning practices need frequent adjustment. It shifts the burden of proof, allowing new approaches to be tried until their effectiveness is proven (Litman, Parking Management, Strategies, Evaluation and Planning, 2008). A possible solution based on the theories of Todd Litman is offered below (Tab. 5):

Tab. 5 *Comparing the old and new transportation paradigms*

The old transportation paradigm	The new transportation paradigm
The lack of parking spaces must be solved by building new ones.	Parking management is an effective solution to the lack of parking spaces.
The city must offer residents transportation alternatives before it introduces parking fees.	The solution to traffic in cities begins with the regulation of parking and the more efficient use of public spaces. Subsequently, drivers will then use alternative modes of transport such as public transport, walking, or cycling.
Parking should be free of charge, financed by local taxes.	Parking should be subject to a charge to regulate demand. In places of high demand for parking, fees should be higher.
Parking fees increase the already high cost of living.	Alternative modes of transport, such as public transport or bicycle transport, are cheaper for the population than car transport.
The population agree with the building of parking garages, but why build them in their backyard?	Reducing the number of cars will reduce the demand for parking spaces and garages. Instead, the municipality can build public spaces such as playgrounds, sports grounds, or parks.
It is the duty of the municipality to construct parking spaces.	The role of municipality is to develop sustainable and ecological mobility respecting public space.
If the municipality cancels our parking spaces, where can the population park their cars?	Alternative modes of transport, such as public transport or bicycle transport, require less space than car transport.
Parking regulations cause bad result for politicians in elections.	If the process and implementation are well managed, citizens will appreciate the benefits of regulated parking. People will begin to value public space more and transform it into a space for all residents, not just car owners.

3.5 Parking policy methodology

The regulation of and charging for parking are unpopular topics for politicians. They are afraid of the adverse reactions of the inhabitants and worried that they will not be re-elected. The absence of a widely understood typology of parking policy approaches is causing confusion in an important urban policy arena (Barter, 2015).

There is empirical evidence relating to the impact of parking policy measures on the demand for parking and for travel. Parking policy measures are a relatively important influence on modal choice (Feeney & Feeney, 1989).

The difference between the supply of and demand for available parking is the primary cause of congested traffic during commuting. Parking lots and parking spaces have a trade-off effect on congestion in sub-district. The adjustment the availability of parking outweighs land reconstruction in mitigating congestion, in terms of a low carbon urban development (Shen, Hong, Thompson, & Liu, 2020).

The aim of a parking policy is to create rules that bring about the efficient use of parking resources. Therefore, it is recommended that cities adopt a parking methodology that describes specific strategies and steps to help cities prepare and implement regulated parking. Based on experience from the implementation of parking rules in Slovakia the following parking methodology is proposed (Tab. 6).

Tab. 6 *Abstract of parking policy methodology*

Phase	Steps
Political decision	• Creating a project team • Preparation of a schedule • Gaining allies and supporters
Analysis of the current state	• Data collection • Analysis of existing legislation and technical standards
Analysis of the needs and goals of regional government	• Identification of measurable indicators • Determining the type of regulation • Pricing policy proposal • Parking policy proposal • Proposed technical solution
Participatory process and public communication	• Presentation of goals • Gathering comments • Processing of comments
Pilot project	• Testing the proposed rules in the selected location • Evaluation of the pilot project • Revision of the parking policy draft
Legislation	• Final draft parking policy • Preparation of implementing regulations • Approval by the regional council
Implementation	• Procurement of goods and services (project documentation, data collection, information and payment systems, parking control equipment) • Technical implementation • Start registration • Start operation
Monitoring and evaluation	• Compliance check • Sanctions • Evaluation of measurable indicators • Observing behaviour and improving the existing system • Troubleshooting

4 CONCLUSIONS

Increases in traffic volumes result in new requirements for static transport solutions and environmental damages. Transport consumes one-third of all the energy in the EU. The transport infrastructure seriously impacts the landscape because it divides natural areas into small patches with severe consequences for animals and plants. Transport continues to be a significant source of air pollution, especially in cities. Noise pollution is another major environmental health problem linked to transport.

The contribution of fuel combustion in transport to total greenhouse gas emissions in Slovakia was about 21% in 2019 and has increased significantly since 1990. Cars contribute to emissions in the transport sector by up to 53% of the emissions in the transport sector.

Between 1990 and 2017, the number of registered cars in Europe increased from 163 million to 264 million. In Slovakia, the number of registered cars increased from 1.5 million to approximately 3.1 million in the same period. According to the Slovak technical standard, one parking space has dimensions of 2.25 x 5 meters (11.25 m^2), so the area of parking cars in Slovakia is roughly 35 million m^2. These cars would form a column more than 15 million meters long.

The absence of parking regulations in urban environments exacerbates the problem. Parking cars occupy public space that could be used for non-transport purposes. The average number of regulated places in Slovakia per 1000 inhabitants is 48.62, while the average number of registered cars per 1000 inhabitants is 800.72. On average, municipalities receive 6.91 € per capita for parking. An effective urban parking policy would seem to be the solution; it can influence transport and significantly contribute to improving the quality of public spaces and reducing the environmental burden caused by transport. Finally, efficient parking management brings funds to city budgets that can be used for further urban development.

There are several obstacles to implementing a parking policy in cities, i.e., a lack of traffic data, a lack of methodology, and the resistance of the population. A parking strategy serves for efficient static traffic management. Various parking strategies are intended to act as a regulation of static traffic, i.e., to discourage using a car.

Based on the above data collection, the income from parking in Slovak cities is significantly undersized. The average number of regulated places per 1000 inhabitants in the eight largest cities is 48.40 €; the average revenue per inhabitant is 8.94 per year €. Among the 35 largest cities in Slovakia, only 7 of them are able to cover the costs of operating parking lots and parking systems with the revenues from parking.

The research for this paper shows that people in Slovakia most often go to work or school by car (52.7%). More than quarter (26.2%) use public transport, 10.5% walk, and 7.5% use bicycles. Residents in the Bratislava region use individual car transport even more: 71.86% drive by car and 22.65% use public transport.

When asked what would motivate the inhabitants of Slovakia to switch from cars to public transport, most (21.7%) answered "I don't know" and 16.7% "nothing".

As part of this research task, a public opinion poll was conducted in 2022. The main goal was to find out the opinions of Bratislava residents on the introduction of a parking policy, which was launched in February 2022. The survey sample consisted of two groups: residents living with an established parking policy and residents living without aby parking regulation. One third of drivers could find a parking place more easily after the introduction of parking regulations. It remained the same for another third. More than half (55%) of the respondents consider the annual fee reasonable. One third think it's too much. Up to 51% recommend introducing regulated parking throughout Bratislava. Less than a third is against such a policy.

Among drivers who do not have regulated parking, one third support the introduction of regulated parking. Less than a third is against it. Up to two-thirds of drivers expect residents to be prioritized by the parking policy. About half of the people demand more vacancies. Two thirds of drivers think that parking spaces should be counstructed first, and then parking fees should be charged. Less than a quarter of people (23%) think that the fee should be 5 € per month. Another quarter (24%) has no problem even with the amount of 10 € per month. On the contrary, 28% of drivers think that parking should be free.

The regulation of and charging for parking are unpopular topics for politicians. They are afraid of the adverse reactions of the inhabitants and fear that they will not be re-elected. However, experience shows that if the process and implementation of regulated parking are well managed, citizens will appreciate its benefits. People will begin to value public space more and transform it into a space for all residents, not just car owners.

It is recommended that cities adopt a parking methodology that describes specific strategies and steps to help cities prepare and implement regulated parking. The proposed methodology contains political decisions, an analysis of the current state of a regulated parking analysis of the needs and goals of the regional government, the participatory process and public communication, a pilot project, legislation, implementation, monitoring, and an evaluation.

REFERENCES

Bozanic, D. - Tešić, D. - Marinković, D. - Milić, A. (2021). *Modeling of neuro-fuzzy system as a support in decision-making processes.* Reports in Mechanical Engineering, 2(1), 222-234.

Cho, S., & Tóth, C. (2022). *Pave-Ut—Hungarian environmental load application.* Acta Technica Jaurinensis. Available at: https://doi.org/10.14513/actatechjaur.00660

Citizen Cycling Initiative Banská Bystrica. (2013). *Car, bicycle or bus? (Plus 1 daily)* Available at: https://www1.pluska.sk/zaujimavosti/auto-bicykel-autobus-mozno-vas-rozhodne-tato-fotka

Citizen Cycling Initiative Banská Bystrica. (2018). *Comparison of space requirements for static transport for different modes of transport.*

Bajracharya, A. (2013). *Private car and public transportation: dynamics of the modal share. Urban Transport.*

Barter, P. A. (2015). *A parking policy typology for clearer thinking on parking reform.* International Journal of Urban Sciences .

Enviroportál. (2018). *Land occupation by transport infrastructure.* Available at: https://www.enviroportal.sk/indicator/detail?id=941

European Environment Agency. (2021). *Climate change mitigation.* Available at: https://www.eea.europa.eu/themes/climate

European Environment Agency. (2021). *Air pollution.* Available at: https://www.eea.europa.eu/themes/air

European Environment Agency. (2021). *Environment and health.* Available at: https://www.eea.europa.eu/themes/human

European Environment Agency. (2021). *Industry releases thousands of different chemicals into the environment.* Available at: https://www.eea.europa.eu/themes/industry

European Environment Agency. (2021). *Land use*. Available at: https://www.eea.europa.eu/themes/landuse

European Environment Agency. (2021). *Noise*. Available at: https://www.eea.europa.eu/themes/human/noise

European Environment Agency. (2021). *Progress in energy conservation and renewable energy sources is determinant for the transition towards a prosperous, sustainable and climate-compatible European economy.* Available at: https://www.eea.europa.eu/themes/energy

European Environment Agency. (2021). *Transport.* Available at: https://www.eea.europa.eu/themes/transport/intro

Feeney, B. P. & Feeney, B. P. (1989). *A review of the impact of parking policy measures on travel demand.* Transportation Planning and Technology.

Feik, M. (2021). *World of Transportation.* Available at: Analysis of economic impacts of the introduction of parking policy in the Capital City of Slovak republic Bratislava. Available at: http://www.svetdopravy.sk/analyza-ekonomickych-dopadov-zavedenia-parkovacej-politiky-v-hlavnom-meste-sr-bratislava/

Golias, J. - Yannis, G. - Harvatis, M. (2010). *Off-Street Parking Choice Sensitivity.* Transportation Planning and Technology.

Gössling, S. - Humpe, A. - Hologa, R. - Riach, N. - Freytag, T. (2022). *Parking violations as an economic gamble for public space.* Transport Policy.

Klein, N. J., & Smart, M. J. (2017). *Millennials and car ownership*: Less money, fewer cars. Transport Policy.

Laughlin, J. (2018). *Cities around the world have figured out how to ease congestion.* Here are five fixes for Philly. Available at: https://www.inquirer.com/transportation/inq/traffic-philadelphia-center-city-bike-lanes-subway-bus-transit-solutions-20190129.html

Litman, T. (2008). *Parking Management, Strategies, Evaluation and Planning.* Victoria Transport Policy Institute.

Litman, T. (2008). *Parking Management, Strategies, Evaluation and Planning.* Victoria Transport Policy Institute.

Melosi. (2019). *The Automobile and the Environment in American History.* Available at: http://www.autolife.umd.umich.edu/Environment/E_Overview/E_Overview.htm

Ministry of the Environment of the Slovak Republic. (2001). *National Climate Change Report.*

Ministry of the Interior of the Slovak Republic. (2020). *Number of registered cars.* Available at: https://www.minv.sk/?celkovy-pocet-evidovanych-vozidiel-v-sr

National Council of Slovak Republic. (2009). *Act 8/2009 on road traffic.* Available at: https://www.zakonypreludi.sk/zz/2009-8

National Bank of Slovakia. (2021). *Alternative forms of mobility help reduce emissions, but they are still growing.* Available at: https://www.nbs.sk/sk/informacie-pre-media/tlacove-spravy/spravy-vseobecne/detail-tlacovej-spravy/_europsky-svetovy-den-bez-aut-alternativne-formy-mobility-pomahaju-znizit-emisie

National Football Stadium. (2022). *National Football Stadium.* Available at: https://www.narodnyfutbalovystadion.sk/

Nobis, C. (2003). *The impact of car-free housing districts on mobility behaviour - case study.* Transactions on Ecology and the Environment vol 67.

Office for Standardization, Metrology and Testing of the Slovak Republic. (2014). L*ocal road design.*

Petrović, N. J. (2022). *A comparative analysis of road and rail freight transport through the Republic of Serbia from the aspect of external costs.* Available at: Acta Technica Jaurinensis: https://doi.org/10.14513/actatechjaur.00655

Shen, T. - Hong, Y. - Thompson, M. M. - Liu, J. (2020). *How does parking availability interplay with the land use and affect traffic congestion in urban areas?* The case study of Xi'an, China. Sustainable Cities and Society.

Slovak National Council. (2009). *Road Traffic Act 8/2009* Z. z. Bratislava.

Sándor, Z. (2020). *Possible Traffic Safety Effects of the Implementation of Section Control in Hungary.* Acta Technica Jaurinensis.

Statista. (2017). *Number of registered passenger cars in Europe (EU-28) from 1990 to 2017.* Available at: https://www.statista.com/statistics/452447/europe-eu-28-number-of-registered-passenger-cars/

Statista. (2017). *Number of registered passenger cars in Europe (EU-28) from 1990 to 2017.* Available at: https://www.statista.com/statistics/452447/europe-eu-28-number-of-registered-passenger-cars/.

Statista Research Department. (2017). *Annual TV and print advertising spending of top 20 car brands in select EU countries in 2017.* Available at: https://www.statista.com/statistics/936356/eu-top-20-car-brand-tv-print-spend/

Statistical Office of the Slovak Republic. (2020). *Statistical Yearbook of the Slovak Republic. Bratislava:* Statistical Office of the Slovak Republic.

Statistical Office of the Slovak Republic. (2020). *Statistical Yearbook of the Slovak Republic. Bratislava:* Statistical Office of the Slovak Republic.

Susilo, Y. - Reimal, T. - Cats, O. (2017). *The prospects of fare-free public transport: Evidence from Tallinn.* Transportation.

Van Nes, A. (2021). *Measuring The Urban Private-public Interface.* Sustainable City 2021.

Volkswagen Slovakia. (2019). *Annual Report Volkswagen Slovakia 2019.* Available at: https://sk.volkswagen.sk/content/dam/companies/sk_vw_slovakia/podnik/vyrocne_spravy/Vyrocna_sprava_2019.pdf

sciendo
Slovak Journal of Civil Engineering
Vol. 30, 2022, No. 3, 53 – 64
DOI: 10.2478/sjce-2022-0021

WORKABILITY AND STRENGTH CHARACTERISTICS OF ALKALI-ACTIVATED FLY ASH/GGBS CONCRETE ACTIVATED WITH NEUTRAL GRADE Na_2SiO_3 FOR VARIOUS BINDER CONTENTS AND THE RATIO OF THE LIQUID/BINDER

GUGULOTHU VIKAS PAUL[1*], T. D. GUNNESWARA RAO[2]

Abstract

Alkali-activated fly ash/GGBS concrete (AAFGC) is a new blended concrete that has been studied by many researchers due to its environmental advantages and better technological characteristics. However, the effect of various factors on AAFGC fresh and hardened properties has not yet been thoroughly studied. The literature mainly describes the combination of NaOH and Na2SiO3 as an activator for the AAFGC's activation, but alkali-activated GGBS concrete (AAGC) prepared with this activator solution is less workable due to its rapid setting behaviour. In this study, AAFGC was prepared using neutral grade liquid Na2SiO3 with a SiO2/Na2O ratio of 2.92. An experimental program was performed for fly ash-GGBS combinations (100-0, 50-50, 0-100), solution/binder ratios (0.6, 0.65, 0.7) and binder contents (300, 400 and 500 kg/m3) to evaluate the workability and the compressive and tensile strength of AAFGC. The results of this study show that a water glass of 2.92 silica modulus used as an activator to prepare AAFGC under ambient curing is very useful in the construction industry.

Address

[1] Dept. of Civil Engineering, Christu Jyothi Institute of Technology & Sciences, Jangaon, Telangana, India.
[2] Dept. of Civil Engineering, National Institute of Technology, Warangal, India.

[*] ***Corresponding author:*** tdgtdg@gmail.com

Key words

- Alkali-activated fly ash/GGBS concrete,
- Neutral grade liquid Na_2SiO_3,
- Initial and final setting time,
- Workability,
- Tensile strength.

1 INTRODUCTION

After water, concrete is the most widely-used material in the world, and its use increases with urbanization. The main problem in the cement industry is that the manufacturing process of ordinary Portland cement (OPC) emits large amounts of carbon dioxide (CO_2) into the atmosphere. Cement CO_2 emissions contribute to 90% of the global CO_2 emissions by industrial processes (Xi and Davis, 2016), and OPC total industrial emissions account for about 8% of the CO_2 emissions worldwide [Le and Andrew, 2016; Le and Andrew, 2017; Andrew, 2018). Attempts have been made to produce alternatives to cement, such as cement-less concrete. Alkali-activated materials are one of those alternative binders in which cement can be substituted by fly ash and GGBS that are obtained during the production of coal and iron. Research on the development of alkaline-activated materials has aroused great interest for the scientific community over the last twenty years, as these products are expected to become a sustainable alternative to Portland cement binders (Provis, 2014). An alkali-activated concrete is formed when supplementary cementitious materials, such as fly ash, GGBS, rice husk ash, metakaolin, etc., are activated with an alkaline solution (Midhun et al., 2018; Wongpa et al., 2010; Venu and Rao, 2017). Arivalagan (2014) concluded that GGBS can be used as an alternative to cement as it reduces the use of cement and construction costs. The alkali activation of fly ash binder with an activator prepared with sodium hydroxide and liquid Na_2SiO_3, which requires a high concentration of NaOH and heat curing, has been proposed to increase the initial age strength of alkali-activated fly ash concrete (AAFC) (Mustafa et al., 2011). The alkali activation of a GGBS binder can produce high strength AAGC without oven curing, but the main problem with GGBS is the rapid setting behavior of the concrete, which results in low workability. AAFGC has exhibited attractive technical properties, and its engineering performance can be optimized by changing the fly ash/GGBS proportions.

Alkali-activated concrete, which is also called organic polymer or geopolymer concrete, can reduce greenhouse gas emissions in the concrete industry by 80 % (Davidovits, 1994; Daniel et al., 2006). The term 'geopolymer' was first used by the French scientist Davidovits Joseph, who applied it to solids produced from the reaction of aluminosilicate powder and an alkaline solution (Joseph, 1999). Since V.D. Glukhovsky developed alkali-activated slag cement and concrete in the USSR in 1957, the understanding of the alkali activation process mechanism has progressed considerably (Glukhovsky, 1959), but there are many challenges that need to be overcome. It was reported that AAFC has great physical properties, such as greater initial strength, less shrinkage, and high freeze-thaw resistance to sulfate attack and corrosion (Davidovits et al., 1990). For alkali-activated cement, it has been noted that a large amount of SiO_2 and Al_2O_3 in calcined materials is as good as the source material. Alkali hydroxide (MOH), weak acid non-silicic salts (M_2CO_3, M_2S, MF), and $M_2O.(n)SiO_2$-type silicic salts, and also their combinations, can be the most effective activating solution, where M represents alkali metals such as Na, K, and Li (Richardson et al, 1994; Wang et al., 1995). Ambient temperature curing has been performed for fly ash-based geopolymer mortars with the addition of calcium oxide and calcium hydroxide due to the accumulation of calcium compounds, which increase their mechanical properties (Temuujin et al., 2009). Mallikarjuna Rao and Gunneswara Rao, (2015) reported that for an alkali-activated GGBS paste made using alkaline solutions of 8M and 16M NaOH, the final setting time values are 40 minutes and 60 minutes respectively. It is also known that slag reactions produce small particles. Particles larger than 20 μm demonstrate slow reactions, but particles < 2 μm completely react in cement and alkali activation systems for twenty-four hours (Shi et al., 2005). Obviously, when slag is used for geopolymerization, similar to the OPC mixing, the strength development profile is controlled by a thorough grain size distribution control (Wan et al., 2004). It has been stated in the literature that the development of strength is due to minerals such as anorthite-sodian, albite, and analbite (Thunuguntla and Rao, 2018).

In studying the fresh and hardened properties of concrete, the activating solution used in AAFGC also plays a significant role. Generally, ordinary Portland cement, sodium hydroxide, Na_2SO_4, Na_2CO_3, and Na_2SiO_3 are used as activators in geopolymer concrete. Many researchers believe that the liquid Na_2SiO_3 is the best activating solution (Glukhovsky, 1980; Malolepszy and Petri, 1986; Douglas et al., 1991; Wang et al., 1994). Landrou et al., (2016) suggests that using Na_2SiO_3 as a dispersant in order to obtain good workability can significantly reduce the paste's yield stress. Bakharev et al., (1999) stated that, compared to Na_2CO_3 and NaOH activators, liquid Na_2SiO_3 is the best activator to impart compressive strength to AAGC. Activation with the liquid Na_2SiO_3 single activator can achieve greater compressive strength compared to NaOH; the low strength of NaOH-activated GGBS-based geopolymer pastes can be explained by these pastes' higher porosity when compared to alkali-activated slag pastes prepared with Na_2SiO_3. Wang et al., (1994) noted that a water glass with silica modulus (M_s) in the 1 to 1.5 range are the best formulations for developing AAGC with a good strength. In contrast, based on low-calcium AAFC tests, Hardjito et al., (2004) stated that the combined solution of NaOH and Na_2SiO_3 can be a good activator, as the high concentration of NaOH and the curing temperature can increase the compressive strength of concrete. However, alkali-activated slag pastes set in 15 minutes, as many researchers have proven experimentally (Jimenez et al., 1999; Jannie and Deventer, 2002; Caijun and Yinyuz, 1989; Wang et al., 1995). This leads to a rapid loss of AAGC workability, thereby preventing its practical application. Improving the use of alkali-activated slag pastes as building materials is needed to solve rapid setting and risk management problems.

The reason for the rapid setting behaviour of alkali-activated slag pastes is the initial rapid formation of C-S-H gel, which leads to the paste hardening. Shi and Day et al., (1995) studied AASC prepared with various activating solutions using an isothermal conduction calorimetry. They found two subsequent signals during the pre-induction stage in slag pastes prepared with sodium silicate. The first is due to the dissolution of the slag and the second is due to the primary C-S-H gel being formed as a result of the $[SiO_4]^{4-}$ ions present in the solution. As the silica modulus of water glass increases, the latter signal intensifies. The formation of the initial C-S-H gel was also observed in water glass alkali-activated slag pastes in rheological tests with a constant shear rate (Palacios et al., 2008). After the initial increase, the shear is reduced and stabilized, attendant upon the paste's deflocculation, which is due to the gel breakdown of the initial C-S-H flocks. The extension of the mixing time from 3 minutes to 10 minutes has also shown that the initial setting time was retarded by 40 minutes and the final setting time by more than 4 hours. The initial and final setting times were also delayed during the 30 minute mixing time (Palacios and Puertas, 2011) . It has recently been shown that the intensity and timing of these signals of rheology at a constant shear rate in alkali-activated fly ash/GGBS pastes prepared with water glass depend on the concentration of the Na_2O and the SiO_2/Na_2O ratio of the activator used. The higher the latter and, thus the higher the silicon content in the activator, the earlier and stronger the signal (Puertas et al., 2014). It is clear that the rheology is affected by this rapid setting and, accordingly, the on site paste and concrete casting. It has been shown in the literature that the reason for this behaviour can be understood and that a solution for this problem can be found in the rheological studies (Palacios, 2006; Palacios et al., 2008). However, some studies have focused on the rheology of slag-based geopolymer systems prepared using liquid Na_2SiO_3.

The most important characteristic of Na_2SiO_3 is the silica modulus, i.e., the SiO_2/Na_2O ratio. Commercially available liquid Na_2SiO_3 has Ms values between 1.6 and 3.85. Water glass is impractical and has less stability outside this range. The rate of geopolymer polymerization increases with the increase in the SiO_2/Na_2O ratio (Xu and Van Deventer, 2000). Krizan et al., (2002) has shown that the sodium content and the SiO_2 to Na_2O ratio of water glass affect the hydration process of alkali-activated slag. It was reported that the use of water glass with M_s in the range of 1-2 provides the best results for AAGC mixes (Tailing and Brandstetr, 1989). The recommended silica modulus ranges from 1 to 1.5 in the literature, and the amount of Na_2O used was 3 - 5.5% when liquid Na_2SiO_3 is used as the activating solution, but in other works, Na_2O of 6.1% was proposed (Wang et al., 1994; Wang et al., 1995). The binder is activated by the alkali, and the silica gel is produced by silica SiO_2. This shows that the compressive strength improves with the increase in the silica for a fixed Na_2O content, which indicates that the high value of M_s results in greater compressive strength. At a M_s value of 3.1, high strength was achieved (Bondar et al., 2011). Liquid Na_2SiO_3activating solutions can be handled safely for a silica-sodium oxide ratio > 1.5 (Elmore, 2004).

The pH value is one of the most significant factors to determine the stability of high M_s water glass (Shi et al., 2006). Due to the large contribution of silica gel formation to the strength of the geopolymerization, the relation between M_s and Na_2O was observed. The effect of alkaline activation is the same for constant Na_2O, and the larger the modulus, the greater the silica gel formation and the higher the compressive strength. For a fixed Na_2SiO_3 solid content, the lower the M_s value, the greater the Na_2O content and the higher the effect of activation resulting in a low amount of silica gel. These competitive effects result in an optimum value of M_s, which differs depending on the binding materials and curing conditions. For an insufficient alkaline activation resulting in a slow activation of alumino-silicate, a low M_s value is desirable; otherwise, a higher value of M_s is desirable.

It is advantageous to use a liquid Na_2SiO_3single solution as an activator rather than a combination of Na_2SiO_3 and NaOH. Gugulothu Vikas and Gunneswara Rao (2020) reported that using neutral grade liquid Na_2SiO_3 as an activating solution for AAGC leads to an increase in the setting time, thereby solving the problem of the quick setting behaviour of slag concrete. Previous studies have suggested that a combination of NaOH and Na_2SiO_3 activator could be mixed 24 hours before casting. However, when the Na_2SiO_3 solution alone is used as an AAGC activator, that is not necessary. In addition, precautions are needed to handle NaOH solutions as they release heat, but no heat is released from water glass single solutions. Also, the cost of a water glass activator is much less than NaOH. It is obvious from the literature that increasing the SiO_2/Na_2O ratio of the activator increases the workability and strength characteristics of AAFGC. Therefore, in the present investigation, tests were conducted on AAFGC produced using liquid Na_2SiO_3 of a high M_s 2.92 (neutral grade) to improve the AAFGC workability. No other chemical additives were added to the AAFGC preparation to increase the slump or the concrete's strength.

The reports available on AAFGC indicate that the design factors, such as the binder content and the ratio of the liquid/binder, can have a significant impact on the workability and strength of the concrete. The liquid/binder ratio effect on AAFGC is the same as the water/cement ratio in traditional OPC (Bondar, 2018). Cheng et al. (1999) concluded that AAGC is formed with a similar mechanical strength and durability as traditional OPC by changing the design factors. Thus, the important design factors studied in this work are the amount of the binder and the ratio of the liquid/binder, because the effect of these factors on conventional OPC has been well studied, but the AAFGC activated with water glass solutions has not been systematically studied. The results of the study showed that the setting time of AAGC was increased by three hours using a neutral grade liquid Na_2SiO_3 activating solution of silica modulus 2.92, which resulted in a good workability and high strengths for AAGC.

2 SIGNIFICANCE OF THE RESEARCH

Slag-based alkali-activated concrete is not suitable for construction because of its fast-setting nature. The literature shows that the liquid Na_2SiO_3 of a high M_s value leads to better properties of AAFGC. It is therefore necessary to study the effect of the high silica modulus of liquid Na_2SiO_3 activator on the workability and strength properties of the AAFGC. The present study deals with the normal consistency, and the initial and final setting time of alkali-activated fly ash/GGBS paste along with the workability, compressive and tensile strength of AAFGC activated with neutral grade liquid Na_2SiO_3 of silica modulus 2.92 obtained from a sodium silicate production company. The workability and strength properties of the AAFGC for various binder contents and liquid/binder ratios were studied in the current work; as a result, researchers will be able to identify the behaviour of AAFGC activated by neutral grade liquid Na_2SiO_3.

3 EXPERIMENTAL PROGRAM

Firstly, the normal consistency (P) and the initial and final setting time tests are performed on alkali-activated fly ash/GGBS paste; secondly, slump, compressive strength, split tensile strength, and flexural strength tests are performed on the concrete for determining the workability and mechanical properties of AAFGC. The normal consistency of the cement is obtained from Vicat's apparatus based on IS: 4031-part 4 (1988). The same procedure was adopted for determining the consistency value of the alkali-activated fly ash/GGBS paste. To prepare alkali-activated paste at a standard consistency, an activating solution was used instead of water. Based on IS 4031-part 5 (1988), IST and FST for the alkali-activated paste were tested using Vicat's apparatus based on IS 1199 (1959) by considering the binder proportion as 500 g and 0.85 times the value of the normal consistency.

To determine the AAFGC's workability, the slump test was performed based on IS 1199 (1959) with a metal slump mold. The slump value was reported by measuring the difference between the height of the mold and the maximum point of the AAFGC. The concrete in the molds was then compacted and vibrated. Depending on the concrete slump, the vibration time is approximately ten to thirty seconds. A 2000kN Tinius-Olsen testing machine was used to test the compressive and tensile strength for the adopted AAFGC mixes based on IS: 516 (1959).

The binder content and the ratio of liquid/binder effects on the fresh and hardened properties of the AAFGC were also investigated. For the solution/binder ratios (0.6, 0.65, and 0.7) and binder quantities (300, 400 and 500 kg/m^3), a test program was performed on the AAFGC activated by neutral grade liquid $Na_2SiO_3$with a silica modulus 2.92. The slump, compressive and tensile strengths were measured for each AAFGC mix. The role of aggregates in AAFGC is considered to be similar to traditional OPC concrete. Since there is no standard design methodology available for AAFGC, the design methodology implemented is almost similar to traditional OPC concrete. By treating the aggregate medium as inert, the FA/CA ratio of the aggregate is considered to be 0.45/0.55 as the maximum dry density of the mixed aggregates is reached at this point.

4 MATERIALS

4.1 Binder

Class-F fly ash and slag were used as binder materials in this study. The fly ash used was procured from the Ramagundam thermal power plant, India, and the slag used was obtained from JSW

Cements, Hyderabad, India. Fly ash and GGBS have specific gravity values of 2.17 and 2.93 and a fineness of 380 m^2/kg and 426 m^2/kg respectively. The chemical composition of the fly ash and slag is shown in Table 1.

Tab. 1 *Chemical composition of fly ash and slag (% by mass)*

Chemical composition	Fly ash	GGBS
SiO_2	60.1	34.07
Al_2O_3	26.54	20.1
Fe_2O_3	4.24	0.81
SO_3	0.36	0.91
CaO	4.01	32.7
MgO	1.26	7.88
Na_2O	0.23	NIL
Loss on ignition	0.87	NIL

4.2 Aggregates

The fine aggregate used to prepare AAFGC is clean dry river sand. It was sieved by a 4.75 mm sieve to remove all the pebbles. The dry specific gravity of the saturated surface of the fine aggregate is 2.68 and conforms to IS 383 (1970) zone II standards. Crushed granite of a maximum 16 mm size was used as coarse aggregate and with a 2.72 specific gravity value. The fine and coarse aggregates had fineness modulus values of 2.73 and 6.33 respectively. Combined aggregate grading was used to meet the standard combined grading curve recommended by the DIN 1045 (1988) standard as shown in Figure 1.

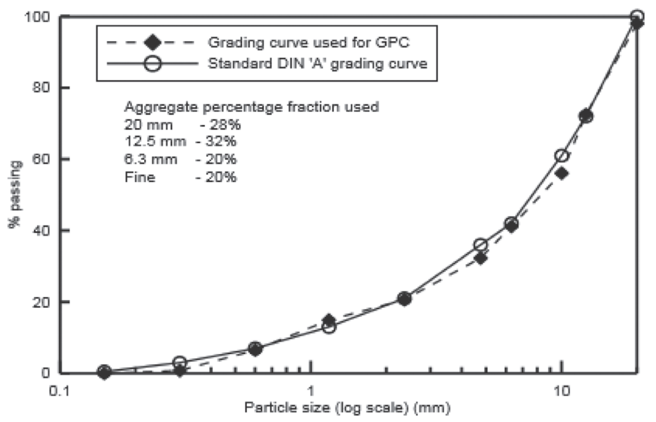

Fig. 1 *Combined aggregate grading curve*

4.3 Activator

The grades of industrial Na_2SiO_3 solution were divided based on their SiO_2:Na_2O ratio i.e., a silica modulus (M_s) that ranges between 2:1 and 3.75:1. Grades with M_s value >2.85 are defined as neutral grade and grades with a M_s value <2.85 are defined as alkaline. A neutral grade Na_2SiO_3 of M_s 2.92 was used as an activating solution in the present study with 28.98% SiO_2, 9.92% Na_2O by weight and pH 12.9, which was obtained from Kiran Global Limited, Chennai, India.

4.4 Casting procedure of the AAFGC samples

The binder, fine aggregates, and coarse aggregates were initially dry mixed for two to three minutes. The activator was then added in the dry mixture, and the mixture was stirred for 5 to 7 minutes until a uniform mixture was achieved. The slump values were then noted followed by the casting of the concrete specimens and the compaction and vibration of the fresh concrete. The concrete cube specimens were cast using steel molds of dimensions of 100 mm x 100 mm x 100 mm. To determine the compressive strengths for 7, 14 and 28 days, 9 cubes were molded to perform 28-day split tensile strength and flexural strength tests; 3 cylinders (150 mm x 300 mm) and 3 prisms (100 mm x 100 mm x 500 mm) were molded for each concrete mix. Thus, 27 concrete mixes (3 Fly ash/GGBS x 3 binder x 3 liquid/binder ratios) of 243 cubes, 81 cylinders and 81 prisms were cast to perform the compressive strength, split tensile strength and flexural strength tests respectively. After 24 hours of casting time, the specimens were demolded and placed at room temperature (27 ± 2°C, 70% relative humidity) till the testing day. The parameters considered in the current investigation were: 1) percentage of slag substituted by fly ash (0, 50, 100); 2) binder content (300, 400 and 500 kg/m^3) and 3) liquid/binder ratio (0.6, 0.65 and 0.7). Since there is no standard mix design procedure for geopolymer concrete, the mix proportions were calculated according to the mix design steps employed in the literature (Vikas and Rao, 2021). The AAFGC mix proportions adopted in this study are shown in Table 2.

Tab. 2 *AAFGC Mix proportions*

B	A/B	FA	CA	A	MP
300	0.6	909	1111	180	1: 3.03: 3.7: 0.6
300	0.65	902.25	1102.7	195	1: 3: 3.67: 0.65
300	0.7	895.5	1094.5	210	1: 2.9: 3.64: 0.7
400	0.6	837	1023	240	1: 2.09: 2.55: 0.6
400	0.65	828	1012	260	1: 2.07: 2.53: 0.65
400	0.7	819	1001	280	1: 2.04: 2.5: 0.7
500	0.6	765	935	300	1: 1.53: 1.87: 0.6
500	0.65	753.75	921.2	325	1: 1.5: 1.84: 0.65
500	0.7	742.5	907.5	350	1: 1.48: 1.81: 0.7

Where: B- Amount of binder (kg/m^3), A/B- Ratio of Solution/binder, FA - Fine aggregate (kg/m^3), CA - Coarse aggregate (kg/m^3), A - Activator solution (kg/m^3), Mix proportions (MP) - B: FA: CA: A

5 RESULTS AND DISCUSSION

5.1 Standard consistency and setting time

The standard consistency and setting time values for the alkali-activated fly ash/GGBS paste are presented in Table 3. The range of the consistency was observed to vary from 36% to 49%. The high consistency value could be because of the sticky nature of the activator due to the low water content in the water glass. The normal consistency of the alkali-activated paste mix prepared with fly ash alone was observed to require a lower amount of activating solution than the alkali-activated paste mix prepared with GGBS alone. The increase in the standard consistency value was observed with the rise in the slag content. This behavior is due to the spherical shape of the fly ash particles and less internal friction, which leads to the Vicat's plunger-free movement for the low activating solution content. In contrast, GGBS particles have a straight, flaky and elongated shape with a sharp-edged angularity and a rough surface texture, which has a greater internal friction when compared with fly ash particles; thus, more solution is required to obtain a normal consistency. It is clear that the percentage of slag in the binder used has an impact on the normal consistency of alkali-activated fly ash/GGBS paste.

Tab. 3 *Fresh properties of alkali-activated fly ash/GGBS paste*

GGBS %	Consistency (%)	Initial setting time (min)	Final setting time (min)
0	36	1210	1900
50	44	420	780
100	49	125	205

The method used for studying the alkali-activated fly ash/GGBS paste setting times was the same as the method applied for determining the IST and FST of the cement. The IST values varied from 1210-125 minutes, and the FST values varied from 1900-205 minutes respectively. The slag was observed to react more easily with the activator than the fly ash. The difference in the chemical composition between GGBS and fly ash may have reduced the setting times of the alkali-activated slag paste. Compared to the fly ash, the setting aspects of the slag with the solution are faster. Thus, in order to develop high initial strength alkali-activated material, slag is a better binder than fly ash. The range of the IST value is 1210 to 420 minutes, and the FST value is from 1900 to 780 minutes when the slag is replaced by 50%. Therefore, an appropriate neutral grade Na_2SiO_3 activated fly ash: GGBS proportion can be recommended for a required setting time value.

Fig. 2 *Alkali-activated fly ash/GGBS paste*

The alkali-activated fly ash/GGBS paste is shown in Fig.1. As the fly ash-based alkali-activated paste has a consistency of 36%, the amount of liquid required to calculate the IST and FST was 0.85 P (i.e., 0.85 x 36 = 30.6 %), whereas for the alkali-activated slag paste, as the consistency was 49%, the amount of solution required to calculate IST and FST was 0.85 P (i.e., 0.85 x 49= 41.6 %). For the alkali-activated slag paste, the initial and final setting times were recorded to be 125±5 minutes and 205±5 minutes, respectively. Generally, the required initial setting time for the cement construction is 30 to 45 minutes, and the final setting time is 10 hours, but for the alkali-activated slag paste activated with the regular alkaline solution ($NaOH+Na_2SiO_3$), it is clear from the literature that the final setting time is less than 40 minutes. In this study, the AAFGC was observed to have IST and FST values of about 125 minutes and 205 minutes respectively. Thus, using neutral grade liquid Na_2SiO_3 of silica modulus 2.92 as an activator for AAFGC is advantageous, as it increased the final setting time of the alkali-activated slag paste by about three hours. This indicates that this activator provides a sufficient initial setting time and final setting time and is useful for working with green concrete. The acceleration effect on the IST and FST has been reported to be pronounced by increasing the concentration of the activating solution in GGBS [27]; similar effects were observed in the current investigation at the time of the casting and curing of the specimens.

5.2 Workability

The workability of the AAFGC mix is influenced by the fly ash/GGBS percentage, solution/binder ratio, and binder content. Tests were carried out on various AAFGC mixes for different fly ash/GGBS binder proportions, binder contents and solution/binder ratios; the slump over the time values is noted. The reduction in the value of the slump with the rise in the slag percentage in the binder material is because of the reduction in the setting time value of AAFGC. Chindaprasirt et al., (2007) observed a similar behaviour in the workability of alkali-activated fly ash/GGBS concrete. The workability values were higher compared to the traditional OPC concrete. The AAFGC high slump values are due to the formation of the silicates as it gives an adhesive property to AAFGC. The workability of the concrete was studied from the slump values that are noted at 30, 60, 90 and 120 minutes for all the AAFGC mixes as shown in Table 4. For the 100 % fly ash concrete mix, the range of the slump from the 300-0.6 mix to the 500-0.7 mix after 30, 60 and 90 minutes is 60 to 118 mm, 34 to 82 mm and 18 to 65 mm. Similarly, for the 50% GGBS concrete mix, the range of the slump from the 300-0.6 mix to the 500-0.7 mix after 30, 60 and 90 minutes is 52 to 112 mm, 28 to 75 mm and 16 to 58 mm. In the same way, for the 100% GGBS concrete mix, the range of the slump from the 300-0.6 mix to the 500-0.7 mix after 30, 60 and 90 minutes is 40 to 96 mm, 22 to 65 mm and 10 to 52 mm. The value of the slump for all the mixes were noted as zero at 120 minutes from the mixing time of the concrete. In the slump test, the fresh concrete was observed to be shrinking very slowly.

Table 4 shows the values of the slump over time of AAFGC for the 0.6, 0.65, 0.7 liquid/binder ratios. The rise in the amount of the binder and the ratio of liquid/binder improved the paste content, which ultimately increases workability without the need for a superplasticizer. The increase in the slump is because of the increased setting time of the alkali-activated paste activated by the neutral grade Na_2SiO_3. Therefore, with the rise in the amount of binder and the ratio of liquid/binder, the workability is observed to be increasing.

In general, the setting time that affects workability is dependent on the precursors and composition of the activating solution. The rheological behaviour has been reported to affect the type of activator used (Zivica, 2007). The regular process of alkali-activation ($NaOH + Na_2SiO_3$) exhibits strong alkalinity, resulting in

Tab. 4 *Slump over time of AAFGC*

Fly ash:GGBS	Binder content (Kg/m^3)	300					400					500				
	Solution/ binder	Slump (mm)					Slump (mm)					Slump (mm)				
		0 min	30 min	60 min	90 min	120 min	0 min	30 min	60 min	90 min	120 min	0 min	30 min	60 min	90 min	120 min
100:0	0.6	118	60	34	18	0	132	72	40	26	0	158	97	65	46	0
	0.65	134	68	40	24	0	162	84	57	38	0	183	105	78	60	0
	0.7	157	75	45	26	0	173	88	62	43	0	187	118	82	65	0
50:50	0.6	108	52	28	16	0	125	66	38	23	0	132	80	52	38	0
	0.65	129	58	33	21	0	156	78	48	35	0	171	102	68	52	0
	0.7	153	66	36	23	0	164	82	52	40	0	180	112	75	58	0
0:100	0.6	102	40	22	10	0	120	53	32	19	0	126	64	43	26	0
	0.65	119	46	28	16	0	145	68	41	28	0	165	92	54	40	0
	0.7	144	54	32	18	0	156	72	45	33	0	175	96	65	52	0

the release of silicon (Si) and calcium (Ca) from slag, which are diffused from the outer layer of the reaction products and quickly formed over the particles that did not react. The conditions of the solution increase the process of activation and also the solubility of Si and Ca formed due to OH- stimulates the slag dissolution. The slag grains are dissolved in less time, which leads to a lower initial alkali-activated paste setting time. However, the performance of the alkali-activated fly ash-slag paste is peculiar when the activator used is a commercial liquid Na_2SiO_3 solution. When the GGBS particles come into contact with the sodium silicate solution, they are surrounded with a thin layer of primary CSH gel due to the interactions of the silicate ions in the activator and Ca^{2+} ions in the GGBS (Huanhai et al., 1993; Rodriguez-Puerta et al., 2014). The GGBS particles are then bonded by Vander Waals forces. These flocs were partly divided at the beginning of the rheological tests, but the rapid and greater precipitation of the initial CSH gel continued to produce large flocs. The constant mixing of the samples leads the flocs to break under experimental conditions, indicating a decrease in shear stress. This improves the flowability and the slump. Using water glass as a dispersant was reported to significantly reduce the yield stress of the alkali-activated paste to reach a suitable slump value (Landrou et al., 2016). This is helpful for applications involving building materials because it results in a long time to handle and place the fresh material.

Fig. 3 *Slump of AAFGC*

5.3 Compressive strength of AAFGC

The AAFGC compressive strength values for the various liquid/binder ratios and binder contents for 7, 14 and 28 days are presented in Table 5. The effect of the fly ash/GGBS proportions on the compressive strength of AAFGC is observed to be more than that of the ratio of the solution/binder and the amount of the binder. The percentage increase of GGBS in the binder increased the AAFGC strength, and similar behaviour was reported for the geopolymer mortars (Mallikarjun Rao and Gunneswara Rao, 2015). The increase is because of the high Ca content in the slag. The range of the 28-day AAFGC's compressive strength is 12.9-85.6 MPa. This increase is due to the continued polymerization at room temperature (Patil et al., 2014). There are two possible mechanisms for the hydration reaction: 1) the formation of fly ash and slag polymerization reactions individually, or 2) the formation of fly ash and slag polymerization reactions at the same time (Wardhono et al., 2014). In the separate polymerization process, GGBS was assumed to re-

Tab. 5 *Compressive strength of AAFGC*

Fly ash:GGBS	Binder content (Kg/m³)	300			400			500		
	Solution/binder	Compressive strength (MPa)			Compressive strength (MPa)			Compressive strength (MPa)		
		7 days	14 days	28 days	7 days	14 days	28 days	7 days	14 days	28 days
100:0	0.6	5.97	10.1	13.4	8.57	12.78	17.2	10.98	16.27	20.8
	0.65	5.45	9.39	12.9	6.24	10.39	13.8	7.58	11.64	15.6
	0.7	5.75	9.80	13.2	7.05	11.46	14.9	8.43	12.74	16.7
50:50	0.6	30.9	36.5	42.8	40.54	46.72	54.2	40.95	46.12	52.23
	0.65	30.1	35.8	42.1	34.84	40.49	47.14	40.08	45.40	51.71
	0.7	27.9	33.8	40.2	33.34	39.07	45.8	37.62	43.03	49.57
0:100	0.6	70.6	74.8	76.5	77.63	80.85	82.5	82.26	84.57	85.6
	0.65	67.9	72.5	75.3	76.02	79.43	81.3	76.12	78.85	80.3
	0.7	69.7	73.8	76.2	74.52	78.29	80.3	79.49	82.25	83.5

act first to form a matrix around the fly ash; then the pores are filled by fly ash, which leads to higher compressive strength. Whereas in the second mechanism, both reactions occur at the same time, thereby activating the fly ash at an ambient temperature.

The high strength of the alkali-activated materials contributes to the physical and structural binder properties. Table 5 shows the compressive strength values for the different binder contents, solution/binder ratios, and fly ash/GGBS ratios. There are two reasons for the AAFGC's high strength. Firstly, the rapid hydration reaction occurred because of the heavily loaded gel structure in the high pH region and secondly due to the dense and constant binder aggregate interface (interfacial transition zone), with little difference between this region and the binder area away from the aggregates (Provis et al., 2007). The characteristics of the AAFGC transition area prepared with water glass may be related to many factors such as the refinement of the porosity due to the additional SiO_2 condensation supplied by the water glass, along with the partial reactivity of the siliceous aggregate surfaces with the liquid alkali silicate in order to find extra reactivity products surrounding the aggregates. This provides strong bonds between the macrophases by the reactivity of the products attained by the aggregates, and the mechanical bonding is enhanced by the high degree of roughness of the particles (Lee and Van Deventer., 2007). In addition, the hydration process also depends on the pH value of the activating solution in establishing the hydrated C–S–H product characteristics. This process mainly occurs with pH values greater than 12, which is impossible to achieve for pH values lower than 9.5. A lower value will slow down the activation process even when it occurs. The anion type of activating solution is the key aspect that controls the concrete's setting time, and the strength development is high in pH values of more than 12. These anions can react with soluble ions in GGBS, especially with Ca^{2+} ions forming constant hydration products. The activator was reported to show a better GGBS hydration capacity for a higher pH value (Douglas et al., 1992). The basic pH of the activator is necessary for the hydration ability of the GGBS. The activating solutions with high pH basic values are most effective. The immediate appearance of silicate ions in the system by adding water glass containing these ions reverses the systems prepared with sodium hydroxide and sodium carbonate, which takes time to form the ions needed to improve the hydration of the alkali-activated systems. Therefore, it is clearer that the higher silicate ratio activators are best for chemical bonding as it is the siliceous portion of Si that reacts with the cations. As the pH of the water glass used in the current investigation is 12.9, increased workability and mechanical properties were obtained.

The main factors affecting the degree of hardening and the concrete's ultimate strength are the amount of the binder and the ratio of the liquid/binder. They are interrelated and are not used for the individual computing of the concrete's strength. The AAFGC with a high binder content was observed to consistently have a high compressive strength. The strength depends on the composition of the binder at high concentrations and also on the long-term curing age, which indicates the high degree of the chemical reaction over time, thereby generating strength in the curing period. A lower solution/binder ratio leads to lower strength, but the mix is more difficult to place. The higher quantity of liquid content instead of the solids in the mix results in a decrease in strength due to the decreased contact between the activator and the reacting material. This reduction was found to be due to the capture of a greater amount of contact fluid. The rise in the water glass content limits the contact between the binder particles and water glass, which may be the reason for the reduction in strength. In some cases, for an increase in the ratio of the liquid/binder at a constant amount of binder, an increase in the strength of the concrete was observed. This is due to the existence of a large number of silicates (SiO_2) in the concrete mix, which is the main reason for the gain in strength through the formation of extra N-A-S-H, C-A-S-H or C-S-H gel. This agrees well with Bondar et al., (2011). As the liquid content increases, the silicates and aluminates present in the binder dissolve more. As a result, more polymerization takes place, and a greater strength in the concrete is obtained. An increase in the liquid/binder ratio to a certain level has a negative effect on the strength of all the binder contents, which is in accordance with the regular standards for cement and concrete materials.

Fig. 4 *Failure of AAFGC cubes*

5.4 7 and 14-day compressive strengths as a percentage of 28-day strength

Table 6 shows the rate of the gain in strength in 7 and 14 days in the percentage of the 28-day compressive strength. The AAFGC compressive strength increased with the hydration time, but the initial age strength gain varied for the various fly ash-slag mixes. The rate of gain in compressive strength is also noted to be different for various fly ash-slag proportions. In general, the major contribution of the initial strength gain is due to the slag, but the gain in strength over time was mainly contributed by the fly ash in the binder. The alkali-activated fly ash concrete generally requires oven curing to improve strength in less time; therefore, it does not obtain structural integrity at ambient temperatures, which is helpful for the construction area in the quick removal of formwork from the site. The results show that the AAGC activated by the neutral grade water glass has a high rate of gain in strength in the initial stages than in the later curing stage. The initial stage reactions of AAGC depend on the dissolution and precipitation phenomena, where higher pH kinetics are more rapid compared to the OPC-based diffusion-controlled hydration process that provides greater strength in the early stages. These AAGC features show its ability to respond to emergencies. Therefore, the greater early strength of the AAGC was observed for two reasons (Bernal et al., 2010). Firstly, GGBS has a larger amount of CaO that can be mixed with SiO_4 and AlO_4, which form CSH gel and CASH gel instantly. Secondly, water glass is more effective for early strength than sodium hydroxide or a Na_2SO_4 solution, because the silicate ions produced by the Na_2SiO_3 solution can increase gel precipitation. The aggregates used in the preparation of AAFGC are in a saturated surface condition. If the aggregate is dry, moist, or partly dry, the change in the amount of activator must be taken into account the same as in OPC concrete. Hence, varying the fly ash/GGBS proportions, binder contents, and solution/binder ratio can significantly affect the strength of AAFGC.

5.5 Tensile strength of AAFGC

Understanding the mechanical properties of AAFGC activated by water glass is certainly significant when it comes to using the concrete effectively. Table 7 shows the 28-day split tensile and flexural strengths of AAFGC mixes for different fly ash/GGBS proportions. The results indicate that AAFGC shows good mechanical properties under ambient curing conditions without the need for any heat curing. An increase in the split tensile strength and flexural strength of AAFGC was observed with the increase in slag content in the binder, which is due to the binder activation process. It can be seen that the AAGC provides more strength because of its quick reaction rate. Increasing the binder content significantly increased the tensile and flexural strengths. The range of the split tensile strength for the AAFGC made with 100% fly ash, 50% GGBS, and the 100% GGBS mixes are 1.92–2.3, 2.5-3.85 and 5.8-6.52, respectively. Similarly, the range of flexural strength for the AAFGC made with 100% fly ash, 50% GGBS, and the 100% GGBS mixes are 2.4–4.23, 3.36-5.92 and 7.6-8.6

Tab. 6 *7 and 14-day compressive strengths as a percentage of 28-day strength*

Fly ash: GGBS	Binder content (Kg/m^3)	300			400			500		
	Solution/ binder	Age of concrete as % of 28 days' strength			Age of concrete as % of 28 days' strength			Age of concrete as % of 28 days' strength		
		7-days (%)	14-days (%)	28-days (%)	7-days (%)	14-days (%)	28-days (%)	7-days (%)	14-days (%)	28-days (%)
100:0	0.6	44.6	75.6	100	49.8	74.3	100	52.8	78.2	100
	0.65	42.3	72.8	100	45.2	75.3	100	48.6	74.6	100
	0.7	43.6	74.3	100	47.3	76.9	100	50.5	76.3	100
50:50	0.6	72.2	85.4	100	74.8	86.2	100	78.4	88.3	100
	0.65	71.5	85.1	100	73.9	85.9	100	77.5	87.8	100
	0.7	69.5	84.2	100	72.8	85.3	100	75.9	86.8	100
0:100	0.6	92.4	97.9	100	94.1	98	100	96.1	98.8	100
	0.65	90.3	96.4	100	93.5	97.7	100	94.8	98.2	100
	0.7	91.6	96.9	100	92.8	97.5	100	95.2	98.5	100

Tab. 7 *Split tensile and flexural strength of AAFGC*

Fly ash:GGBS	Binder (Kg/m^3)	300		400		450	
	Solution/Binder ratio	Split tensile strength	Flexural strength	Split tensile strength	Flexural strength	Split tensile strength	Flexural strength
100:0	0.6	2.18	3.21	2.24	3.5	2.3	4.23
	0.65	1.92	2.4	1.98	2.92	2.08	3.75
	0.7	2	3.1	2.12	3.3	2.16	4.1
50:50	0.6	2.64	3.9	3.2	4.8	3.85	5.92
	0.65	2.54	3.74	2.87	4.6	3.59	5.63
	0.7	2.5	3.36	2.78	4.3	3.2	5.24
0:100	0.6	6.73	8.26	6.6	8.34	6.52	8.6
	0.65	5.8	7.6	5.94	7.8	6.04	8.1
	0.7	6.32	7.98	6.38	8.1	6.48	8.3

respectively. However, it is well known that there is a relationship between the tensile and compressive strength of concrete. The higher the compressive strength, the higher the tensile strength of the concrete. Deb et al., (2014) reported that fly ash-based, alkali-activated concrete substituted with up to 20% GGBS in the binder resulted in the improvement of the split tensile strength. The reactions in high percentage GGBS binders are much higher than in low percentage GGBS binders. Conversely, the GGBS partially dissolves and contributes to the reaction. Thus, the increase in the GGBS percentage in the binder refines the AAFGC pore structure, thereby improving the tensile strength of the concrete. Another factor which improves the tensile strength is the pH of the activator. It is one of the major factors in the hydration process determining the formation characteristics of the C-S-H hydration product. The CSH hydration product formed depends on the type of silicate activator affected by the pH solution. The results have revealed that the AAFGC mixes increased the mechanical properties of the concrete at an ambient temperature to be able to cure itself without any heat curing. This is due to the strong bonding between the alkali-activated paste and aggregates that enhances the mechanical properties of the concrete.

6 COST ANALYSIS

The costs of producing 1m^3 of AAFGC for grades A20, A40, A50, A70 and A80 are shown in Table 8. The activator was found to have the maximum cost, and the fly ash has the minimum cost. For A20, the activator contributes 64.4%, and the fly ash contributes 34.5% out of the total cost of the concrete. For A40, out of the total cost, the contribution of the activator, fly ash and GGBS is 56%, 13.2%, and 30.6%, respectively. Similarly, for the A50, out of the total cost, the contribution of the activator, fly ash and GGBS is 52.2%, 14.3%, and 33.3% respectively. In the same way, for A70 and A80, the activator contributes 45.9% and the GGBS contributes 54% out of the total cost of the concrete. The sodium silicate activator is the highest contributor for the A20, A40 and A50, whereas GGBS is the highest contributor for the A70 and A80 AAFGC grades.

Fig 5. *Split tensile failure of AAFGC*

Fig. 6 *Flexural strength failure of AAFGC*

Tab. 8 *Cost comparison of concrete materials*

Grade	Binder Content	Solution/binder ratio	FA-GGBS	Activator (Rs 16/kg)	Fly ash (Rs 2.3/kg)	GGBS (Rs 3.5/kg)	Total cost (Rs/m^3)
A20	500	0.6	100-0	300	1150	0	7445
A40	300	0.7	50-50	210	345	525	5991
A50	400	0.6	50-50	240	460	700	7348
A70	300	0.65	100-0	195	0	1050	6795
A80	400	0.65	100-0	260	0	1400	9060

7 CONCLUSIONS

1. The neutral grade liquid Na_2SiO_3used as an activating solution in the preparation of the AAGC increased the IST and FST values by avoiding the rapid setting of the concrete. To improve the setting time, no retardants or water reducers were added while mixing the concrete.
2. To develop the workability aspect of the AAFGC, fly ash and slag activated with a neutral grade water glass solution is a possible combination to obtain a better slump.
3. The increase in the slag percentage in the binder reduced the setting time and slump values of the fresh concrete and enhanced the compressive, split tensile and flexural strengths of the hardened concrete at ambient room temperature curing at all the stages.
4. With all the binder contents, increasing the liquid/binder ratio above a certain level does not add to the strength but increases the workability, while the AAFGC mixes with a low liquid/binder ratio are less workable.
5. The AAFC has the maximum slump with the minimum compressive strength, but it is reversed in the AAGC. It is concluded that the AAFGC prepared with neutral grade Na_2SiO_3 can be designed for various slump values and AAFGC grades.
6. The development in the rate of the strength gain in the AAGC at the initial stage was more than in the later stage, whereas, the strength gain rate of the AAFC was very slow in the first 7 days, but it increased rapidly with the stages.
7. The range of the 28 days' compressive strength of the AAFGC for the 300, 400 and 500 kg/m^3 binder contents are 12.9 to 76.5 MPa, 13.8 to 82.5 MPa, and 15.6 to 85.6 MPa respectively.
8. The AAFGC mixes with a greater amount of fly ash can be successfully cured at an ambient temperature. This shows that the fly ash-slag combination provides a solution to the requirement of oven curing for concrete.
9. A high compressive strength of 85.6 MPa was obtained without any oven curing or additional ingredients. These results show that a properly designed AAFGC prepared with a neutral grade sodium silicate single solution can be a promising binder material and activator for the production of highly efficient composites.
10. The AAFGC split tensile and flexural strength increased with the binder content, and the strength variations with an increasing ratio of the liquid/binder was found to be similar to the AAFGC compressive strength.

REFERENCES

Andrew, R. (2018) *Global CO_2 emissions from cement production*. Earth Syst Sci Data, Vol. 10, 195-217.

Arivalagan, S. (2014) *Sustainable studies on concrete with ggbs as a replacement material in cement*. Jordan J. Civil Eng, Vol. 8, No. 3, pp. 263-270.

Bakharev, T. et al. (1999) *Alkali activation of Australian slag cements.* Cement and Concrete Research, Vol. 29, pp. 113–20.

Bernal. S.A. et al. (2010) *Performance of an alkali-activated slag concrete reinforced with steel fibers*. Construct. Build. Mater, Vol. 24, No. 2, pp. 208–214.

Bondar, D. et al. (2011) *Effect of type, form, and dosage of activators on strength of alkali-activated natural pozzolan***.** Cement and Concrete Research, Vol. 33, No. 2, pp. 251-260.

Bondar Qianmin, M.A. (2018) *Alkali Activated slag concretes designed for a desired slump. Strength and chloride diffusivity.* Construction and Building materials, Vol. 190, pp. 191-199.

Caijun, S. - Yinyuz, L. (1989) *Investigation on some factors affecting the characteristics of alkali-phosphorus slag cement*. Cement Concrete Res, Vol. 19, pp. 527–33.

Chindaprasirt, P. et al. (2007) *Workability and strength of coarse high calcium fly ash geopolymer.* Cement and concrete composites, Vol 29, No. 3, pp. 224-229.

Daniel, K. J. et al. (2006) *The behavior of geopolymer paste and concrete at elevated temperatures* In: international Conference on Pozzolan Concrete and Geopolymer, KhonKaen, Thailand, pp. 105–118

Davidovits, J. et al. (1990) *Geopolymeric concretes for environmental protection*. ACI Concr Int J, Vol. 12, No. 7, pp. 30–40.

Davidovits, J. (1994) *Properties of geopolymer cements* In: First international conference on alkaline cements and concretes. Scientific Research Institute on Binders and Materials Kiev, Ukraine, pp. 131–149.

Deb. P.S. et al. (2014) *The effects of ground granulated blast-furnace slag blending with fly ash and activator content on the workability and strength properties of geopolymer concrete cured at ambient temperature.* Materials and Design (1980-2015), Vol. 62, pp. 32-39.

Douglas, E. et al. (1991) *Alkali activated ground granulated blast furnace slag concrete: preliminary investigation*. Cem Concr Res, Vol. 21, No. 1, pp. 101-108.

Douglas, E. et al. (1992) *Properties and durability of alkali activated slag concrete*. ACI Mater J, Vol .89, pp. 509–16.

Elmore, A.R. (2004) *Final Report on the Safety Assessment of Potassium Silicate, Sodium Metasilicate, and Sodium Silicate.* International Journal of Toxicology, Vol. 24, pp. 103-117.

Glukhovsky, V.D. (1980) *High strength slag-alkaline cements*. 7th Inter Congr Chem Cem, Paris, Vol. 3, pp. 164-168.

Glukhovsky, V.D. (1959) *Soil silicates*. Gosstroiizdat, Kiev (in Russian).

Gugulothu, V. - Gunneswara Rao, T.D. (2020) *Effect of Binder Content and Solution/Binder Ratio on Alkali-Activated Slag Concrete Activated with Neutral Grade Water Glass*. Arab J Sci Eng, Vol. 45, pp. 8187–8197.

Hardjito, D. et al. (2004) *On the development of fly ash-based geopolymer concrete*. ACI Mater J, Vol. 101, No. 6, pp. 467–72.

Huanhai, Z. et al. (1993) *Kinetic study of hydration of alkali-activated slag.* Cem Concr Res, Vol. 23, pp. 1253.

Jimenez, A.F. et al. (1999) *Alkali-activated slag mortars: mechanical strength behavior*. Cement Concrete Res, Vol. 29, No. 13, pp. 13–21.

IS 516 – 1959, Indian standard code of practice: Methods of Tests for Strength of Concrete. Bureau of Indian Standards, New Delhi, India.

IS 4031 (part 4) – 1988, Method of physical tests for hydraulic cement: Determination of consistency of standard cement paste. Bureau of Indian Standards, New Delhi, India.

IS 4031 (part 5) – 1988, Method of physical tests for hydraulic cement-Determination of initial and final setting times. Bureau of Indian Standards, New Delhi, India.

IS 1199 -1959, Methods of Sampling and Analysis of Concrete. Bureau of Indian Standards, New Delhi, India.

IS 383-1970, Specification for Coarse and Fine Aggregates from Natural Sources for Concrete. Bureau of Indian Standards, New Delhi, India.

Jannie, H.X. - Deventer, S.J.V. (2002) *Geopolymerisation of multiple minerals*. Miner Eng, Vol. 15, pp. 1131–9.

Joseph. (1999) *Chemistry of geopolymeric systems, terminology*, Geopolymer international conference In: James C (ed.), France, pp. 9–40.

Krizan, D. - Zivanovic, B. (2002) *Effects of dosage and modulus of water glass on early hydration of alkali–slag cements.* Cement and Concrete Research, Vol. 32, No. 118, pp. 1–8.

Landrou, G. et al. (2016) *Lime as an anti-plasticizer for self-compacting clay concrete*. Materials, Vol. 9, pp. 330.

Lee, W.K.M. - Van Deventer, J.S.F. (2007) *Chemical interactions between siliceous aggregates and low-Ca alkali-activated cements*. Cem. Concr. Res, Vol. 37, No. 6, pp. 844–855

Le, Q.C. - Andrew, R.M. (2017) *Global carbon budge.* Earth Syst Sci Data.

Le, Q.C. - Andrew, R.M. (2016) *Global carbon budge.* Earth Syst Sci Data, Vol. 8, pp. 605-649.

Mallikarjuna Rao, G. - Gunneswara Rao, T.D. (2015) *Final setting time and compressive strength of flyash and ggbs based geopolymer paste and mortar*. Arab J Sci Eng, Vol. 40, No. 11, pp. 3067-3074.

Malolepszy, J. - Petri, M. (1986) *High strength slag-alkaline binder*, 8th Inter Congr Chem Cem, Rio de Janeiro, Vol. 4, pp. 108-111.

Midhun, M.S. et al. (2018) *Mechanical and fracture properties of glass fiber reinforced geopolymer concrete*. Adv. Concr. Constr, Vol. 6, No.1, pp. 29–45.

Mustafa, A.M. et al. (2011) *The Effect of Curing Temperature on Physical and Chemical Properties of Geopolymers*. Physics Procedia, Vol. 22, pp. 286–291.

Palacios, M. et al. (2008) *Rheology and setting of alkali-activated slag pastes and mortars: effect of organic admixture*. ACI Materials Journal, Vol. 105, No. (2), pp. 140.

Palacios, M. (2006) Empleo de aditivosorgánicosen la mejora de las propiedades de cementos y morteros de escoria activad al calinamente. Universidad Autónoma de Madrid.

Palacios, M. - Puertas, F. (2011) *Effectiveness of Mixing Time on Hardened Properties of Waterglass-Activated Slag Pastes and Mortars.* ACI Materials Journal. Vol. 108, p. 1.

Patil, A.A. et al. (2014) *Effect of curing condition on strength of geopolymer concrete. Advances in concrete construction.* Vol. 2, No. 1, pp. 029.

Provis, J.L. et al. (2007; 28) *Will geopolymers stand the test of time?* Ceram. Eng. Sci. Proc, Vol. (9), pp. 235–248.

Provis, J.L. (2014) Introduction and scope. In: Provis J.L., Van Deventer J S J (ed.). *Alkali Activated Materials*. State-of-the-Art Report. RILEM TC 224-AAM. Springer, Dordrecht, pp. 1–9.

Puertas, F. et al. (2014) *Rheology of alkali-activated slag pastes. Effect of the nature and concentration of the activating solution.* Cement and Concrete Composites, Vol. 53, pp. 279-288.

Richardson, I.G. et al. (1994) *The characterization of hardened alkali-activated blast-furnace slag pastes and the nature of the calcium silicate hydrate (C–S–H) phase.* Cement Concrete Res, Vol. 25, pp. 813–29.

Rodriguez-Puerta, C. (2014) Comportamiento reologico y mecanico de pastas y morteros de cementos eco-eficiente Reutilizacion de residuos vitreos, Proyecto, Fin de Carrera-UPM-CSIC.

Shi, C. - Day, R.L. (1995) *A calorimetric study of early hydration of alkali-slag cements,* Cement and Concrete Research, Vol. 25, No. 6, pp. 1333-1346.

Shi, C. et al. (2006) *Alkali-activated cement and concretes*. London and NY, Taylor and Francis.

Shi, C. et al. (2005) Characteristics and pozzolanic reactivity of glass powders. Cem Concr Res, Vol. 35, pp. 987– 99.

Tailing, B. - Brandstetr, J. (1989) *Present state and future of alkali-activated slag concretes:* 3rd Inter Conf Fly Ash. Silica Fume. Slag and Natural Pozzolans in Concrete, Trondheim, 2 SP 114-74:1519-1546.

Temuujin, J. et al. (2009) *Influence of calcium compounds on the mechanical properties of fly ash geopolymer paste*. J Hazard Mater, Vol. 167, pp. 82–88.

Thunuguntla, C.S. - Rao, T.G. (2018) *Effect of mix design parameters on mechanical and durability properties of alkali activated slag concrete*. Construction and Building Materials, Vol.193, pp.173-188.

Venu, M. - Rao T.G. (2017) *Tie-confinement aspects of fly ash-GGBS based geopolymer concrete short columns.* Constr. Build. Mater, Vol. 151, pp. 28–35.

Vikas, G. - Rao, T.D.G. (2021) *Setting Time, Workability and Strength Properties of Alkali Activated Fly Ash and Slag Based Geopolymer Concrete Activated with High Silica Modulus Water Glass.* Iran J Sci Technol Trans Civ Eng, Vol. 45, pp. 1483–1492.

Wang, S.D. et al. (1995) *Alkali-activated slag cement and concrete: a review of properties and problem.* Adv Cem Res, Vol. 27, pp. 93-102.

Wang, S.D. et al. (1994) *Factors affecting the strength of alkali-activated slag*. Cement Concrete Res, Vol. 24, pp. 1033–43.

Wang, S.D. - Scrivener, K.L. (1994) *Comment on activation of ground blast furnace slag by alkali-metal and alkaline-earth hydroxides*. Am Ceram Soc, Vol. 77, No. 4, pp. 11-16.

Wongpa, J. et al. (2010) *Compressive strength, modulus of elasticity, and water permeability of inorganic polymer concrete*. Mater. Des, Vol. 31, No. 10, pp. 4748–4754.

Wan, H. et al. (2004) *Analysis of geometric characteristics of GGBS particles and their influences on cement properties*. Cem Concr Res, Vol. 34, pp. 133–137.

Wardhono, A. et al.(2014) *The mechanical properties of fly ash geopolymer in long term performance*, In: The CIC2014 “Concrete Innovation Conference”, Oslo, Norway.

Xi, F. - Davis, S.J. (2016) *Substantial global carbon uptake by cement carbonation.* Nat Geo Sci, Vol. 9, pp. 880- 883.

Xu, H. - Van Deventer, J.S.J. (2000) *The geo-polymerization of alumino-silicate minerals.* Int J Miner Process, Vol. 59, pp. 247–66.

Zivica, V. (2007) *Effects of type and dosage of alkaline activator and temperature on the properties of alkali-activated slag mixtures*. Construction and Building Materials, Vol. 21, pp. 1463-1469.